

University of Windsor

Scholarship at UWindor

Electronic Theses and Dissertations

Theses, Dissertations, and Major Papers

1997

Effect of Be on the nucleation and growth of beta' phase in aluminum-magnesium-silicon alloy.

Ali. Hatab
University of Windsor

Follow this and additional works at: <https://scholar.uwindsor.ca/etd>

Recommended Citation

Hatab, Ali., "Effect of Be on the nucleation and growth of beta' phase in aluminum-magnesium-silicon alloy." (1997). *Electronic Theses and Dissertations*. 1816.
<https://scholar.uwindsor.ca/etd/1816>

This online database contains the full-text of PhD dissertations and Masters' theses of University of Windsor students from 1954 forward. These documents are made available for personal study and research purposes only, in accordance with the Canadian Copyright Act and the Creative Commons license—CC BY-NC-ND (Attribution, Non-Commercial, No Derivative Works). Under this license, works must always be attributed to the copyright holder (original author), cannot be used for any commercial purposes, and may not be altered. Any other use would require the permission of the copyright holder. Students may inquire about withdrawing their dissertation and/or thesis from this database. For additional inquiries, please contact the repository administrator via email (scholarship@uwindsor.ca) or by telephone at 519-253-3000ext. 3208.

INFORMATION TO USERS

This manuscript has been reproduced from the microfilm master. UMI films the text directly from the original or copy submitted. Thus, some thesis and dissertation copies are in typewriter face, while others may be from any type of computer printer.

The quality of this reproduction is dependent upon the quality of the copy submitted. Broken or indistinct print, colored or poor quality illustrations and photographs, print bleedthrough, substandard margins, and improper alignment can adversely affect reproduction.

In the unlikely event that the author did not send UMI a complete manuscript and there are missing pages, these will be noted. Also, if unauthorized copyright material had to be removed, a note will indicate the deletion.

Oversize materials (e.g., maps, drawings, charts) are reproduced by sectioning the original, beginning at the upper left-hand corner and continuing from left to right in equal sections with small overlaps. Each original is also photographed in one exposure and is included in reduced form at the back of the book.

Photographs included in the original manuscript have been reproduced xerographically in this copy. Higher quality 6" x 9" black and white photographic prints are available for any photographs or illustrations appearing in this copy for an additional charge. Contact UMI directly to order.

UMI

**A Bell & Howell Information Company
300 North Zeeb Road, Ann Arbor MI 48106-1346 USA
313/761-4700 800/521-0600**

**EFFECT OF Be ON THE NUCLEATION
AND GROWTH OF β' PHASE IN
Al-Mg-Si ALLOY**

by

Ali Hatab

**A Dissertation
Submitted to the
Faculty of Graduate Studies and Research
Through the Department of Mechanical and
Materials Engineering
in Partial Fulfilment of the Requirements
for the Degree of Doctor of Philosophy
at the University of Windsor**

**Windsor, Ontario, Canada
1997**



**National Library
of Canada**

**Acquisitions and
Bibliographic Services**

**395 Wellington Street
Ottawa ON K1A 0N4
Canada**

**Bibliothèque nationale
du Canada**

**Acquisitions et
services bibliographiques**

**395, rue Wellington
Ottawa ON K1A 0N4
Canada**

Your file Votre référence

Our file Notre référence

The author has granted a non-exclusive licence allowing the National Library of Canada to reproduce, loan, distribute or sell copies of this thesis in microform, paper or electronic formats.

L'auteur a accordé une licence non exclusive permettant à la Bibliothèque nationale du Canada de reproduire, prêter, distribuer ou vendre des copies de cette thèse sous la forme de microfiche/film, de reproduction sur papier ou sur format électronique.

The author retains ownership of the copyright in this thesis. Neither the thesis nor substantial extracts from it may be printed or otherwise reproduced without the author's permission.

L'auteur conserve la propriété du droit d'auteur qui protège cette thèse. Ni la thèse ni des extraits substantiels de celle-ci ne doivent être imprimés ou autrement reproduits sans son autorisation.

0-612-30273-3

© **Ali Hatab 1997**

**In the name of Allah, Most Gracious, Most Merciful.
“Of knowledge it is only a little that is communicated to you, (O men!).”
And say: “O my Lord! Increase me in knowledge.”**

**To My Father who is in complete rest,
Allah may forgive him, mercy him, and
enter him to his heaven.**

And

To My Blessed Children

Mehdi

Ziad

Ahmed

Isra

ABSTRACT

An investigation on the effect of Be on β' phase precipitation in Al-0.7%Mg-0.4%Si alloy was carried out using microhardness and resistivity measurements, and optical and TEM observations. It is shown that addition of 0.4%Be to an Al-0.7%Mg-0.4%Si (base) alloy significantly enhances the age hardening response and increases the peak hardness levels of the alloy, which is associated with a refinement of the β' (Mg₂Si) precipitate. Hardness and resistivity techniques used to study the precipitation kinetics show that the two methods are in good agreement for monitoring the transformation rates. A kinetic analysis shows that precipitation of β' phase in both the base and the Be-containing alloy obeys the modified Avrami-Johnson-Mehl equation, and that the Be addition does not alter the growth parameter (n) or the activation energy (Q_1), but increases 2-3 fold the nuclei density-dependent parameter (k_1), which agrees well with the optical and TEM observations. The activation energy (Q_1) obtained is in the accepted range for vacancy diffusion in Al alloys, indicating it is the transport mechanism controlling the rate of growth of the β' phase.

Optical results show that the Be addition reduces the as-cast grain size, significantly inhibits grain growth during the aging, and increases the density of dislocation etch pits. The TEM results show that the increase in precipitate particle density in the aged Be-containing alloy, compared with the lower dislocation loops and higher density of dislocation lines (corresponding to a higher concentration of Be-trapped vacancies) for the quenched alloy, indicates that as aging proceeds at higher temperatures, the trapped vacancies are released and condense to form dislocation loops that act as sites for β' nucleation.

A theoretical calculation of the activation energy (ΔG^*) for β' nucleation, which includes the effects of phase transformation, strain, and interfacial energies, shows a ~13% decrease for the Be-containing alloy, giving a ~1.7-fold increase in the classical nucleation rate for β' .

ACKNOWLEDGEMENTS

The author would like to take this opportunity to express his sincere gratitude to his advisor Dr. W.V.Youdelis for his advice, guidance, supervision, and encouragement throughout this investigation . He is also grateful to Dr. W.Yang and Mr. John Robinson for their assistance in the TEM work.

He is very grateful to his family and especially his mother, bother, and sisters for their support and encouragement throughout his years of education.

Finally, he wishes to express his deepest gratitude to his wife for her support and patience throughout this investigation .

TABLE OF CONTENTS

ABSTRACT.....	v
ACKNOWLEDGEMENTS.....	vii
LIST OF TABLES	xi
LIST OF FIGURES.....	xii
Chapter	
1 INTRODUCTION.....	1
2 LITERATURE REVIEW.....	4
2.1 Basic Concepts of Precipitation Hardening.....	4
2.2 Nucleation of Precipitates.....	5
2.2.1 Strain Energy-Free Nucleation	6
2.2.2 Nucleation Involving Strain Energy	8
2.2.3 Heterogeneous Nucleation.....	12
2.2.3.1 Nucleation on Dislocations.....	12
2.2.3.2 Nucleation on Grain Boundaries.....	14
2.2.4 Refinement of Precipitates.....	15
2.2.5 Nucleation Entropy Concept.....	16
2.3 Kinetics of Precipitation Processes.....	20
2.3.1 Modified Avrami Equation.....	21
2.4 Aluminum Alloy Systems.....	23
2.4.1 Aluminum-Magnesium.....	23
2.4.2 Aluminum-Silicon.....	25
2.4.3 Aluminum-Magnesium Silicide.....	25
2.4.4 Aluminum-Beryllium.....	30
2.4.5 Aluminum-Silicon-Beryllium.....	30
2.4.6 Aluminum-Magnesium-Beryllium.....	30
2.5 Precipitation Stages in Al-Mg-Si Alloys.....	34
2.6 Structural Aspects of the Precipitating Phases.....	35
2.6.1 GP Zones.....	35
2.6.2 β'' and β' Transition Phases.....	35
2.6.3 β Equilibrium Phase.....	36

2.6.4	Trace Element Effects.....	36
2.7	Be Effects on Precipitation in Al-Mg-Si Alloys.....	38
3	EXPERIMENTAL.....	40
3.1	Alloy Preparation.....	40
3.2	Analytical Procedures.....	40
3.2.1	Optical Microscopy.....	40
3.2.2	Transmission Electron Microscopy.....	41
3.2.3	Microhardness Measurement.....	42
3.2.4	Resistivity Measurement.....	42
4	RESULTS AND DISCUSSION.....	45
4.1	Optical Microscopy.....	45
4.1.1	As-Cast Microstructures.....	45
4.1.2	As-Quenched Microstructures.....	45
4.1.3	Etch Pits at Dislocations.....	50
4.2	Aging Behaviour.....	53
4.2.1	Precipitation Stages.....	53
4.2.2	Kinetic Treatment of Rate Data.....	57
4.2.3	Aged Microstructures.....	79
4.3	TEM Microscopical Observations.....	83
4.3.1	As-quenched and Room Temperature Aged Alloys.....	83
4.3.1.1	Dislocation Loop Formation.....	83
4.3.2	Peak Hardness Structure.....	88
4.3.3	Overaged Structure.....	90
5	Be EFFECT ON NUCLEATION RATE OF β' PHASE.....	94
5.1	Nucleation Thermodynamics and Kinetics.....	94
5.2	Nucleation Entropy of Mg_2Si	94
5.3	Nucleation Entropy of $Mg_2SiBe_{0.15}$	98
5.4	Determination of Strain Energy.....	100
5.5	Nucleation Rate Comparison.....	101
6	CONCLUSIONS AND RECOMMENDATIONS.....	105
6.1	Conclusions.....	105
6.2	Recommendations.....	106
	REFERENCES.....	108
	APPENDICES	
A	Nucleation Entropy Calculation	115

PUBLICATIONS.....	117
VITA AUCTORIS.....	118

LIST OF TABLES

Table 1	Invariant reactions at the Al end of the Al-Mg-Si diagram.....	29
Table 2	Kinetic parameters.....	77
Table 3	Reaction sequence for calculating ΔS for precipitation of Mg_2Si at 250°C.....	97
Table 4	Reaction sequence for calculating ΔS for precipitation of $Mg_2SiBe_{0.15}$ at 250°C.....	99
Table 5	Comparison of nucleation rates for Mg_2Si and $Mg_2SiBe_{0.15}$ at 250°C.....	103

LIST OF FIGURES

Figure 1	Aluminum-Magnesium phase diagram.....	24
Figure 2	Aluminum-Silicon phase diagram.....	26
Figure 3	Aluminum-Magnesium Silicide quasibinary phase diagram.....	27
Figure 4	Partial Aluminum-Magnesium-Silicon ternary phase diagram.....	28
Figure 5	Aluminum-Beryllium phase diagram.....	31
Figure 6	Aluminum-Silicon-Beryllium phase diagram.....	32
Figure 7	Partial Aluminum-Magnesium-Beryllium phase diagram.....	33
Figure 8	Resistivity specimen 0.2mm thick.....	44
Figure 9	Optical Macrographs of the as-cast alloys.....	46
Figure 10	Optical Micrographs of the as-cast alloys.....	47
Figure 11	Optical Macrographs of the as-quenched alloys.....	48
Figure 12	Optical Micrographs of the as-quenched alloys.....	49
Figure 13	Optical Micrographs of the as-quenched alloys, showing dislocations etch pits and a tilt boundary at A and dislocation clusters at B.....	51
Figure 14	Optical Micrographs for alloys Aged at room Temperature for 12 months, showing dislocations etch pits.....	52
Figure 15	Optical Micrographs for alloys Aged at 250°C for 20 min, showing dislocations etch pits.....	54
Figure 16	Optical Micrographs for alloys Aged at 250°C for 65 min, showing dislocations etch pits.....	55

Figure 17	(a) HV vs. log t, (b) ρ vs. log t and (c) $\Delta\rho$ vs. log t for alloys aged at room temperature.....	58
Figure 18	(a) HV vs. log t, (b) ρ vs. log t and (c) $\Delta\rho$ vs. log t for alloys aged at 150°C.....	60
Figure 19	(a) HV vs. log t and (b) ρ vs. log t for alloys aged at 200°C.....	62
Figure 20	(a) HV vs. log t and (b) ρ vs. log t for alloys aged at 250°C.....	63
Figure 21	(a) HV vs. log t and (b) ρ vs. log t for alloys aged at 300°C.....	64
Figure 22	dp/dt vs. t for alloys aged at 200°C.....	66
Figure 23	dp/dt vs. t for alloys aged at 250°C.....	67
Figure 24	dp/dt vs. t for alloys aged at 300°C.....	68
Figure 25	Y vs. log t for alloys aged at 200°C.....	70
Figure 26	Y vs. log t for alloys aged at 250°C.....	71
Figure 27	Y vs. log t for alloys aged at 300°C.....	72
Figure 28	$\log \ln (1/(1-Y))$ vs. log t for alloys aged at 200°C.....	73
Figure 29	$\log \ln (1/(1-Y))$ vs. log t for alloys aged at 250°C.....	74
Figure 30	$\log \ln (1/(1-Y))$ vs. log t for alloys aged at 300°C.....	75
Figure 31	Arrhenius plots using k_1	76
Figure 32	Optical Micrographs for alloys aged at 250°C for 140 hrs.....	80
Figure 33	Optical Micrographs for alloys aged at 250°C for 140 hrs.....	81
Figure 34	Optical Micrographs for alloys aged at 300°C for 17 hrs.....	82

Figure 35	TEM Micrographs of the as-quenched alloys, showing dislocation lines chopped off at A and dislocation loops at B.....	85
Figure 36	TEM Micrographs and corresponding SADP of the as-quenched alloys, showing large dislocation loops at A and small loops at B.....	86
Figure 37	TEM Micrographs and corresponding SADP for alloys aged at room temperature for 4 months, showing dislocations pinned by precipitates.....	87
Figure 38	TEM Micrographs and corresponding SADP for alloys aged at 250°C for 65min, showing β'' needles and β' rods.....	89
Figure 39	TEM Micrographs and corresponding SADP for alloys aged at 250°C for 600min, showing β' rods.....	91
Figure 40	TEM Micrographs and corresponding SADP for alloys aged at 250°C for 600min, showing β' rods and β plates.....	92

CHAPTER 1

INTRODUCTION

The increased demand for higher fuel efficiency has led to the development of light weight vehicles, in which light metal alloys (Al, Mg) are replacing much of the steel and cast iron used in the earlier models. Aluminum alloys offer substantial weight savings due to their low density and competitive strength. The combination of relatively good ductility, formability and weldability, without a serious decrease in the strength and fatigue resistance, and coupled with the high corrosion resistance and attractive surface appearance, renders Al-Mg-Si alloys (6xxx series) very attractive for use in the auto industry. Al-Mg-Si alloys also find use in many other areas, including the aerospace industry, structural engineering (bridges, buildings), rolling stock, hydraulic tubing, etc.

Precipitation processes are the basis for the development and control of strength and hardness of age hardenable alloys by heat treatment. The influence of the precipitates on the mechanical properties of the alloys depends on the degree of coherency, the relative orientation relationship of the precipitate to the matrix, and the precipitate morphology (size and spacing).

Age hardening in Al-Mg-Si alloys is due to GP zone formation and subsequent β' (metastable Mg_2Si) precipitation[74,80]. Although the GP zones are coherent with the matrix, coherency strains are low. The hardening effect is due primarily to the structural complexity of the precipitate (Mg_2Si) phase, which increases the resistance to dislocation motion, thereby increasing the alloy's shear strength. The desired microstructure of Al precipitation hardening

alloys (for strength and fatigue resistance) can to a large degree be obtained through appropriate solution treatment and aging procedures. Thermal mechanical treatments (cold working plus heat treatment) are additional means for improving the mechanical properties for the alloys.

The addition of specific microalloying elements to some Al-base alloys strongly affects the alloys' aging response, which is attributed to increasing defect concentrations (vacancies and dislocations), and/or refining the precipitate by increasing its nucleation rate. Incorporation of trace elements into the precipitate phase may significantly change the energetics of the nucleation process through changes in the precipitate's volume free energy of formation, strain, and interfacial energies. The former, which can be related to the mixing or configurational entropy change for the system, is of particular interest, since the nucleation rate is greatly affected by small entropy changes accompanying the transformation. Earlier studies by Youdelis and coworkers[1-4] have shown that small additions of third elements(e.g., Si, Be) significantly enhances the grain refinement of Al by Ti. It was shown that Si and Be are incorporated into the TiAl_3 compound, with the net result of increasing the nucleation rate of TiAl_3 , and ultimately enhancing grain refinement. It was also shown that small additions of Be are extremely effective in stimulating the nucleation and refinement of metastable phases in Al-Cu[5,6], Al-Cu-Mg[7,8] and Al-Li-Cu-Mg[9,10] alloys, with attendant increases in the peak hardness for the aged alloys.

The effects of Be on the age hardening behaviour of the natural aging Al-0.75%Mg-0.5%Si* alloy have been previously reported[11,12]. It was shown that the additions of

*** All concentrations in wt% or as otherwise indicated.**

0.1%Be significantly increases the hardening rate and peak hardness value for the aged alloys, and is associated with a significant increase in the density (refinement) of precipitate particles. A kinetic analysis showed that the precipitation kinetics for the β (Mg₂Si) phase obeys the Avrami-Johnson-Mehl equation[12], and that the hardening rate increase is the result of a Be-enhanced nucleation rate. The latter is attributed to Be incorporation into the β phase, which is shown[13] to be plausible based on unit cell and atom size considerations.

The present investigation is undertaken to determine the specific role of Be addition on the precipitation stages in the Al-0.7%Mg-0.4%Si alloy during aging. The precipitation stages and kinetic information are determined using microhardness and resistivity techniques. Microstructures of as-cast, as-quenched, and aged alloys are obtained using optical microscopy. Defect and precipitate morphology, density, distribution, and size during aging are determined using transmission electron microscopy. The TEM results obtained are discussed in relation to the effect of Be on the aging kinetics for the alloy, i.e., the nucleation, growth, and coarsening processes for the β' phase.

CHAPTER 2

LITERATURE REVIEW

2.1 Basic Concepts of Precipitation Hardening

Many heat treatable alloys exhibit age hardening at room temperature (natural aging) after a solution treatment, and this property is exploited to develop the mechanical properties of the alloy. The increase in strength in age-hardenable alloys derives from the coherent (or partially coherent) dispersed particles of intermetallic phases formed by precipitation from supersaturated solid solution. The heat treatment of an age-hardening alloy generally consists of: (i) solution treatment (solutionizing) to produce a homogeneous solid solution, (ii) quenching to room temperature or lower to retain a supersaturated solid solution, and (iii) reheating to an intermediate temperature and holding for determined time to precipitate the second phase within the matrix. The basic requirements for an alloy to exhibit precipitation hardening are: (i) a limiting solid solubility that rapidly decreases with temperature, allowing substantial supersaturation when quenching the alloy from a homogenized single-phase region, and (ii) precipitation of an (initially) coherent or partially coherent precipitate.

The formation of a precipitate in a supersaturated solid solution derives from a net reduction in free energy, and thus the essential driving force for a precipitation process is the difference in the free energies of the initial and final compositions and configurations of the alloy phases. The basic stages involved in a precipitation process are: (i) the formation of stable nuclei of the new phase (nucleation stage), (ii) the growth of the new phase nuclei

forming the precipitate particles (growth stage), and (iii) the coarsening of the precipitate particles (Ostwald Ripening stage). Generally, the equilibrium phase does not precipitate directly, i.e., the precipitation process may involve the formation of one or more metastable transition phases, for example: Guinier-Preston (GP) zones, θ'' , and θ' as precursors of stable θ phase (Al_2Cu) in the Al-Cu system; and GP zones and β' as precursors of stable β phase (Mg_2Si) in the Al-Mg-Si system. Metastable phases are partially or fully coherent with the matrix, and form when the atomic misfit between the precipitate and matrix does not exceed a maximum sustainable amount. Also, there is a particular orientation relationship between the precipitating and parent phases that minimizes the interfacial energy. The precipitation sequence, and the corresponding mechanism for each stage of the transformation depend on the particular alloy system and on aging temperature. The alloy's strength and other mechanical properties depends on the nature of the precipitates, i.e., their coherency degree, morphology, density, distribution, size and orientation relationships with the matrix.

2.2 Nucleation of Precipitates

Nucleation produces the first aggregates of the new phase that grow spontaneously to relieve the supersaturation of the parent matrix. The nucleation barrier controlling the formation of a second phase depends on the resulting interfacial and strain energies for the critical nucleus. The nucleus shape is essentially a compromise between these factors. The preferred nuclei have a crystallographic relationship with respect to the parent phase that minimizes the interfacial energy (other factors such as strain energy assumed constant). Nucleation can occur uniformly throughout the supersaturated matrix (homogeneous

nucleation) or preferentially at specific sites (heterogeneous nucleation), such as preexisting phases or impurity particles, grain boundaries, or dislocations which can lower the interfacial and strain energy barrier.

The classical theory for nucleation from a vapour phase was first developed by Volmer and Weber[14], and Becker and Doring[15], which was then extended by Turnbull and Fisher[16] to describe nucleation for solid state phase transformations. The investigation of Servi and Turnbull[17] on precipitation in Cu-Co alloys provided the first test of homogeneous nucleation theory in metallic solids. The subject of solid state nucleation has been comprehensively reviewed by several authors, including, Kelly and Nicholson[18], Christian[19], Nicholson[20], Russell[21], Aaronson et al.[22] and Russell[23].

2.2.1 Strain Energy-Free Nucleation

For a stable nucleus to form the interfacial energy barrier must be overcome by the decrease in the volume free energy of transformation. In the absence of strain energy, the free energy change (ΔG) for the formation of a spherical embryo of a radius r is given by[16]

$$\Delta G = (4/3\pi r^3 \Delta G_v) + (4\pi r^2 \gamma) \quad (1)$$

where ΔG_v and γ are the volume free energy change and the specific interfacial energy respectively. Minimizing eq.(1) with respect to the radius gives for the free energy of formation of a critical-sized embryo

$$\Delta G^* = (16\pi\gamma^3)/(3\Delta G_V^2) \quad (2)$$

The resulting homogeneous nucleation rate (\dot{N}) is directly proportional to the concentration of critical-sized embryos and diffusion rate across the embryo's boundary, and is given by

$$\dot{N}_{\text{homo}} = (K)\exp[(-16\pi\gamma^3)/(3\Delta G_V^2 kT)] \quad (3)$$

where the parameter K includes the embryo surface concentration of atoms, and the jump frequency for an atom across the interface, which is exponentially dependent on the activation energy for the jump process (magnitude comparable to the activation energy for grain boundary diffusion).

For low undercooling the volume free energy of transformation ΔG_V is related to the volume entropy change ΔS_V and the undercooling ΔT by [24]

$$\Delta G_V \cong -\Delta S_V \Delta T \quad (4)$$

so that the nucleation rate becomes

$$\dot{N}_{\text{homo}} = (K)\exp[(-16\pi\gamma^3)/(3\Delta S_V^2 \Delta T^2 kT)] \quad (5)$$

Eq.(5) shows that the nucleation rate is exponentially dependent on the square of both the undercooling and volume entropy change for the transformation (here referred to as

nucleation entropy), so that a small increases in entropy or undercooling can result in very large increases in the nucleation rate.

2.2.2 Nucleation Involving Strain Energy

The above treatment of nucleation is applicable only to phase transformations for which the strain energy due to the volume change is negligible, e.g., for liquid-solid transformations (solidification). However, in solid state transformations, strain energy usually results from the associated volume changes, and must be included in the activation energy for nuclei formation, i.e.,

$$\Delta G = V(\Delta G_v + W) + A\gamma \quad (6)$$

where V is the volume of a new phase, A the interface area and W the strain energy per unit volume of precipitate.

The strain energy arises from two sources[25]: (i) the interfacial strain caused by whatever misfit exists between the two (coherent) phases before the precipitate has grown to a sufficient size to induce a dislocation to take up the distortion (e.g., GP zones), and (ii) the strain due to the different specific volumes of the matrix and precipitate. This problem has been considered by Nabarro[26], who assumed that the nucleus and matrix are both strained isotropically, and used a continuum mechanics approach to determine the value of W , which is independent of the shape of the particle, to give

$$W = 6\mu_p \delta^2 / (1 + (4\mu_p / 3K_m)) \quad (7)$$

where μ_p is the shear modulus of the precipitate phase, K_m the bulk modulus of the matrix, and δ the lattice misfit between a precipitate nucleus and the matrix due to the difference in lattice parameters. If the value of Poisson's ratio (ν) is taken as 0.33 then $K=2\mu$, and if the moduli of the matrix and precipitate are similar ($\mu_p = \mu_m$), then

$$W \approx 2((1+\nu)/(1-\nu)) \mu \delta^2 \approx 4\mu \delta^2 \quad (8)$$

For hard particles in a softer matrix, it is more realistic to assume that the nuclei are unstrained, and that only the matrix suffers hydrostatic volume strain. In this case Nabarro found that W becomes a function of the shape of the particle (ellipsoid) and

$$W = (2/3)\mu_m (\Delta V/V)^2 f(c/r) \quad (9)$$

where μ_m is the shear modulus of the matrix, $\Delta V/V = (V_p - V_m)/V_p$ is the fractional volume change in the matrix accompanying the transformation, and $f(c/r)$ is a function of the ratio of minor (c) to major (r) axes of the ellipsoid, and so depends on particle shape: it is unity for a sphere ($c/r=1$), 0.75 for a rod ($c/r \gg 1$), and $3\pi c/4r$ for a thin plate ($c/r \ll 1$). Thus the strain energy is minimum when the precipitate is plate-like in shape and approaches zero as c/r decreases to zero.

Local strains around a precipitate will produce large energy increases if the strain is

taken up elastically, since elastic moduli of metals are large. Doherty[24] shows that for Al (Young's modulus $\sim 70\text{GPa}$), a 1% shear strain results in an elastic energy of 3.5MJ/m^3 ($\sim 35\text{J/g-atom}$), and a 5% deformation gives an energy 25 times larger. This energy can be reduced plastically by the introduction of dislocations into the interface, at the expense, however, of raising the interfacial free energy. A dilational type of elastic strain can be relaxed plastically by dislocation motion, or by diffusional motion of point defects. Strain energy release mechanisms operate easily at higher temperatures, especially where motion of point defects are involved.

Lee et al.[27,28] have reviewed the results of current theoretical and experimental studies on the influence of elastic and plastic strains on precipitation in general, and nucleation in particular. For the elastic situation, the detailed theoretical analysis shows that the elastic strain energy is minimized when the precipitate is formed as a thin disc-like or plate-like shape, as originally shown by Nabarro[26].

The type of strain energy is closely related to the morphology of the precipitate, and models to analyze strain energy effects have been developed separately on this basis. The models are generally divided into two groups according to the type of precipitate/matrix interface, coherent or incoherent.

For a coherent interface, the crystallographic planes of matrix and precipitate, i.e., the atomic configurations and spacings, are identical or very nearly identical. A theoretical analysis of the elastic strain energy associated with an ellipsoidal coherent precipitate in an isotropic matrix was first presented by Eshelby[29,30]. Lee et al.[31,32] extended Eshelby's treatment to the general anisotropic case, and showed that the free energy is minimized when

the particle is an oblate ellipsoid, for which

$$\Delta G = \left\{ \left(\frac{4}{3} \pi r^3 \beta [\Delta G_v + W] + (\pi r^2 \gamma) [2 + g(\beta)] \right) \right\} \quad (10)$$

where $\beta = c/r$ is the ratio of the ellipsoid's semi-major axes. The function $g(\beta)$ is given by

$$g(\beta) = \begin{cases} \frac{2\beta^2}{(1-\beta^2)^{1/2}} \tanh^{-1}(1-\beta^2)^{1/2} & \text{when } \beta < 1 \\ 2 & \text{When } \beta = 1 \\ \frac{2\beta}{(1-\beta^{-2})^{1/2}} \sin^{-1}(1-\beta^{-2})^{1/2} & \text{when } \beta > 1 \end{cases} \quad (11)$$

To find the ΔG^* , ΔG is minimized with the respect to both r (for r^*) and β (for β^*) to give

$$\Delta G^* = \left\{ (\pi \gamma^3) [2 + g(\beta^*)]^3 / (12) [\beta^*]^2 [\Delta G_v + W]^2 \right\} \quad (12)$$

The strain varies with the aspect ratio, and for the anisotropic case varies markedly with the orientation relationship between matrix and precipitate. An analysis of ΔG^* shows that the minimum value of ΔG^* is obtained at $\beta = 1$, i.e., the spherical nucleus, until $(W/|\Delta G_v|) > 0.82$. The critical free energy of formation of a spherical embryo is obtained by substituting $\beta = 1$ and $g(\beta) = 2$ into Eq.(10), to give

$$\Delta G^* = \left\{ (16\pi \gamma^3) / (3) [\Delta G_v + W]^2 \right\} \quad (13)$$

An incoherent interface is one across which there is no crystallographic continuity. In such a case, the strain associated with the formation of an embryo in a crystalline lattice is hydrostatic[33]. For an oblate spheroid [$c/r \ll 1$, $V = 4/3\pi r^2 c$, $A = 2\pi r^2$, $f(c/r) = 3\pi c/4r$], the free energy of formation of a critical-sized embryo (nucleus) becomes[34]

$$\Delta G^* = (8\pi^3 \mu_\alpha^2 \gamma^3 (\Delta V/V)^4 / 3(\Delta G_v)^4) \quad (14)$$

2.2.3 Heterogeneous Nucleation

It is well known that defects, such as grain boundaries, dislocations, stacking faults, etc., are effective catalysts for nucleation of precipitates under certain circumstances[35-38]. The energy of formation of the nucleus in the heterogeneous nucleation situation is reduced due to a reduction in interfacial and/or strain energies. For nucleation on grain boundaries, part of the boundary area is eliminated for a net reduction of interfacial energy. When there is an appreciable volume strain energy associated with nucleation, transition phases will nucleate preferentially at dislocations if there is a net reduction in the volume strain energy [39,40]. Nucleation at dislocations can be incoherent[38,41] or coherent[42-44], and in both cases, the associated volume strain energy may be reduced. Actually, most intermediate precipitates appear to nucleate either on dislocations or on preexisting GP zones[45,46].

2.2.3.1 Nucleation on Dislocations

Nucleation involving dislocations may occur in four relatively different ways:

- (a) Formation of an incoherent particle on the dislocation line, so as to release the strain

energy of the latter and to make additional contributions to the free energy available to aid the nucleation process.

(b) Formation of a coherent particle near a dislocation, where the transformation strain is already provided, to minimize the volume strain energy of the nucleus.

(c) Formation of a semi-coherent particle in contact with the dislocation, with the direction of a worst misfit aligned parallel to the Burgers vector. This arrangement allows a maximum release of strain energy and uses part of the dislocation core energy for creating the incoherent interface.

(d) Nucleation on the stacking fault between two partial dislocations. In addition to being a high energy region, the stacking fault represents a thin layer of material of a different crystal structure.

In general, dislocations can modify several aspects of the precipitation process in crystalline solids. They provide a stress field that may interact with the misfit strain created by the formation of a nucleus, reducing the activation energy necessary for its appearance. This stress field can also accelerate the diffusion process, changing the kinetics of precipitation. The idea that dislocations can act as catalysts for nucleation of a new phase in solids was first proposed by Cottrell[47] and Koehler et al[48]. They suggested independently that accommodation of the misfit strain by the strain field of the dislocation would lower the activation energy necessary for the formation of a nucleus.

Larche [43] has reviewed the results of current theoretical studies on the problem of the formation of coherent embryos on or near an edge dislocation. The total change in free energy of a spherical embryo is given by

$$\Delta G = (-4A\pi r^2/3) + (4\pi\gamma r^2) + (4\pi Br^3/3) \quad (15)$$

for which the critical radius is obtained from

$$d(\Delta G)/dr = 0 = (-8A\pi r/3) + (8\pi\gamma r) + (4\pi Br^2) \quad (16)$$

$$\text{to give} \quad r^* = ((2A - 6\gamma)/3B) \quad (17)$$

$$\Delta G^* = (2A - 6\gamma/3B)^2 (-4\pi A + 12\pi\gamma/9) \quad (18)$$

$$-B = \Delta G_v + (2\mu_\alpha/9)(1+\nu/1-\nu)(e^T)^2 \quad (19)$$

$$\text{and} \quad -A = (\mu_\alpha b/3\pi)(1+\nu/1-\nu)(e^T) - (b(1+2\nu)(1-2\nu) \Delta G_v / 4\pi(1+\nu)(1-\nu)) \quad (20)$$

In the above, b is Burgers vector, e^T the stress-free transformation strain, μ_α the shear modulus, γ the interfacial energy and ν Poisson's ratio.

2.2.3.2 Nucleation on Grain Boundaries

Formation of embryos on grain boundaries results in the elimination of part of the grain boundary, the released energy aiding the nucleation process. The most probable shape of the embryo is a symmetrical double spherical lens, for which the volume is $(2\pi/3)(2-3\cos\theta+\cos^3\theta)(r^3)$, the surface area $(4\pi)(1-\cos\theta)(r^2)$, and the area of the destroyed grain boundary $(\pi\sin^2\theta)(r^2)$. This gives for the free energy of formation of the embryo at a grain boundary [49]

$$\Delta G_b = (2\pi/3)(2-3\cos\theta+\cos^3\theta)(r^3)\Delta G_v + (4\pi)(1-\cos\theta)(r^2) \gamma_{\alpha\beta} - (\pi\sin^2\theta)(r^2)\gamma_{\alpha\alpha} \quad (21)$$

and

$$\gamma_{\alpha\alpha} = 2\gamma_{\alpha\beta}\cos\theta \quad (22)$$

where $\gamma_{\alpha\alpha}$ is grain boundary interfacial energy, $\gamma_{\alpha\beta}$ the matrix/precipitate interfacial energy, and θ the contact angle. Minimization of eq.(21) with respect to r , gives

$$\Delta G_b^* = ((16\pi \gamma_{\alpha\beta}^3)/(3)(\Delta G_v)^2) ((2-3\cos\theta+\cos^3\theta)/2) \quad (23)$$

2.2.4 Refinement of Precipitates

Refinement of structure is often the principal means for improving the mechanical properties of precipitation hardenable alloys, and the nucleation rate is the controlling factor in precipitate refinement. The mechanism for enhancing the nucleation rate can be related to the general equation for the heterogeneous nucleation rate[16]

$$\dot{N}_{het} = K \exp (-\Delta G^* f(\theta)/kT) \quad (24)$$

where θ is the contact angle in the balance of interfacial tensions given by

$$f(\theta) = (2-3\cos\theta+\cos^3\theta)/4 \quad (25)$$

As in the case for homogeneous nucleation, the parameter K includes the embryo surface concentration of solute atoms and the jump frequency for the atom, which has exponential dependence on the activation energy for atom transfer across the interface. Nucleation rates

can be increased by either decreasing the activation energy for the atom transfer process, which is related to the point defect concentrations at the precipitate/matrix interface, or reducing the free energy of formation for a stable nucleus, ΔG^* . For heterogeneous nucleation, the number and distribution of available defects, which act as nucleation sites, is an important factor influencing the nucleation rate.

The highest rate of nucleation corresponds to the smallest possible ΔG^* . Thus, any changes in one or more of the parameters determining ΔG^* , i.e., interfacial energy, strain energy, and transformation free energy, will strongly alter the nucleation rate because of its exponential dependency on ΔG^* .

2.2.5 Nucleation Entropy Concept

The entropy change during nucleation was first considered by Youdelis[24,2] to account for the variation of undercooling with composition of binary alloys during solidification[24], and the enhanced grain refinement of Al-Ti alloys obtained when microalloyed with Si[2] and Be[3]. It was shown that the refinement could be related to the increase in the magnitude of the nucleation entropy (ΔS_v), and thereby the nucleation rate (c.f.eq.(5)).

Youdelis[24] has derived an expression for the nucleation entropy (ΔS_v) for transformations for the special case of regular solution behavior for binary alloy phases, assuming isothermal, isobaric, and constant phase composition conditions are maintained during nucleation. For the case of solidification, the molar entropy of nucleation is separated into the entropy change due to the freezing of the pure components (ΔS_F), and the change

in the mixing entropy for the solid/liquid system resulting from the precipitation of the solid phase (ΔS_M), given by

$$\Delta S = \Delta S_F + \Delta S_M \quad (26)$$

$$\Delta S_F = N_1^s (S_1^s - S_1^l) + N_2^s (S_2^s - S_2^l) \quad (27)$$

and

$$\Delta S_M = R (N_1^s \ln(N_1^l / N_1^s) + N_2^s \ln(N_2^l / N_2^s)) \quad (28)$$

where the N 's refer to the mole fractions, the S 's to the molar entropies, the subscripts 1,2, to the components, and s, l to the solid and liquid phases respectively.

For a multicomponent system, ΔS is obtained by including terms for all components (r) in the system, i.e.

$$\Delta S_F = \sum N_r^s (S_r^s - S_r^l) \quad (29)$$

$$\Delta S_M = R \sum N_r^s \ln (N_r^l / N_r^s) \quad (30)$$

where N_r^s and N_r^l refer to the mole fractions of the r th component in the solid and liquid phases, and S_r^s and S_r^l are the molar entropies of the r th component in the solid and liquid states respectively at the nucleation temperature.

The application of eq.(27) and (28) to simple binary eutectic systems shows the ΔS_M is always negative, and $|\Delta S_M|$ increases with increasing separation of the solidus and liquidus lines, and for a eutectic alloy is maximum at the eutectic composition. Thus, it follows that

the nucleation rate (and thus grain refinement) should increase with solute concentration for a binary eutectic system (cf.eq.(5)).

The behaviour of ΔS_F and ΔS_M for the multicomponent system is similar to that for the binary system, i.e., both ΔS_F and ΔS_M are always negative, and $|\Delta S_M|$ increases with difference in composition between solid and liquid phases. This is particularly so for the precipitation of intermediate compounds or phases of limited solubility range, when only the principal component (solvent 1) is concentrated in the liquid phases ($N_1^l > N_1^s$), and the remaining minor components (solutes 2,3,..., n), which are present in dilute concentrations in the liquid, are concentrated in the solid phase ($N_r^l < N_r^s$, $r=2,3,\dots, n$), so that only the first term in eq.(30) is positive (decreasing $|\Delta S_M|$), while the remaining terms are negative. In general, since a redistribution of all components necessarily occurs during the nucleation of the primary phase or intermediate compound in the liquid alloy, it follows that the nucleation entropy and corresponding nucleation rate (other factors being equal) increase with the number of components comprising the alloy system.

Compound formation usually concentrates in the compound one or more components present in dilute concentration in the alloy, e.g., Ti concentrates in $TiAl_3$ when precipitated from dilute Al-Ti alloys, so the nucleation entropy is particularly significant in nucleation of intermediate compounds. Youdelis[2] has developed a method for determining the nucleation entropy of intermediate compounds, or phases of limited solubility, which do not have regular solution behaviour. For a pure metal $\Delta S_v (= \Delta H_v/T)$ is readily calculated. In a two (or more) component alloy system, ΔS_v is more difficult to obtain for the nucleation of a phase due to the redistribution of solute between the phases, and the general nonideality of the system. The

problem is solved in two stages: first, regular solution behaviour is assumed for both phases, for which the nucleation entropy is readily formulated. Then the regular solution constraint is removed by a suitable combination of reactions that includes the compound formation reaction and (known) formation entropy.

The role of nucleation entropy in determining the nucleation rate and the degree of structure refinement has been confirmed in several investigations[2,3,6,24,50,51]. The enhanced grain refinement of Al-Ti alloys by third element additions of Si or Be has been attributed to the concentration of Si and Be in the peritectic compound TiAl_3 [2,3], which increases the nucleation entropy and nucleation rate of the compound, that subsequently undergoes the peritectic reaction to form the Al grains[52].

The nucleation entropy concept has also been successfully applied to account for the refinement of carbides in Co-base (HS21) superalloy by small additions of Ta and Nb[50]. It was shown that when Ta or Nb is added to the superalloy, the primary M_{23}C_6 -type carbide, with the approximate stoichiometric formula $(\text{Cr}_{0.77}\text{Co}_{0.15}\text{Mo}_{0.08})_{23}\text{C}_6$, is replaced by the MC-type carbides, TaC or NbC, which have significantly higher nucleation entropies and rates than the M_{23}C_6 carbides. In a similar study of Ni-base superalloy (713C), the addition of Ta or Nb did not alter the basic MC type structure of the primary carbides in the alloy $(\text{Nb}_{0.77}\text{Ti}_{0.23})\text{C}$ [51], and although there was some replacement of Ti in the carbide by Ta or Nb, it did not significantly change the nucleation entropy or nucleation rate. The experimental results showed no refinement of the primary carbides in the Ni-base alloy by the Ta or Nb addition, in agreement with nucleation entropy calculations.

For precipitation in the solid state, the general equations (29) and (30) still apply,

except that the freezing entropy change (ΔS_F) for the pure elements is replaced by the entropy change for the transformation (ΔS_T) of the elements comprising the precipitate from the solid solution structure to the precipitate structure[6].

2.3 Kinetics of Precipitation Processes

For isothermal transformations in the solid state involving nucleation and precipitate growth, the kinetics are generally described by the Avrami-Johnson-Mehl (AJM) equation, usually expressed in the form

$$Y=1-\exp(-kt^n) \quad (31)$$

where Y is the fraction transformed, n is the growth parameter determined by the growth mechanism and precipitate morphology, and k is a nuclei density-dependent parameter. Equation (31) was first applied by Avrami[53] and Johnson and Mehl[54] to recrystallization, in which solute diffusion is essentially absent. The use of eq.(31) was later extended by Wert and Zener[55] to diffusion-limited precipitation reactions, where the parameter k includes the solute diffusion coefficient and (for 3-dimensional growth) is given by

$$k=a(N_0 r_f D)^{3/2} \quad (32)$$

where a is a constant, N_0 the nuclei density, r_f the mean final radius of the particle, and $D(=D_0 \exp(-Q/RT))$ the solute diffusion coefficient. Substituting eq.(32) into eq.(31) gives

$$k = a(N_0 r_f D_0)^{3/2} \exp (-3Q/2RT) \quad (33).$$

where Q is the diffusion activation energy.

The use of eq.(31) to describe the kinetics of various solid state transformations has become commonplace. However, precipitation is a complex process involving nucleation, interfacial reactions, and diffusion-limited growth, and inferring the rate-controlling mechanisms from the activation energy magnitude alone is difficult and can be misleading. This has been convincingly shown by Berkenpas et al[56], who show that when nucleation and growth occur simultaneously, the activation energy obtained from an Arrhenius-type plot for the rate data may be for some reactions the sum of the positive and negative energy values for the nucleation and diffusional growth mechanisms. Accordingly, they recommend that the practice of reporting activation energy for overall transformations should be avoided unless the stages of the transformation which contribute to Q are unequivocally identified.

2.3.1 Modified Avrami-Johnson-Mehl Equation

Youdelis and coworkers[57,58] have shown that solid-state transformation kinetics can be more usefully described using the modified form of the AJM equation

$$Y = 1 - \exp(-k_1 t^n) \quad (34)$$

where k_1 replaces k in eq.(31). The parameter (n) is determined by the growth mode and particle shape (rod, disc, or sphere). The Arrhenius treatment of the rate data using eq.(34)

more directly yields the activation energy for the rate controlling process (e.g. unidimensional diffusion), and is more useful for the study of nonisothermal kinetics using differential scanning calorimetry (DSC)[57,58].

The kinetic parameters (n) and (k_1) are obtained from the logarithmic plot of eq.(34), thus

$$\log \ln (1/(1 - Y)) = n \log t + n \log k_1 \quad (35)$$

which is a straight line function with (n) obtained from the slope and (k_1) from the intercept.

For diffusion-independent transformations (e.g., recrystallization grain growth), where nucleation is fast and not rate controlling, k_1 has the form

$$k_1 = k_{10} \exp (- Q_1/RT) \quad (36)$$

where Q_1 is the activation energy for an atom jump across the grain boundary (grain boundary diffusion), and k_{10} a parameter which includes nuclei density, strain energy, and entropy dependent terms.

For diffusion-limited precipitation reactions, the precipitate growth rate will have a $(Dt)^{1/2}$ dependence for each principal growth direction[59], and when using the modified AJM eq.(34) to describe 3-dimensional growth, k in eq.(33) is replaced by

$$k_1 = a(N_o r_f D_o)^{3/2} \exp (- Q_1/RT) \quad (37)$$

Note that eq. (33) gives a slope $(-3Q/2R)$, while using the modified AJM equation with k replaced by k_1^n , gives a slope (Q_1/R) . Thus the Arrhenius treatment of the rate data (k_1) more directly yields the activation energy for the singular (unidimensional), diffusion rate-controlling process, and is preferred to avoid possible erroneous interpretations of the activation energies obtained when using eqs.(31) to (33).

2.4 Aluminum Alloy Systems

The aging of Al-Mg-Si and Al-Mg-Si alloys containing Be involves the precipitation of several metastable and stable phases. The following is a brief description of the known binary and ternary phase diagrams, and the precipitates formed in the Al-Mg, Al-Si, Al-Mg-Si, Al-Be, Al-Si-Be and Al-Mg-Be alloy systems.

2.4.1 Aluminum-Magnesium System

The equilibrium solid phases of the Al-Mg system shown in Fig.1 are: (i) fcc Al(α), with a maximum solubility of Mg in Al of 18.9 at.% at the eutectic temperature 450°C; (ii) hcp Mg(δ) solid solution, with a maximum solubility of Al in Mg of 11.8 at.% at the eutectic temperature 437°C; (iii) β compound with the approximate stoichiometry Al_3Mg_2 , which has a complex fcc structure (at low temperature, β -phase transforms martensitically to another structure that may be a distortion of the β structure); (iv) the line compound R (sometimes designated ϵ) with composition 42 at.%Mg; and (v) the compound γ , with α -Mn structure, which has composition range 45 to 60 at.%Mg at 450°C (the ideal crystal structure has the stoichiometry $Al_{12}Mg_{17}$ at 58.6at.%Mg[60]). Solid solutions of Al-Mg alloys show an

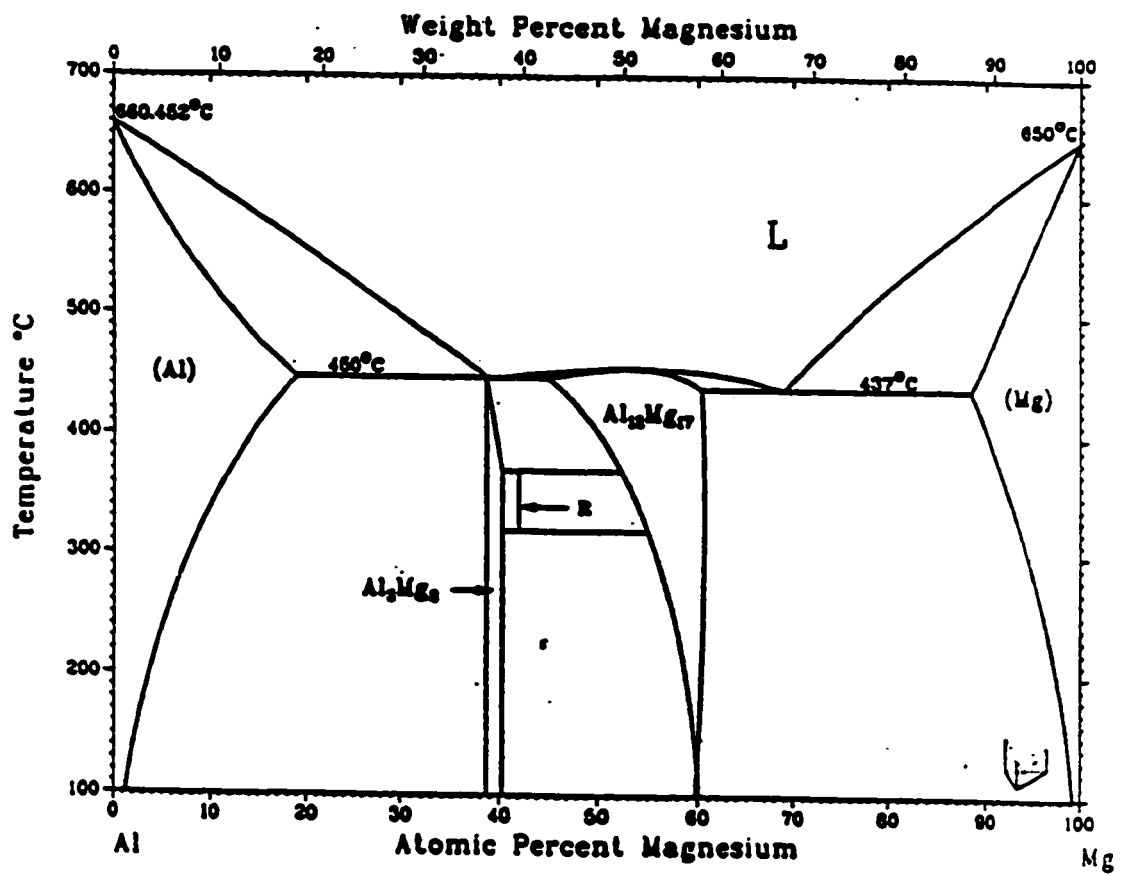


Fig.1 Aluminum-Magnesium phase diagram (after Murray [60]).

expansion in the Al(α) lattice parameter, e.g., for 2.75at.%Mg, the lattice parameter is 0.40521nm at room temperature[61], compared to 0.40494nm for pure Al.

2.4.2 Aluminum-Silicon System

The binary Al-Si phase diagram shown in Fig.2 is a simple eutectic system with one solid solution phase, fcc Al(α), with a maximum solubility of Si in Al of about 1.5at.% at the eutectic temperature 577°C, and diamond cubic Si with negligible solid solubility of Al[62]. The eutectic reaction $L \rightleftharpoons Al + Si$ occurs at approximately 12.2 at.%Si. Silicon in solid solution decreases the lattice parameter of Al(α), e.g., for 0.74 at.%Si Al(α) has a lattice parameter of 0.40400 nm[63].

2.4.3 Aluminum-Magnesium Silicide System

The quasibinary Al-Mg₂Si equilibrium diagram [64] shown in Fig.3 is relatively simple and well established. The compound Mg₂Si is in equilibrium with Al, and the quasibinary line Al-Mg₂Si in the ternary diagram occurs at the Mg/Si ratio of 1.73 (Fig.4). The binary and ternary invariant reactions at the Al end are shown in Table 1 [65].

The Si, Al₃Mg₂ (β) and Mg₂Si phases in the reactions do not differ substantially from stoichiometric compositions. The solid solubility of Mg₂Si in Al(α) is reduced only slightly with Si above the Mg/Si ratio of 1.73, but an excess of Mg greatly reduces Mg₂Si solubility[65]. As Mg expands and Si contracts the lattice parameter of Al(α) solid solution, the lattice of the ternary Al(α) solid solution may increase or decrease depending on the ratio of Mg/Si[66].

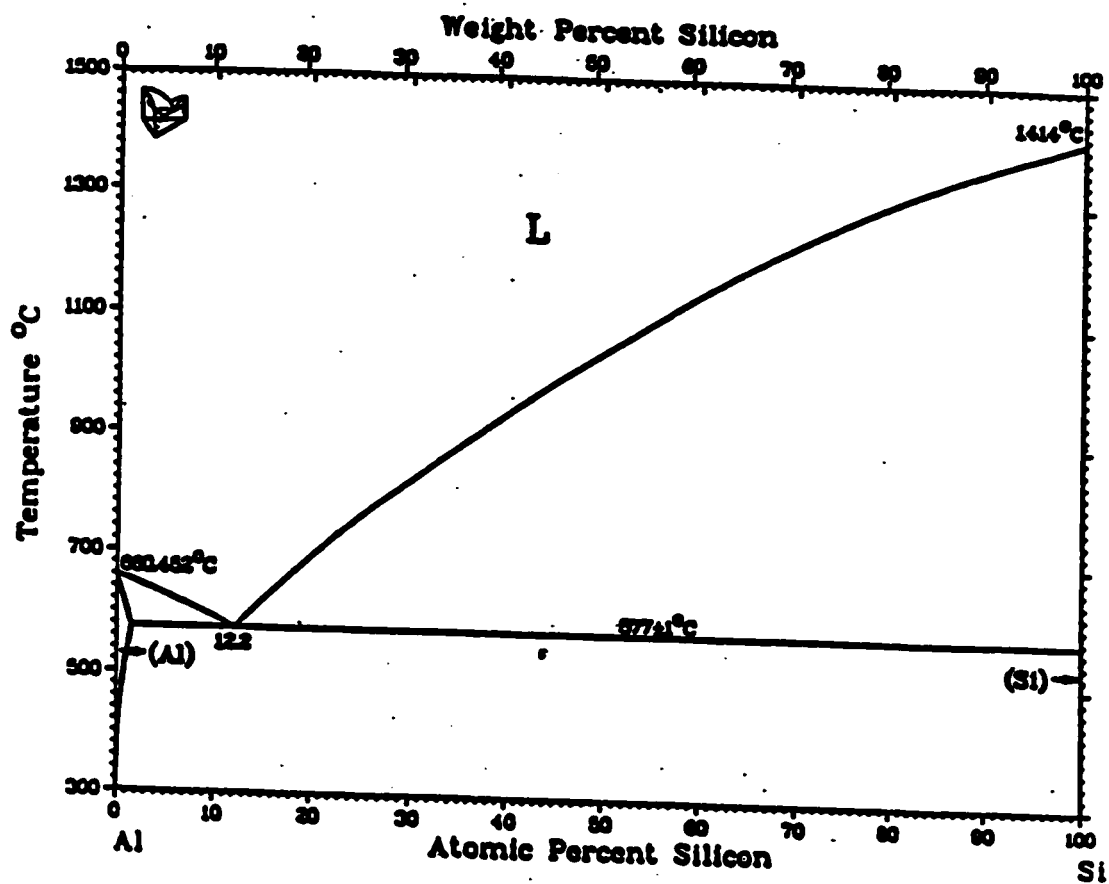


Fig.2 Aluminum-Silicon phase diagram (after Murray and McAlister [62]).

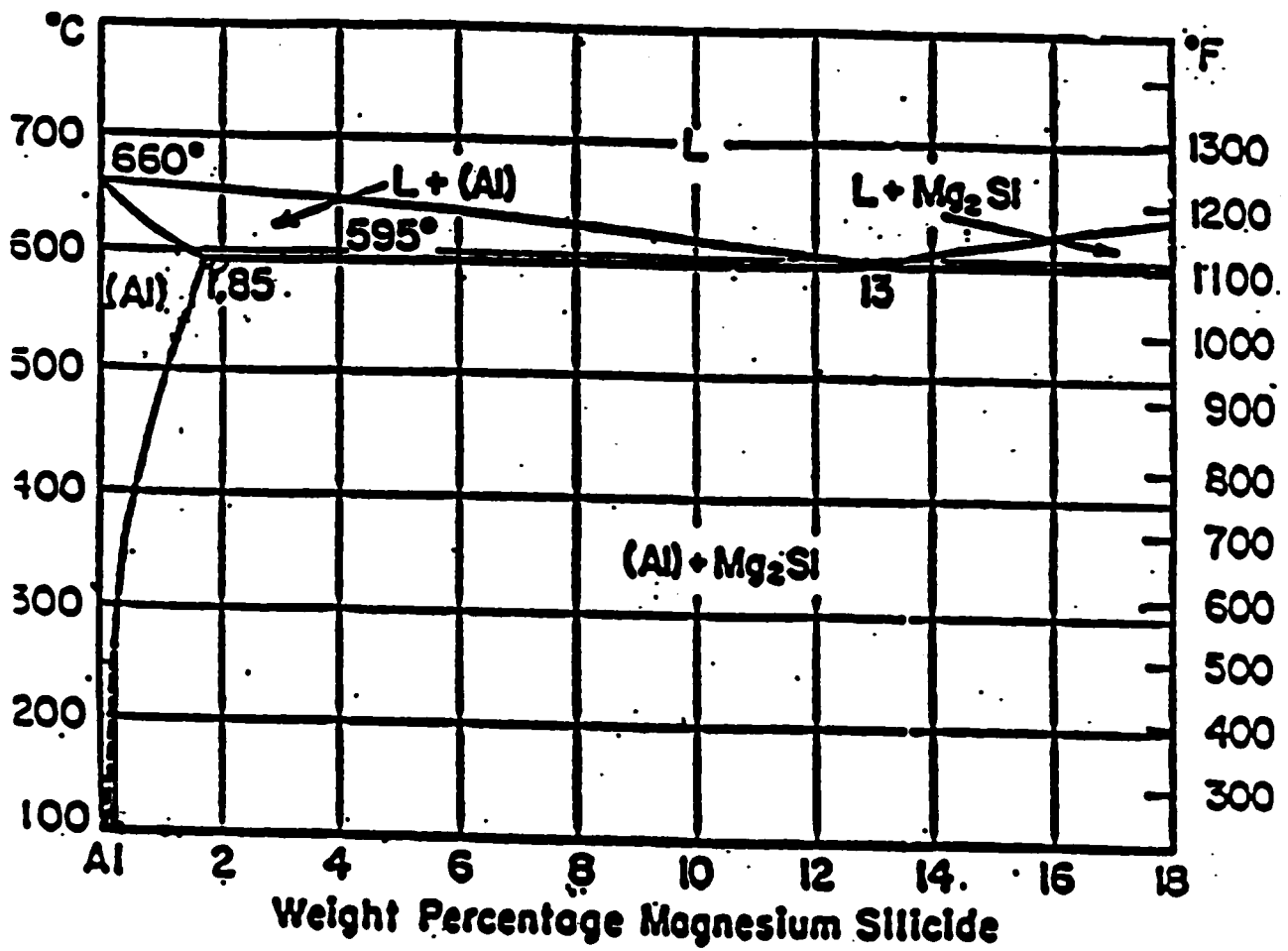


Fig.3 Aluminum-Magnesium Silicide quasibinary phase diagram (after Anderson [64]).

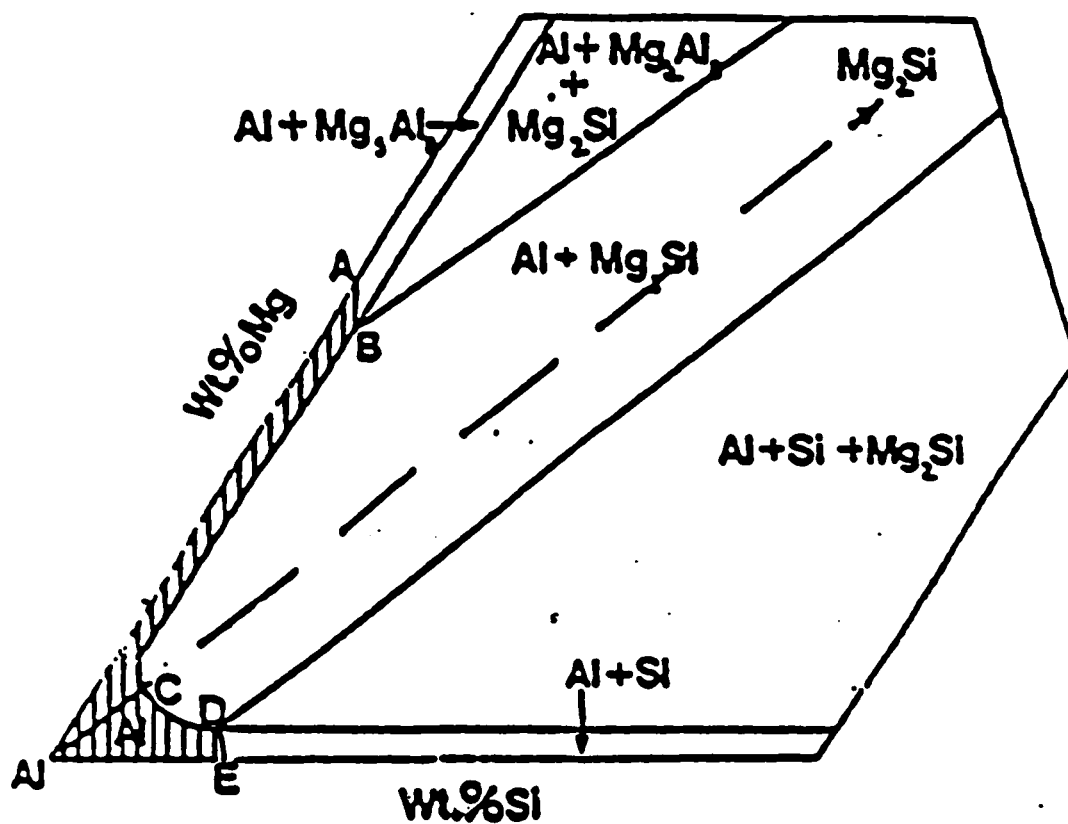


Fig.4 Partial Aluminum-Magnesium-Silicon ternary phase diagram (after Mondolfo [65]).

Table 1 Invariant reactions at the Al end of the Al-Mg-Si diagram (after Mondolfo[65]).

Reactions	Temperature, °C	Liquid		Al(α)	
		%Si	%Mg	%Si	%Mg
(A) $L \rightleftharpoons Al + Al_3Mg_2$	450	---	34.0	---	17.4
(B) $L \rightleftharpoons Al + Mg_2Si + Al_3Mg_2$	449	0.37	32.2	0.05	15.3
(C) $L \rightleftharpoons Al + Mg_2Si$	595	4.75	8.15	0.68	1.17
(D) $L \rightleftharpoons Al + Mg_2Si + Si$	555	12.95	4.96	1.10	0.85
(E) $L \rightleftharpoons Al + Si$	577	12.5	---	1.65	---

2.4.4 Aluminum-Beryllium System

The binary Al-Be phase diagram shown in Fig.5 is a simple eutectic system with two solid solution phases, fcc Al(α) with a maximum solubility of Be in Al of about 0.3 at.% at the eutectic temperature 644°C, and hcp Be with negligible solid solubility for Al. The eutectic reaction $L \rightleftharpoons Al + Be$ occurs at 2.5 at.%Be[67]. The incorporation of Be in Al(α) results in a contraction in the lattice parameter; e.g., for 0.06%Be the lattice parameter is 0.40411 nm at room temperature[68].

2.4.5 Aluminum-Silicon-Beryllium System

According to Nowotny [69], the system is a simple eutectic one in which neither binary nor ternary compounds are formed. The ternary Al-Si-Be phase diagram (Fig.6) in the Al corner consists of two binary Al-Si and Al-Be eutectics, and a ternary eutectic, $L \rightleftharpoons Al + Be + Si$, at approximately 12-13 %Si and 1-1.5 %Be at 845°K.

2.4.6 Aluminum-Magnesium-Beryllium System

The partial ternary phase diagram for the Al-Mg-Be system, as determined by Nagorskaya et al [70], is shown in Fig.7. A ternary eutectic, $L \rightleftharpoons Al + Be + \beta(Al_3Mg_2)$, occurs at ~35%Mg and ~0.6%Be, at 445±3°C. Fig.7 shows that the solubility of Mg in Al(α) decreases as the Be content increases, and that no ternary compounds are formed. Nagorskaya et al [70] and Fridlyander et al [71] report some dissolution of Be in the binary β phase. The lattice parameter of the Al solid solution quenched from 440°C is 0.41032nm[72].

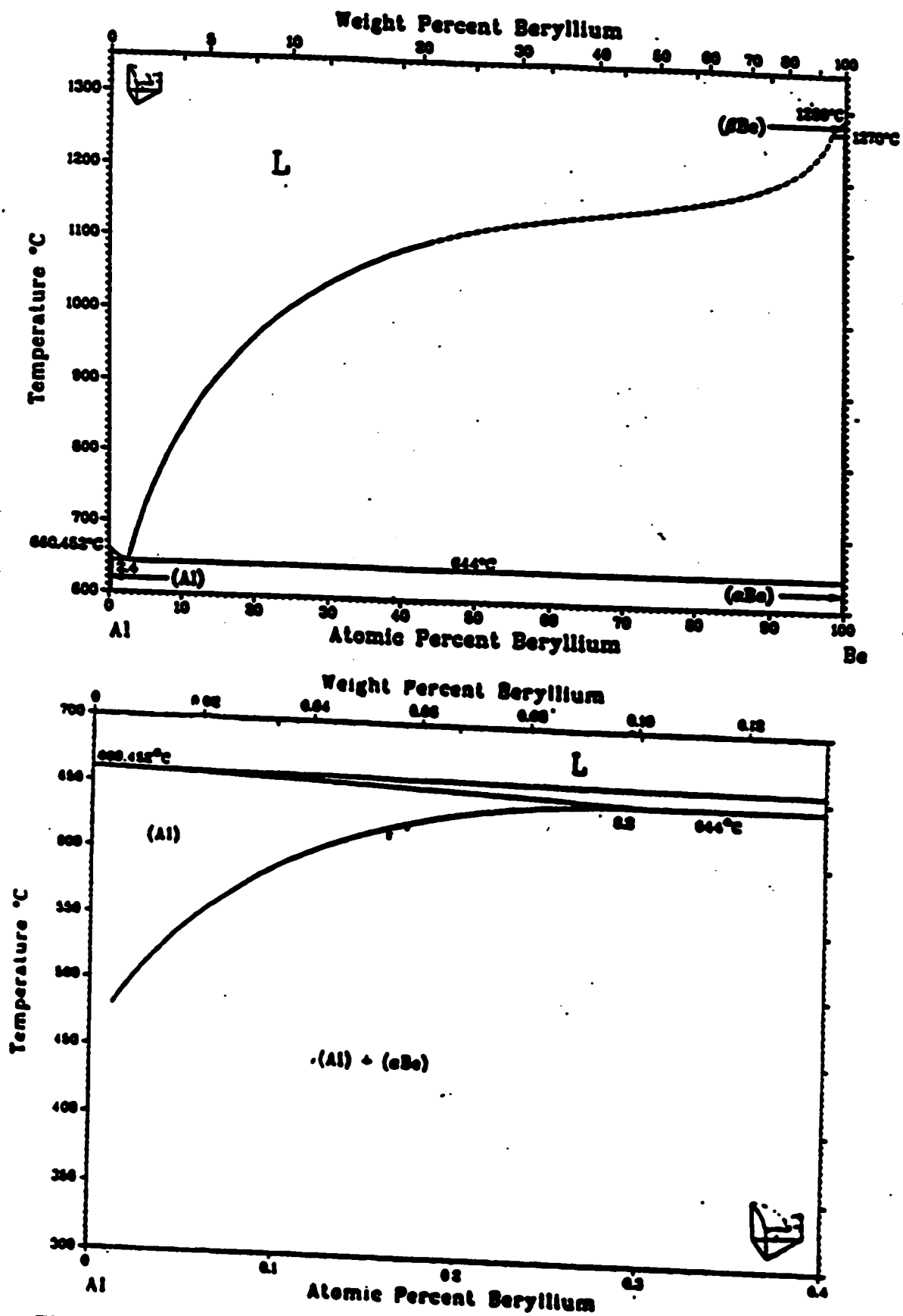


Fig.5 Aluminum-Beryllium phase diagram (after Murray and Kahan [67]).

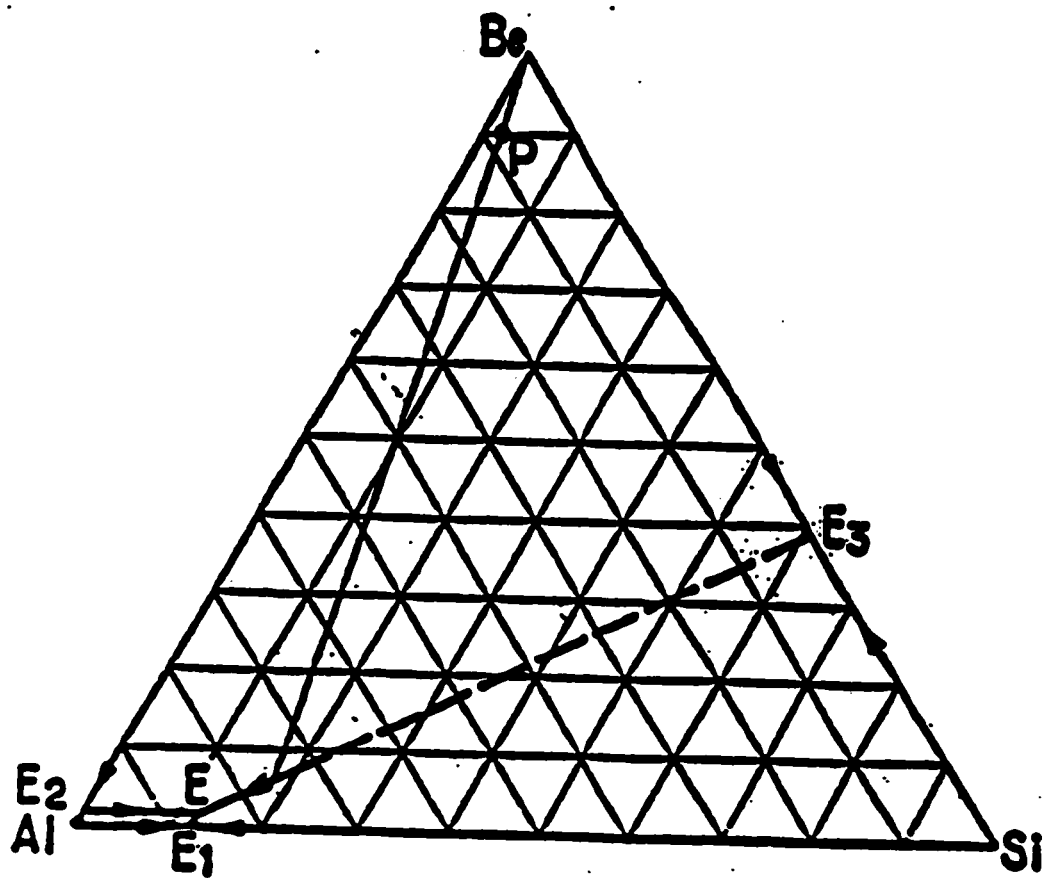


Fig.6 Aluminum-Silicon-Beryllium phase diagram (after Nowotny [69]).

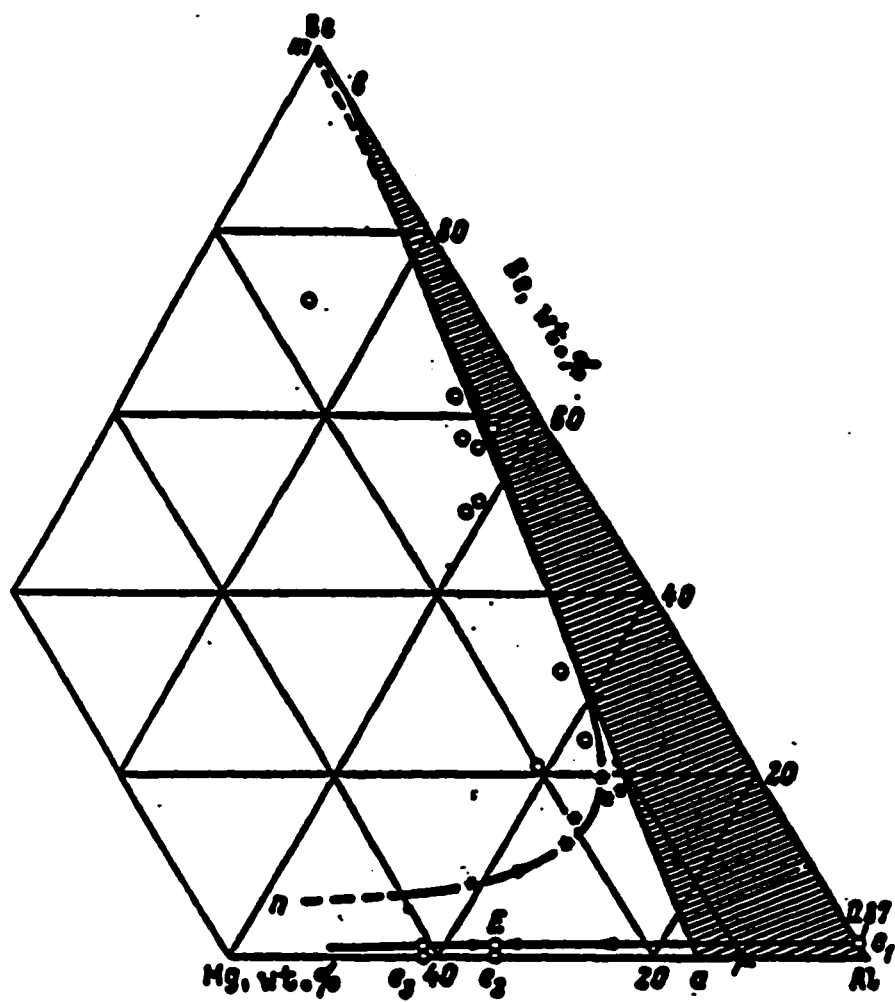


Fig.7 Partial Aluminum-Magnesium-Beryllium phase diagram (after Nagorskaya [70]).

2.5 Precipitation Stages in Al-Mg-Si Alloys

The Al-Mg-Si system is the basis of a major class of heat treatable alloys used for both wrought and cast products. These alloys combine many favorable characteristics, including moderately high strength, relatively low quench sensitivity, and good corrosion resistance. The more dilute alloys are frequently used for architectural applications, usually in the form of extruded sections, which are not solution-treated before artificial aging.

Age-hardening curves for Al-Mg-Si alloys may exhibit two or more stages for the precipitation process, the number of stages depending on the aging temperature. It is generally accepted that the first transformation stage during aging of precipitation hardenable alloy is the formation of GP zones, which initiate at solute clusters. As aging progresses, the GP zones grow in size and transform to the metastable intermediate precipitates (β'' and β' -phases), which finally take on the structure of the equilibrium β (Mg_2Si) phase. Dutta et al[73], in a study of 6061 alloys using differential scanning calorimetry (DSC) and a transmission electron microscope (TEM), have proposed a more detailed transformation of the intermediate phases as follows

Vacancy-Si clusters \Rightarrow GP-I zones \Rightarrow GP-II zones or β'' -needles \Rightarrow β' -rods \Rightarrow β -plates (38)

Other studies[74] show that the precipitation sequence may be adequately represented by

Clusters \Rightarrow GP zones \Rightarrow β' -rods \Rightarrow β -plates (39)

2.6 Structural Aspects of the Precipitating Phases in Al-Mg-Si Alloys

2.6.1 GP Zones

Guinier-Preston (GP) zones are solute-rich and coherent with the matrix. The earlier X-ray diffraction studies[75,76] suggested that GP zones are needle-shaped along $\langle 100 \rangle$ of the matrix, are composed of layers of one row of Si atoms bounded by two rows of Mg atoms, and are 1-2nm wide and ~10nm long. Thomas[74] reported a density of needle shaped zones with $\langle 100 \rangle$ growth direction $\sim 2.5 \times 10^{15} / \text{cm}^3$. A single crystal X-ray study by Lutts[77] of Al-Mg-Si alloys showed that when aging at 135° or 150°C zone formation took place in two stages. The first zones to form were reported to contain a high vacancy concentration but did not exhibit any sign of internal order or periodicity. During subsequent aging a periodicity identical to that of the matrix developed along the zone axis; this was accompanied by a sharp decrease in the vacancy concentration of the zones. Smith[78] observed a duplex precipitate morphology consisting of both spherical and needle-shaped GP zones.

2.6.2 β'' and β' Transition Phases

The intermediate metastable (β'' and β') phases are partially coherent precipitates and have different crystal structures from the matrix. Lynch et al[79] reported that the structure of β'' is a monoclinic unit cell, with $a=0.30\text{nm}$, $b=0.33\text{nm}$, $c=0.40\text{nm}$, $\alpha=\beta=90^\circ$, and $\gamma=71^\circ$ with the orientation relationship $[001]_{\beta''} \parallel [001]_{\text{Al}}$. Dutta et al[73] propose that β'' grow to β' rod-shaped precipitate about 5.0-7.5nm in diameter and 50.0nm in length. Electron microscope studies[79-81] confirmed that the structure of β' is a hexagonal unit cell, with

$a=0.705\text{nm}$, $c=0.405\text{nm}$, and an orientation relationship $\{100\}_{\beta} \parallel \{100\}_{\text{Al}}$, $\langle 110 \rangle_{\beta} \parallel \langle 100 \rangle_{\text{Al}}$.

2.6.3 β Equilibrium Phase

The stable equilibrium β phase (Mg_2Si , 63.2%Mg and 36.8%Si) is cubic (fcc), with a CaF_2 structure, space group $\text{Fm}\bar{3}\text{m}$, 12 atoms in the unit cell, and a lattice parameter $a = 0.635\text{-}0.640\text{ nm}$. The reported melting point, Vickers hardness, and density for Mg_2Si are 1085°C , 459 kg/mm^2 , and 1.88 gm/cm^3 [65] respectively. Thomas[74] and Jacobs[80] showed that the β phase forms as platelets on the matrix $\{100\}$ planes, with an orientation relationship $(100)_{\beta} \parallel (100)_{\text{Al}}$, $[110]_{\beta} \parallel [100]_{\text{Al}}$.

2.6.4 Trace Element Effects

It is well known that minor or trace amounts of elements can significantly alter the binary phase diagrams, and precipitate highly insoluble binary compound precipitates. For example, Youdelis[2] has shown that small amounts of Si significantly reduces the Ti concentration for the peritectic reaction to occur in Al-Ti alloy, and results in Si incorporation into the TiAl_3 compound. Both effects have the net result of increasing the nucleation rate of TiAl_3 , and ultimately enhancing grain refinement. Youdelis and Fang [4] have calculated the Al corner of the ternary Al-Ti-Be phase diagram using thermodynamic data calculated from the binary diagrams, known thermochemical data for compounds, and free energies of formation for binary compounds. It was shown that small additions of Be transform the isothermal peritectic reaction for the Al-Ti binary to a monovariant reaction in which secondary Al crystals are formed over a temperature range, and that Be and Ti severely

restrict their mutual solubilities in solid Al, precipitating as TiBe_{12} . The effects of Be on the Al-Ti system has been investigated by Youdelis and Yang [3], who show that the addition of small amounts of Be markedly enhances the grain refinement of Al by Ti. It was shown that Be is incorporated into the peritectic compound TiAl_3 , and that the ternary compound $\text{Ti}(\text{Al},\text{Be})_3$ has a higher nucleation entropy and a corresponding significantly higher nucleation rate.

It is evident that small amounts of trace elements may modify the nucleation of precipitates, and thus exert large effects upon the structure and properties of age hardening alloys. Several mechanisms by which additions of trace elements modify the nucleation mechanism and compositions of precipitates have been reviewed by Polmear[82]. These include:

(a) trace elements may interact with vacancies, leading to a reduction in the rate of lattice diffusion of substitutional elements. Thus the marked effects of small amounts of Cd, In and Sn in reducing the rate of GP zone formation in Al-Cu alloys is attributed to this type of interaction; (b) trace elements may modify the interfacial energy (γ) between a precipitate and the matrix, thereby changing the nucleation rate of the phase; (c) trace elements may change the free energy relationships in an alloy system, so that precipitation of a different phase is favoured. It has been shown that the addition of 0.1 at.%Ag to Al-Cu-Mg alloys induces homogeneous nucleation of a ternary T-phase ($\text{Al}_6(\text{Cu},\text{Ag})\text{Mg}_4$) instead of the normal GP zones, and the S'-phase (Al_2CuMg) is nucleated on dislocations[83].

2.7 Be Effect on Precipitation in Al-Mg-Si Alloys

The effect of Be microadditions on Mg_2Si precipitation in age hardenable Al-0.75%Mg-0.50%Si alloy has been investigated by Xiao and Youdelis[11,12]. A study of the precipitation kinetics (using resistivity) showed that in both the Be-free and Be-containing alloys, Mg_2Si precipitation obeys the Avrami-Johnson-Mehl equation[53,54]. It was shown that an addition of 0.1%Be to the alloy significantly increases the transformation rate reflected in a higher nuclei density-dependent parameter(k). The enhanced age hardening rate and hardness for the Be containing alloy is associated with a significant increase in the density of precipitate particles. The higher k value and precipitate density for the Be-containing alloy is thus attributed to a Be-enhanced nucleation rate. Solubility of Be in the pseudobinary Al-13%Mg $_2$ Si alloy has been investigated by Hatab[13]. It was shown that based on Mg_2Si crystal structure and Be atom size, Be can be incorporated into Mg_2Si phase, and this is supported by X-ray diffraction data. Hatab has also shown that Be replaces some Si in the ternary compound Al_5FeSi .

The effect of small additions of Be to Al-7.0%Si-0.5%Mg-0.1%Fe (A357) alloy has been investigated by Granger et al[84]. They report that in addition to Si and Mg_2Si , the Be-free alloy contains three Fe-rich phases (Al_5SiFe , $\text{Al}_{15}(\text{MnFe})_3\text{Si}_2$, and $\text{Al}_{10}\text{Si}_4\text{Mg}_4\text{Fe}$), while the Be containing alloy has only one Fe-rich phase ($\text{Al}_{15}(\text{MnFe})_3\text{Si}_2$ or $\text{Al}_8\text{Fe}_2\text{Si}$). They also report 12% of the particles are Fe-bearing in the Be-free alloy, compared with 3% in the Be-containing alloy. Using D.S.C.(Differential Scanning Calorimetry) analysis, Granger et al show that the additions of Be lowers the ternary eutectic melting point by 6°C, and that the second (higher) temperature peak, which is a Fe reaction, is effected by the Be addition.

These observations lend further support to the microprobe results, e.g., that the presence of Be reduces the number of Fe-bearing constituents. The above results show that the phase types and distribution in Be-free and Be-containing A357 alloy are significantly different, and the presence of $\text{Al}_{10}\text{Mg}_4\text{Si}_4\text{Fe}$ in the Be-free alloy is responsible for the decrease in strength of the alloy as it reduces the amount of Mg available to form Mg_2Si (the strengthening phase).

The effect of Be and Ti on mechanical properties of a cast Al-Si-Mg alloy has been investigated by Altman et al[85]. Altman et al report that the effect of Be alone increases the grain size of the casting alloy, but the addition of Be and Ti significantly refines the grain size. The highest ultimate strength of the alloys ($\sigma_b = 33.5 \text{ kg/mm}^2$) is obtained for the composition of Al-7.50%Si-0.45%Mg-(0.15-0.40%)Be-0.15%Ti.

The effect of Be and Na on the aging phenomena of Al-Si-Mg alloys has been investigated by Nishi and Shinoda[86], who showed that the additions of 0.09%Be and 0.01%Na affected the formation of GP zones in Al-Si-Mg alloys, and the density of the GP zones increased when Be was incorporated into the GP zones.

CHAPTER 3

EXPERIMENTAL

3.1 Alloy Preparation

Super pure aluminum and magnesium (99.99%), and Al-50%Si and Al-5.23%Be master alloys were used in the preparation of the base alloy (Al-0.7%Mg-0.4%Si) and the base alloy containing 0.4%Be. The alloys were prepared in graphite crucibles, by induction melting in air, using a 15-KVA Ajax inductotherm unit at a frequency of 10kHz. The melts were heated to well above the liquidus temperature ($\approx 750^{\circ}\text{C}$), maintained for 10 minutes and periodically stirred to ensure complete homogenization, and then poured (pouring temperature $\approx 750^{\circ}\text{C}$) into graphite molds (20 mm dia. by 70 mm length) at room temperature. The melt temperature was monitored by a thermocouple embedded in the graphite crucible. The ingots are homogenized at 560°C (under alumina powder for protection against oxidation) for 72hrs. The experimental work was carried out on the central parts of the ingots to ensure minimal variations in microstructures and compositions resulting from solidification segregation.

3.2 Analytical Procedures

3.2.1 Optical Microscopy

Specimens were prepared for microscopical analyses by wet grinding on 240, 320, 400 and 600 grit papers, followed by polishing with $1.0\mu\text{m}$ and then $0.05\mu\text{m}$ alumina, and

finishing with colloidal silica suspension. Specimen etching for microstructure analysis was accomplished by using a solution of 10ml of H_2SO_4 , 5 ml HF (48%) and 85ml H_2O , and Tucker's reagent (45ml HCl, 15ml HNO_3 , 15ml HF (48%) and 25ml H_2O) for macrostructure analysis. A progressive etch was carried out to obtain sufficient topographical contrast. The optical microscope used in this study is a Leitz Labor Lux 12 model, with a maximum objective lens magnification of 1000x.

3.2.2 Transmission Electron Microscopy (TEM)

Thin foils for TEM studies were prepared from the homogenized ingots. Sections (~5mm thick) were reduced to a thickness approximately 1mm in two stages by cold rolling and annealing (400°C). The rolled sections were then solution treated at 560°C for an additional two hours to ensure the maximum supersaturation of Mg, Si, and Be, followed by a quench in ice-brine. Immediately following the quench, the specimens were aged at room temperature and 250°C for 30, 65 and 600 minutes. The processes of annealing, solution and aging treatments were done under alumina powder for protection against oxidation. The aged specimens were mechanically ground on silicon carbide paper to thickness of <75 μm . Discs 3mm in diameter were made from the ground foil sections using a punch tool. The final specimens for TEM analysis were prepared by electropolishing using a double-jet electropolisher (Struers Tenupol-3) and 30% HNO_3 in methanol. The electrolyte temperature was maintained at -40 to -30°C using a dry ice-ethanol bath. A potential of 20 V produced a current of ~200 mA and medium flow rates were used during thinning. Foil thicknesses obtained by the jet technique are reported in the range of 100-300nm[87,88]. The TEM

specimens were examined using a Philips CM12 transmission electron microscope operated at 120 kV.

3.2.3 Microhardness Measurement

Microhardness measurements were used to monitor the age hardening process. Sections about 5mm thick, cut from the central regions of the homogenized ingots, were used for the studies. The solution treatments and aging were carried out under alumina powder using an electric furnace with a temperature control of $\pm 2^{\circ}\text{C}$. The solution treatment consisted of an anneal at 560°C for 2hr., followed by a quench in ice-brine. Immediately following the quench, the specimens were aged at room temperature (25°C), 150, 200, 250, and 300°C . Hardness measurements were made by constantly interrupting the aging treatments. The microhardness measurements were obtained using a Micromet- II with a Digmet microhardness tester readout system, a diamond pyramid indenter, a 100 gram load, and a test time of 20 seconds. Before taking the measurements, the aged specimens were polished using a conventional polishing technique, and at least six randomly located readings were taken for each hardness determination and the age hardening process was repeated three times using new specimens to provide a statistical basis for the mean hardness values.

3.2.4 Resistivity Measurement

For the resistivity study, sections (~5mm thick) were cut from the central regions of the homogenized ingots to ensure similar initial microstructures and compositions. The specimens were cold rolled to strips and annealed (400°C) to remove the cold work. Samples,

72mm by 4mm by 0.2mm thick, were cut from the strips for the resistivity measurements. Before each aging treatment the test samples were again solution treated at 560°C for 2 hrs., followed by a quench in ice-brine. Immediately following the quench, the specimens were aged at room temperature, 150, 200, 250, and 300°C, with aging interrupted periodically for resistivity measurements at room temperature. The annealing, solution, and aging treatments were done under alumina powder to minimize specimen oxidation. A standard potentiometric method was used to monitor the resistivity changes. The ends of the specimens were split (Fig. 8) and connected to the current and potential leads separately to eliminate contact resistance effects, and the potential drops were compared with that of a super pure aluminum strips used as reference. The resistivity measurements were carried out with the specimens immersed in de-ionized water maintained at $29 \pm 1^\circ\text{C}$. The potentiometric facility consisted of a Leeds-Northrup potentiometer, resolution of 10^{-7}V , and a power supply which enabled regulation of the current to $\pm 0.02\%$. Resistivity changes of $10^{-11} \Omega\text{m}$ could be detected, and the overall precision for the readings was $\pm 0.03\%$.

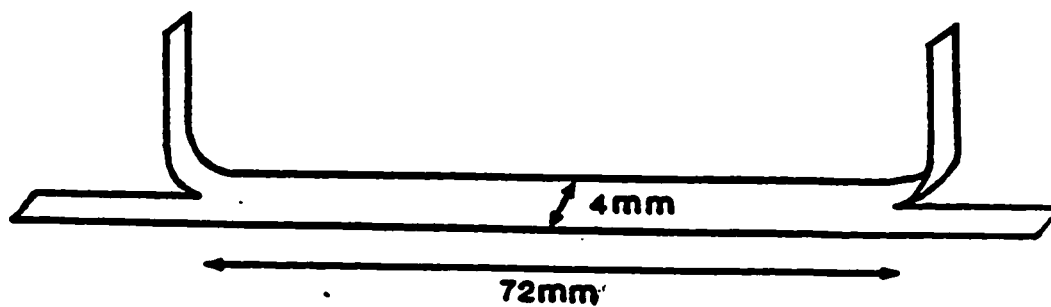


Fig. 8 Resistivity specimen 0.2mm thick.

CHAPTER 4

RESULTS AND DISCUSSION

4.1 Optical Microscopy

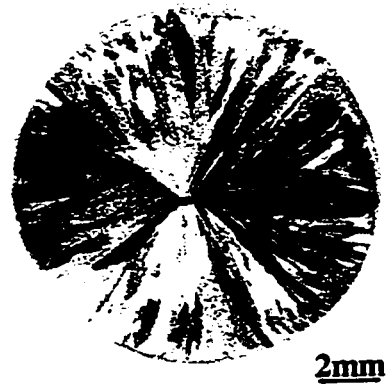
4.1.1 As-Cast Microstructures

The as-cast macrostructures for the base and 0.4%Be alloys are shown in Fig.9(a), and (b). The macrostructure of the Be-containing alloy (Fig.9(b)) shows a larger equiaxed zone, and a decrease in grain size for both the columnar and equiaxed zones of the casting compared with the base alloy (Fig.9(a)). A similar Be-enhanced grain refinement effect was reported for Al-Ti alloys[3]. The as-cast microstructures show β precipitate (Mg_2Si) particles in the grain interiors and at grain boundaries for both base and Be-containing alloys (Fig.10(a) and (b)); however, the latter also shows interdendritic Al-Be eutectic regions (Fig.10(b)). The maximum solubility of Be in Al(α) solid solution for the binary Al-Be system is approximately 0.02% at 560°C (cf., Fig.5), and for the as-cast condition the excess Be forms as interdendritic eutectic regions[90].

4.1.2 Solution Treated and As-Quenched Microstructures

The macrostructures of the solution-treated and quenched alloys are shown in Fig.11(a) and 11(b) for the base and 0.4%Be alloy respectively, and the corresponding microstructures in Fig.12(a) and 12(b). Essentially complete dissolution of the β precipitate has resulted for the base alloy (Fig.12(a)), and for the Be-containing alloy the excess (eutectic) Be has coalesced to form distinct spheroidal/ellipsoidal particles (Fig.12(b)).

(a)



(b)

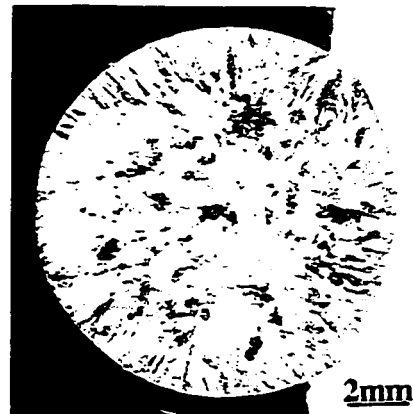


Fig.9 Optical macrographs of the as-cast alloys: (a) base alloy; (b) 0.4%Be alloy.

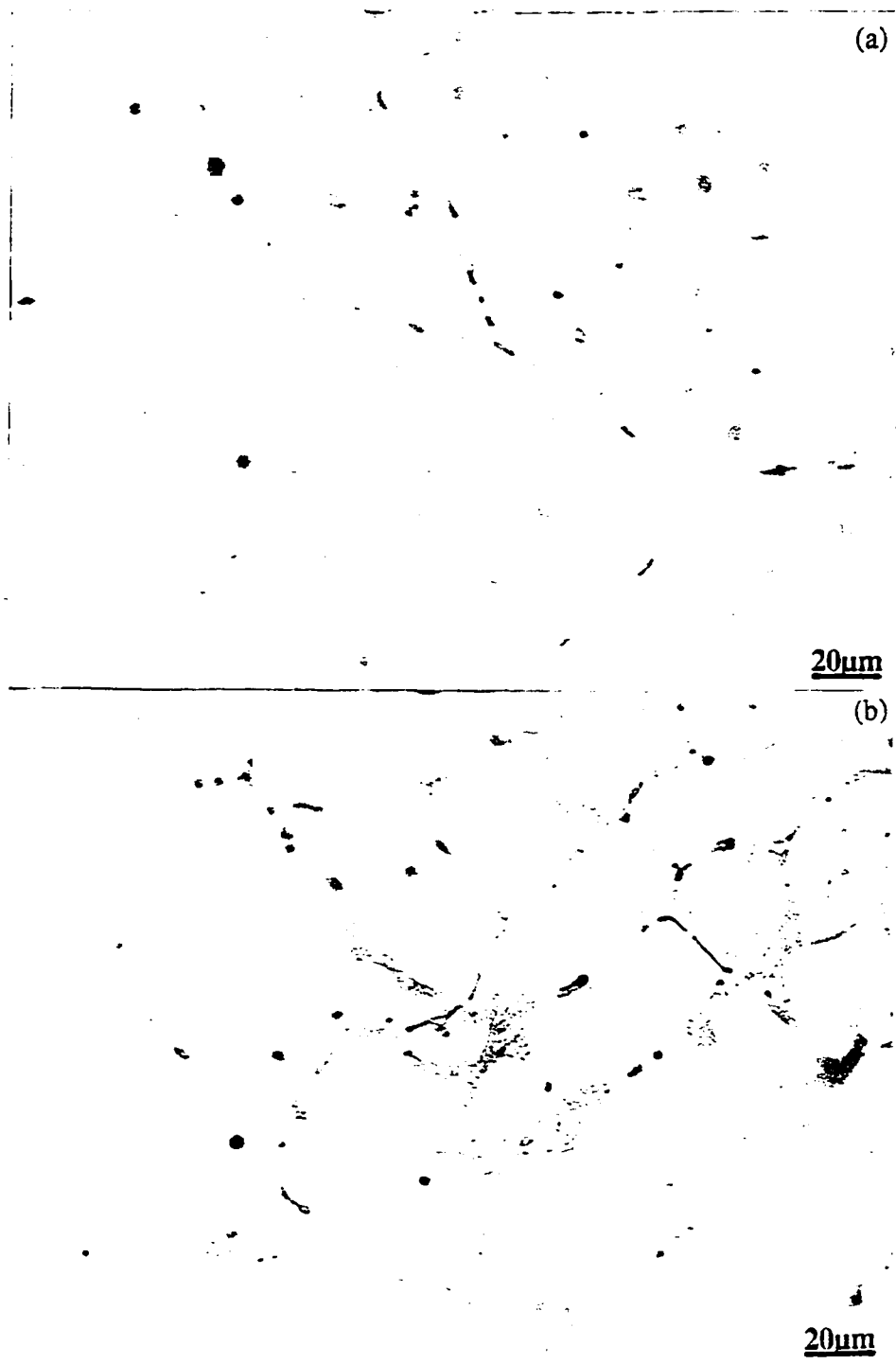


Fig.10 Optical micrographs of the as-cast alloys: (a) base alloy; (b) 0.4%Be alloy.

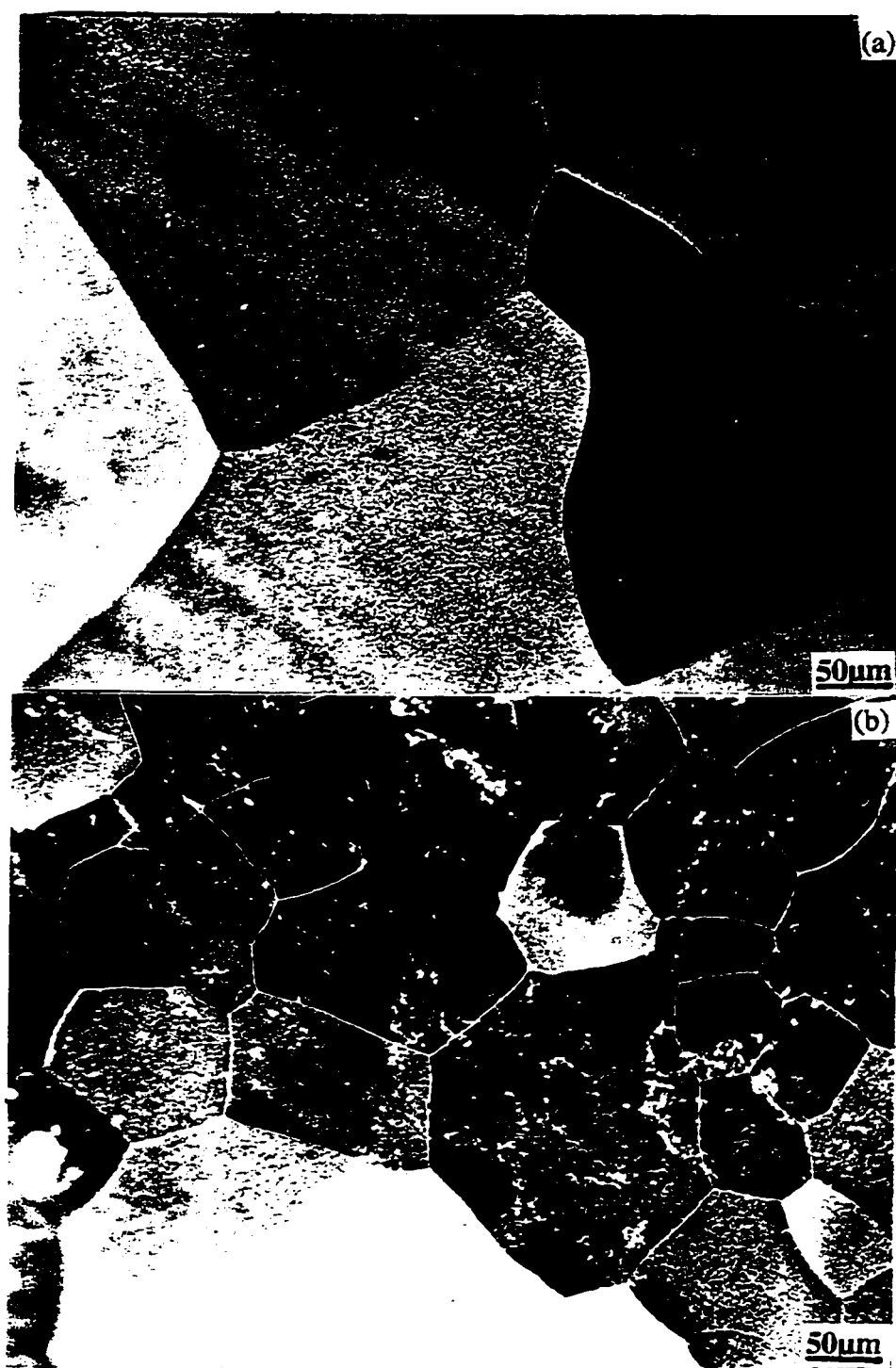


Fig.11 Optical macrographs of the as-quenched alloys: (a) base alloy; (b) 0.4%Be alloy.

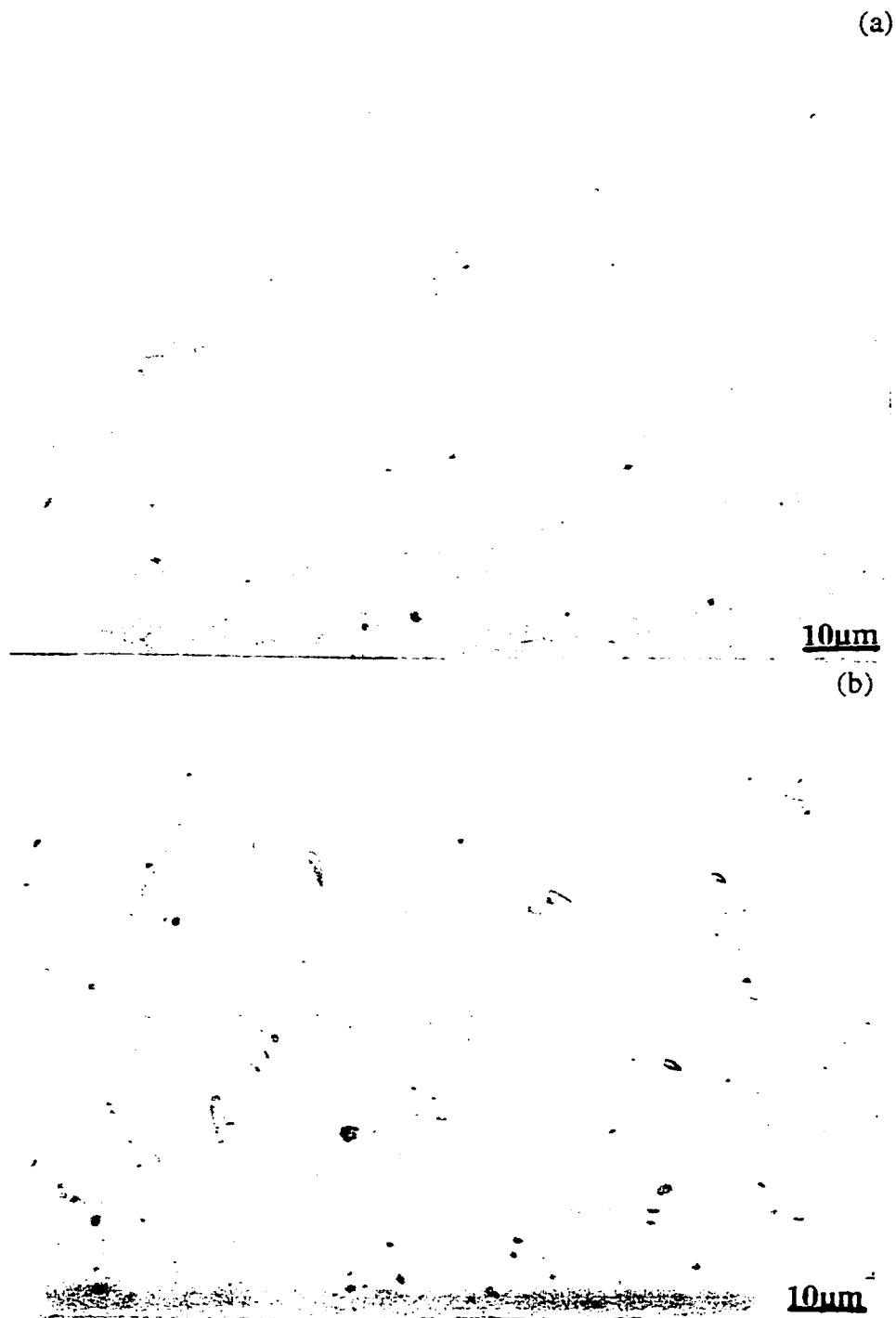


Fig.12 Optical micrographs of the as-quenched alloys: (a) base alloy; (b) 0.4%Be alloy.

Fig. 12(b) also shows the presence of very fine precipitate, some of which may be undissolved Mg_2Si phase, since Be is known to restrict the solid solubility of the alloying elements in Al[4,13].

Fig. 11 (electropolish etch) shows a ~ 3 -fold reduction in the average grain size for the Be-containing alloy (Fig. 11(b)) compared to the base alloy (Fig. 11(a)). The grain refinement is primarily the result of the essentially insoluble Be restricting growth of the primary Al grains during solidification[1]. Although grain coarsening occurred during the 72 hrs homogenization anneal at 560°C , the initial relative grain refinement has been maintained.

4.1.3 Etch Pits at Dislocations

A surface preparation method was used to reveal dislocation etch pits. This was accomplished by electropolishing and then chemical etching. Figs. 13 and 14 show dislocations etch pits for the as-quenched and room temperature aged (for 12 months) alloys respectively. Both alloys show subboundaries (tilt boundary, see A in Fig. 13) as shown by a regularly spaced row of dislocation etch pits formed at a grain boundary (array of edge dislocation). Both dislocation climb and glide are required to produce a tilt boundary. The as-quenched Be-containing alloy shows a significantly higher density of dislocation etch pits (Fig. 13(b)). The presence of dislocation clusters (see B, in Fig. 13(b)) suggest interaction between matrix dislocations and vacancies has occurred[89]. As aging progresses (Fig. 14) the dislocation density decreases, indicating that dislocations migrate to the grain boundaries. The dislocation etch pit density (pits/unit area) determinations were made from optical photomicrographs using a Ladd Microcomputer Image Analyzer, and the accuracy of the calculation is $\sim \pm 15\%$.

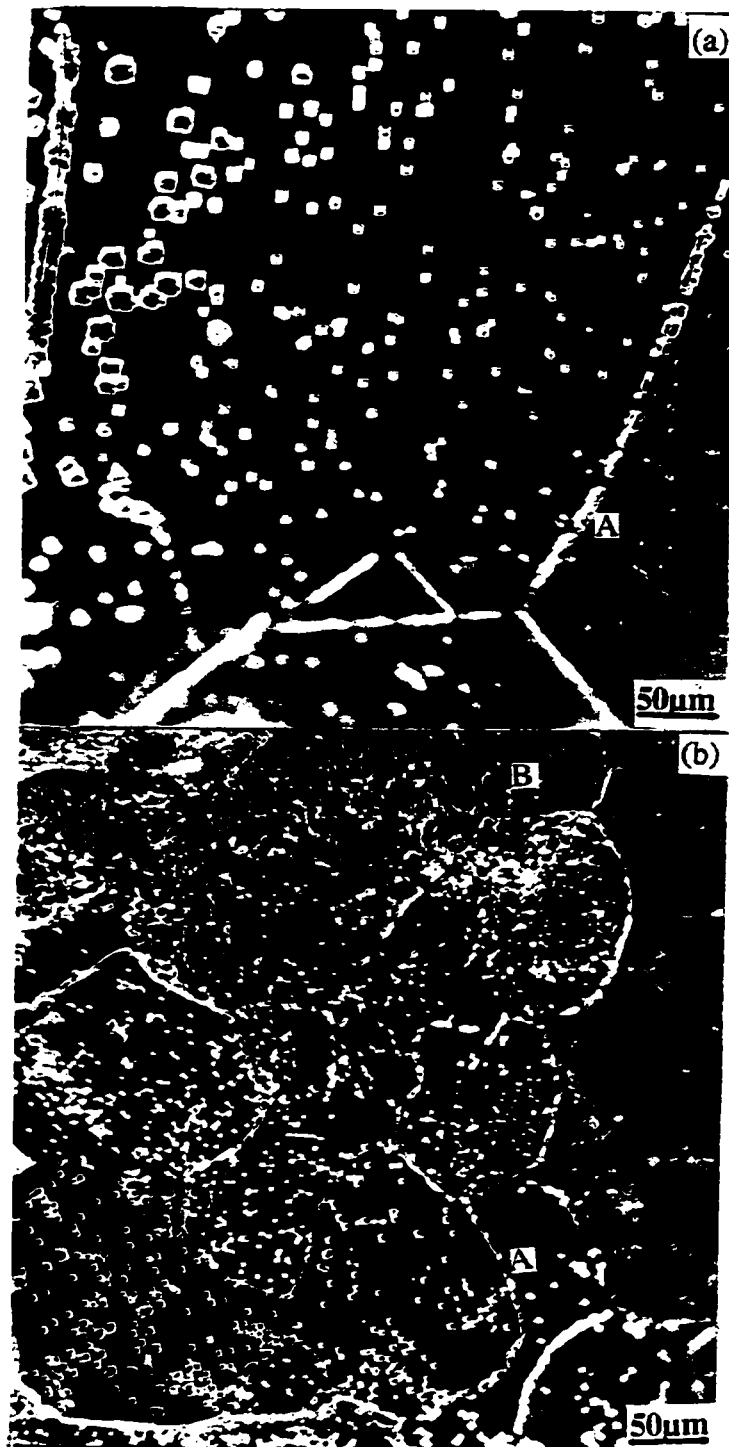


Fig.13 Optical micrographs of the as-quenched alloys, showing dislocations etch pits and a tilt boundary at A and dislocation clusters at B: (a) base alloy; (b)0.4%Be alloy.

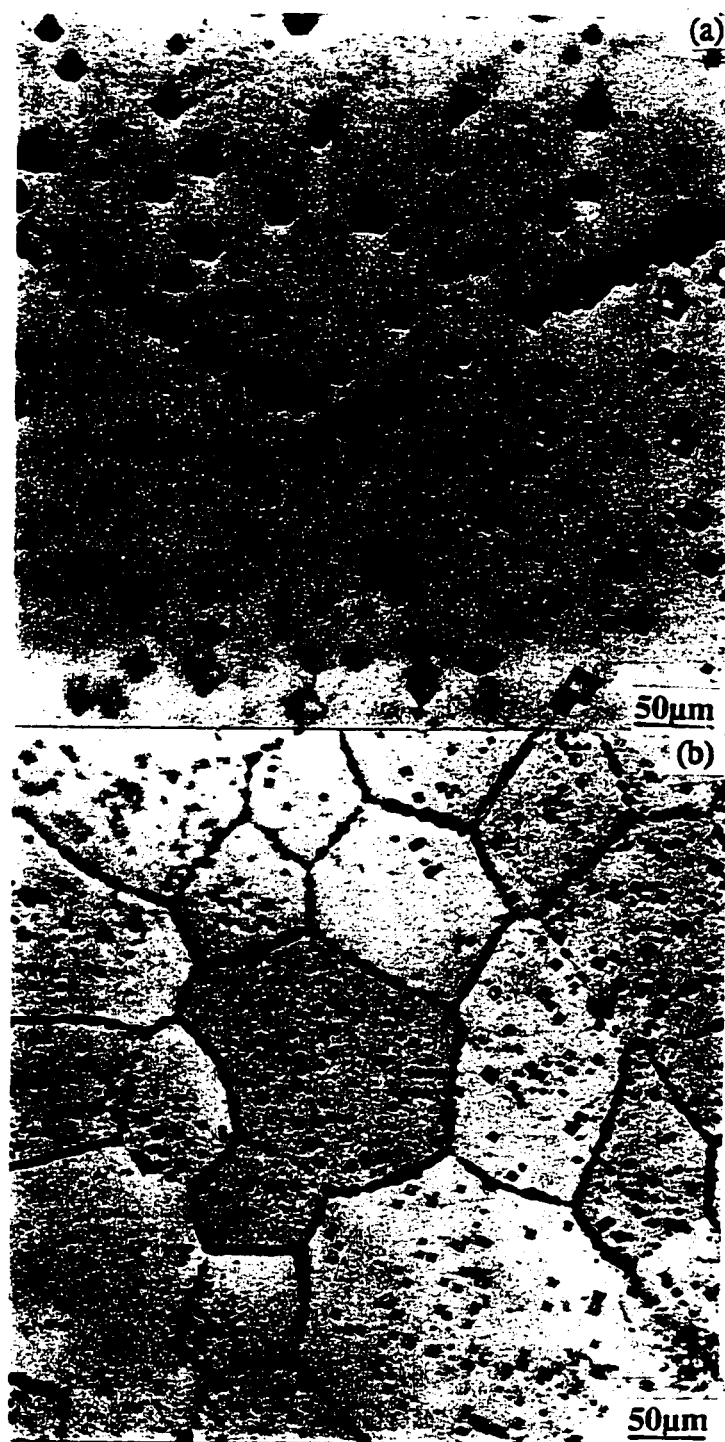


Fig.14 Optical micrographs for alloys aged at room temperature for 12 months, showing dislocations etch pits: (a) base alloy; (b) 0.4%Be alloy.

The average density of dislocations in Fig.13(a) is $\sim 2.8 \times 10^5 / \text{cm}^2$ for the as-quenched base alloy and >4 -fold higher ($>1.1 \times 10^6 / \text{cm}^2$) for the as-quenched Be-containing alloy, shown in Fig.13(b) (dislocations in clusters are not included due to difficulty in resolution). The alloys aged at room temperature for 12 months show a decrease in the average dislocation density for the both base alloy ($\sim 6.7 \times 10^4 / \text{cm}^2$, Fig.14(a)) and the 0.4%Be alloy ($\sim 2.4 \times 10^5 / \text{cm}^2$, Fig.14(b)); however the density for the Be-containing alloy still remains about ~ 4 -fold higher than for the base alloy.

Figs.15 and 16 show the dislocation etch pits for the alloys aged at 250°C for 20 and 65min respectively. The calculated average dislocation density (Fig.15) for the base alloy aged for 20min. is $\sim 8.0 \times 10^4 / \text{cm}^2$ vs. $\sim 2.5 \times 10^5 / \text{cm}^2$ for the Be-containing alloy, and as the aging time increases to peak hardness (65min.), the average dislocation density (Fig.16) decreases to $\sim 7.0 \times 10^4 / \text{cm}^2$ for base alloy and $\sim 1.6 \times 10^5 / \text{cm}^2$ for the Be-containing alloy, i.e. the Be-containing alloy still shows a ~ 2 -3 fold higher dislocation density than the base alloy. Based on quenching and annealing experiments on pure copper, Livingston[89] reports a dislocation density of $\sim 2 \times 10^6 / \text{cm}^2$ for the as-quenched vs. $\sim 3 \times 10^5 / \text{cm}^2$ for the as-annealed alloy, which is qualitatively consistent with the present investigation. The higher dislocation density for the Be-containing alloy would provide additional sites for nucleation of the precipitating phase (Mg_2Si).

4.2 Aging Behaviour

4.2.1 Precipitation Stages

The age hardening and resistivity curves for the alloys aged at room temperature, 150, 200, 250 and 300°C are shown in Figs.17 through 21 respectively. The room temperature

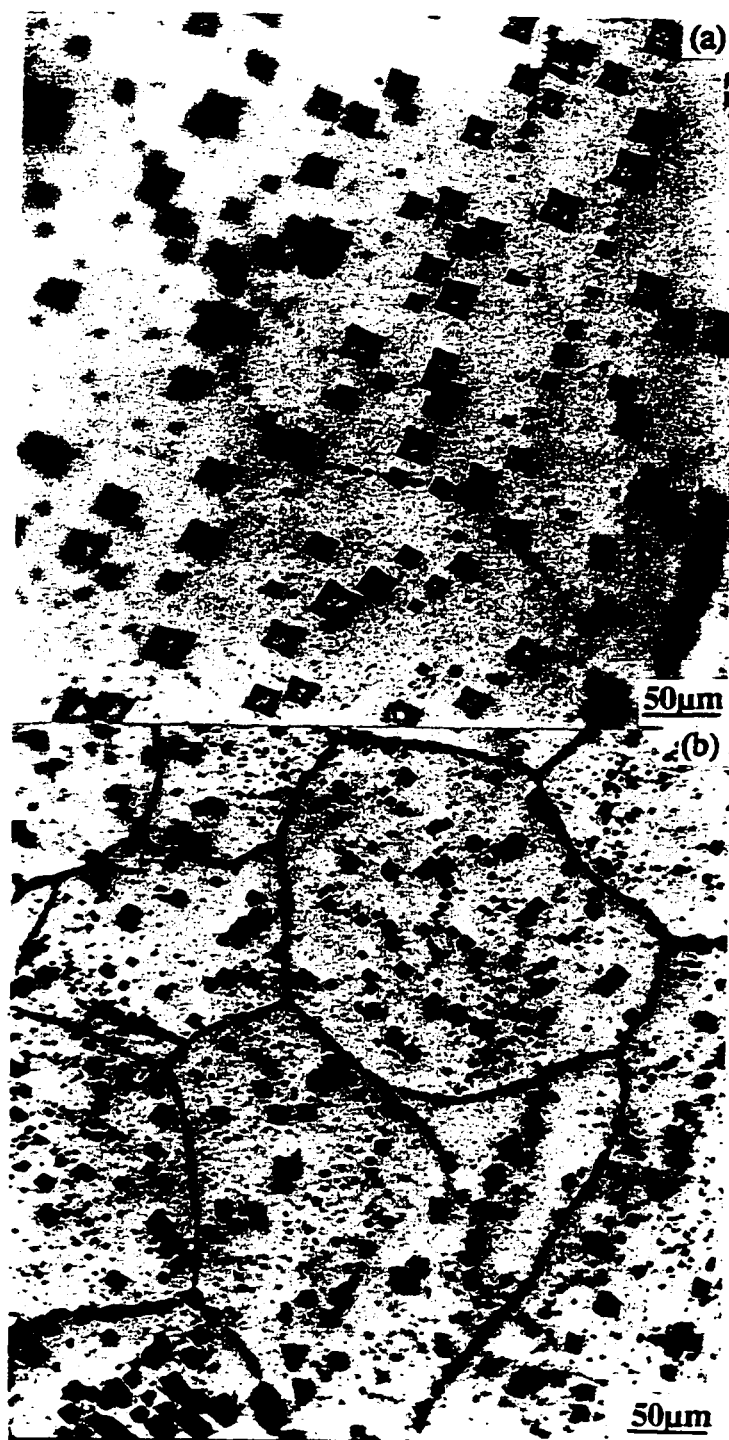


Fig.15 Optical micrographs for alloys aged at 250°C for 20 min., showing dislocations etch pits: (a) base alloy, (b) 0.4%Be alloy.

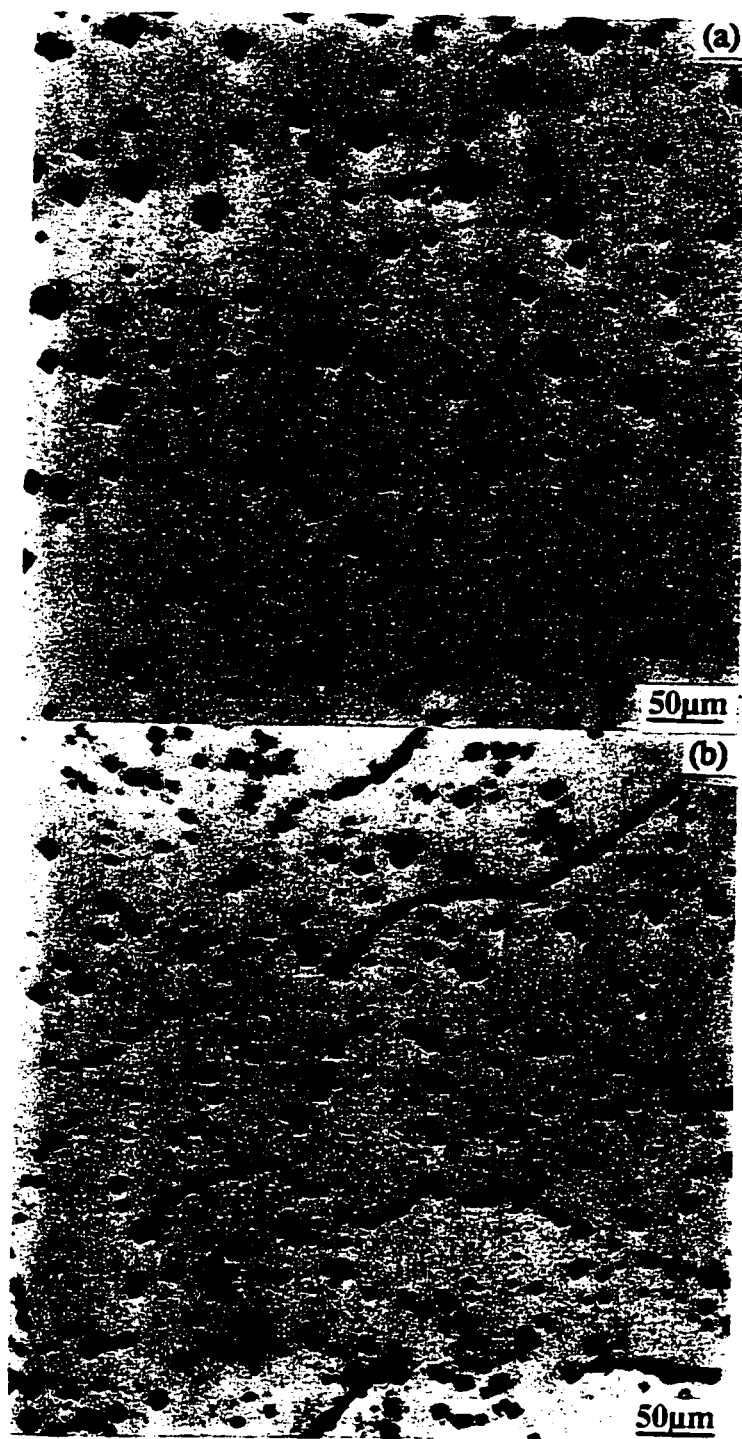


Fig. 16 Optical micrographs for alloys aged at 250°C for 65 min.(peak hardness), showing dislocations etch pits: (a) base alloy; (b) 0.4%Be alloy.

results indicate that the formation of vacancy-solute clusters is the initial stage of decomposition for both alloys, occurring over a time span of approximately 100 hours. This is more readily evident from the incremental change in resistivity ($\Delta\rho=\rho_{t=\infty}-\rho_{t=0}$) shown in Fig.17 (c). The formation of solute clusters or GP zones is a low temperature diffusion process, and is dependent on the presence of excess vacancies quenched in from the higher solution temperature. The vacancies diffuse to the sinks (dislocations, grain boundaries), and correspondingly the solute atoms diffuse to form solute clusters or GP zones. Clustering in Al-Mg₂Si alloys is reported to occur in the temperature range 70-80°C, which is above that for GP zone formation[92,93]. The age hardening curve (Fig.17(a)) for the Be-containing alloy shows a marked increase in the age hardening rate (after 100 hrs.) compared with the base alloy, indicating that Be increases the solute cluster density, which suggests a higher trapping of excess vacancies by Be during solution treatment, which is consistent with the reported high Be-vacancy binding energy (0.26 eV[93]). Karov[94] showed a similar effect for Al-Cu alloy when small additions of Be were made. The higher initial (as-quenched) hardness and resistivity for the Be-containing alloys may be attributed to the solid solution hardening effect of Be.

Figs.18-21 give the hardness and resistivity curves for the alloys aged at 150, 200, 250, 300°C respectively. The age hardening and resistivity curves show several stages, the number depending on the aging temperature. Two stages are readily distinguished for both the base and the Be-containing alloys for the 150°C aging treatment (indicated in Fig. 18), showing that either method can be used to describe the precipitation process. Stage (1) is characterized by the initial relatively slow increase in hardness (Fig.18(a)) or slow decrease

in resistivity (Fig.18(c)), corresponding to the formation of solute clusters. GP zone formation (stage (2)) is identified by the faster rise in the hardness or drop in resistivity. It is evident that the addition of 0.4%Be has increased the hardness of the two stages significantly, e.g., the Be-containing alloy attains a peak hardness of ~HV 125 in ~540min., vs. ~HV 113 in ~1080min. for the base alloy. Three stages are evident in the curves for the alloys aged at 200 and 250°C (Figs.19,20), and decrease to two stages at 300°C (Fig.21). The stages are generally associated with solute cluster formation (stage (1)), followed by their transformation to coherent GP zones (stage (2)) at low aging temperatures. At higher aging temperatures, the increased overall transformation rate results in an overlap of GP zone formation (stage(2)) and precipitation of semicoherent β' precipitate (stage(3)), and the age-hardening curves show a continuous rise to peak hardness levels. Again, the effect of Be is to accelerate the transformation process, and increase the peak hardness level, e.g., for the 250°C age, the peak hardness reaches ~HV 113 in ~30 min. for the Be-containing vs. ~HV 100 in ~65 min. for the base alloy. Stage (4) is the formation of the equilibrium β phase, which results in a monotonically decreasing hardness and resistivity of the alloys to constant levels, indicating completion of the transformation. In general, the peak hardness values decrease with increasing aging temperature due to particle coarsening.

4.2.2 Kinetic Treatment of Rate Data

The fraction (Y) of solute forming GP zones and β' , as determined using hardness measurements, is given by

$$Y = ((H_{t=t} - H_{t=0}) / (H_{peak} - H_{t=0})) \quad (40)$$

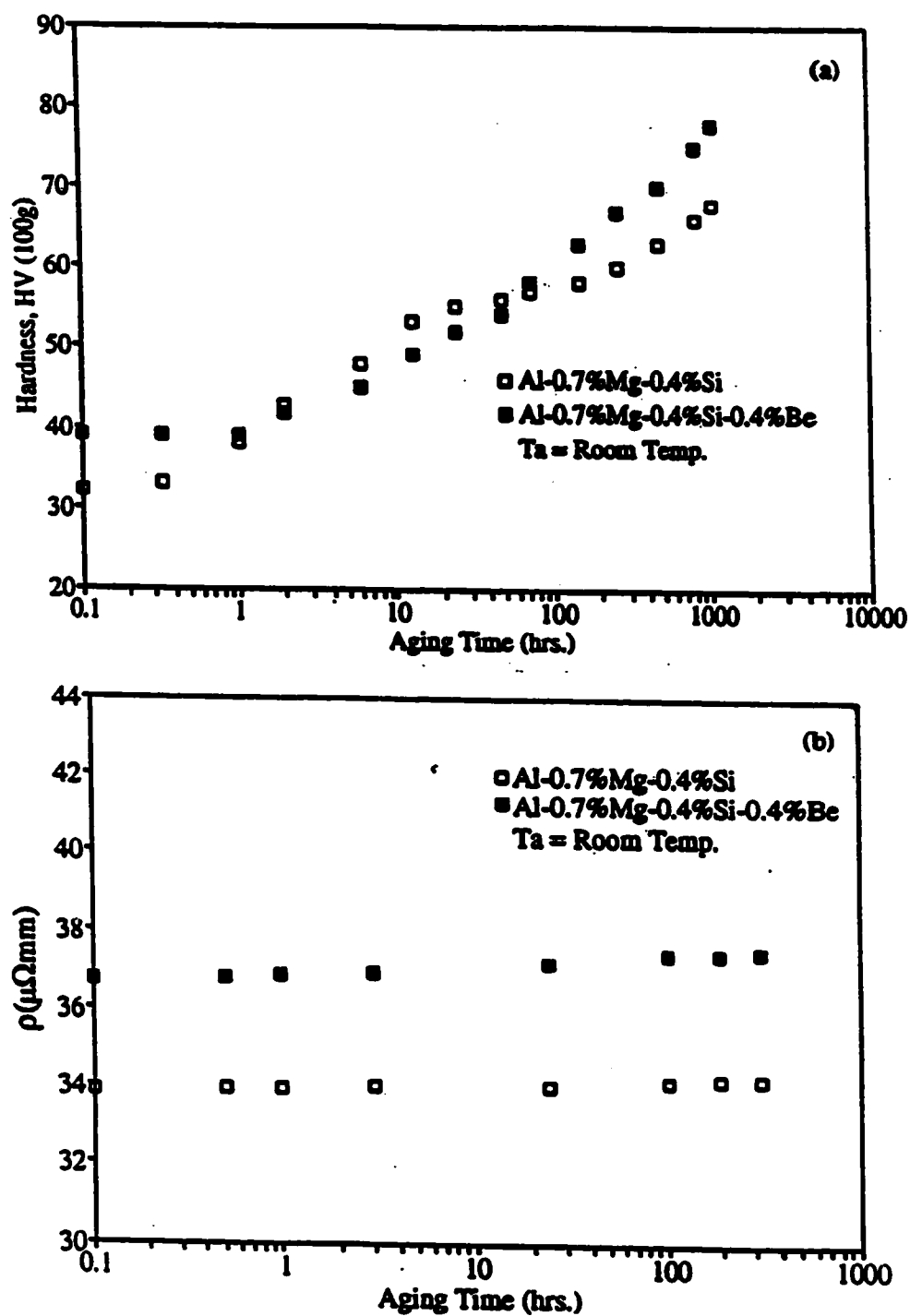


Fig.17 (a) HV vs. log t and (b) ρ vs. log t plots for the alloys aged at room temperature.

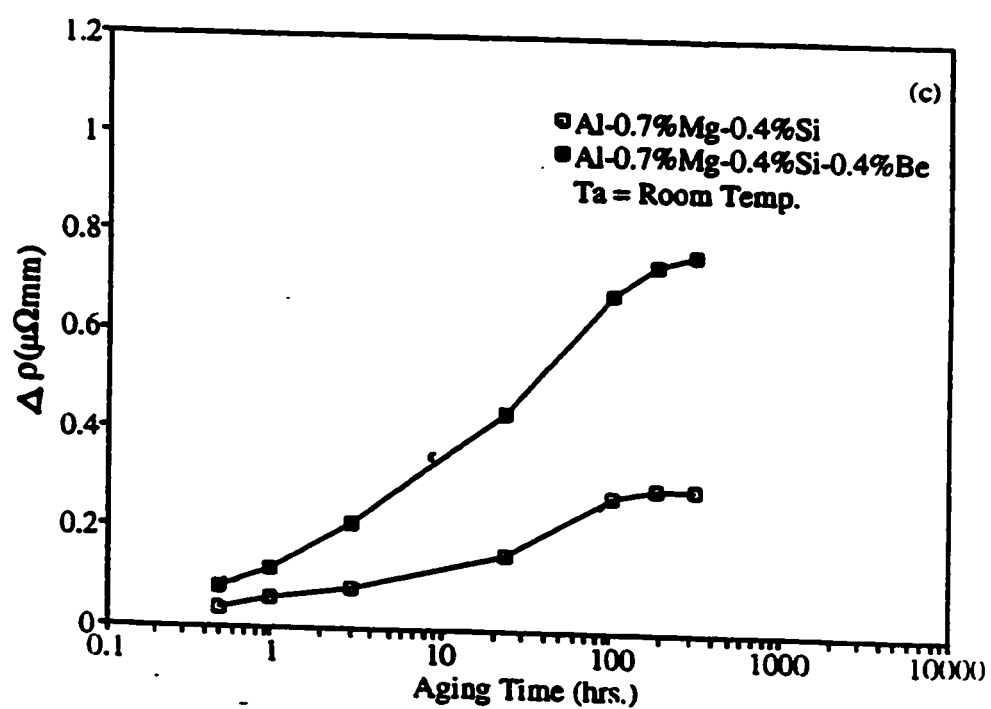


Fig.17 (c) $\Delta\rho$ vs. $\log t$ plot for alloys aged at room temperature.

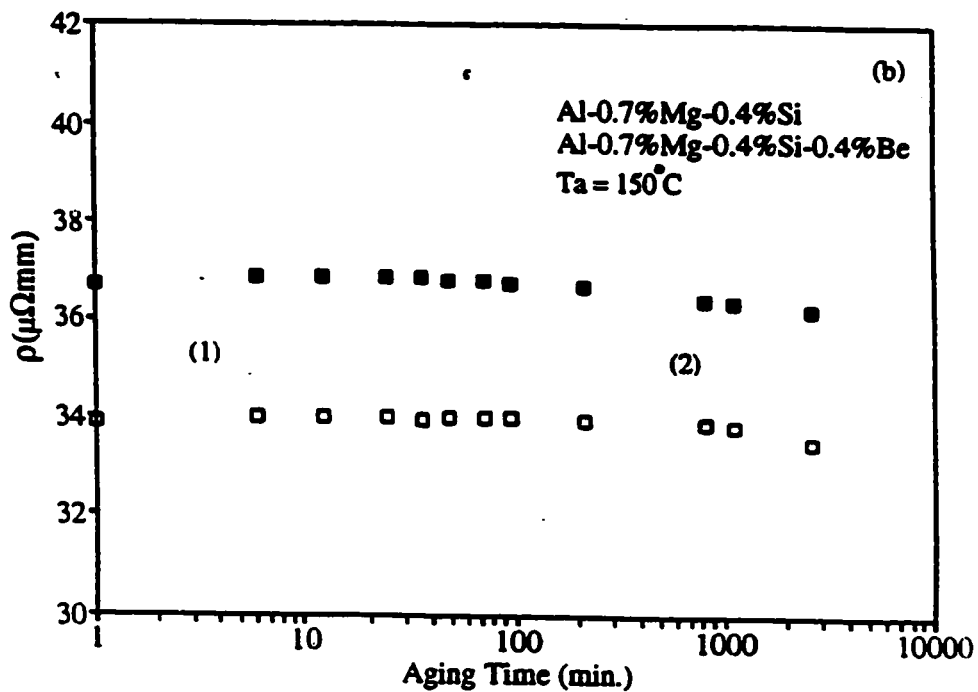
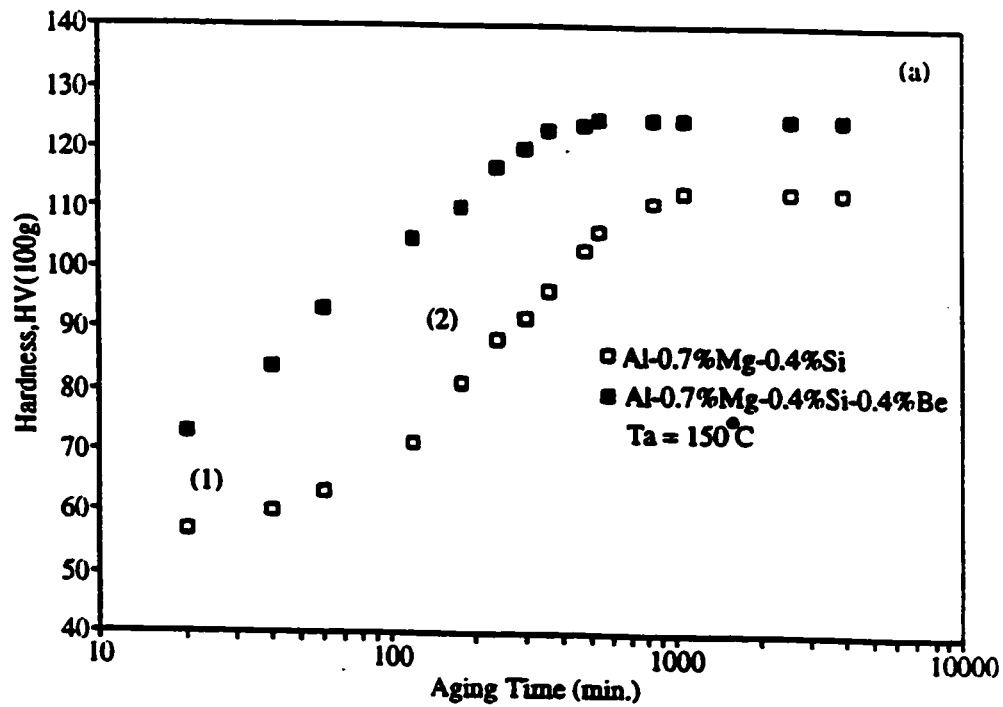


Fig. 18 (a) HV vs. log t and (b) ρ vs. log t plots for the alloys aged at 150°C.

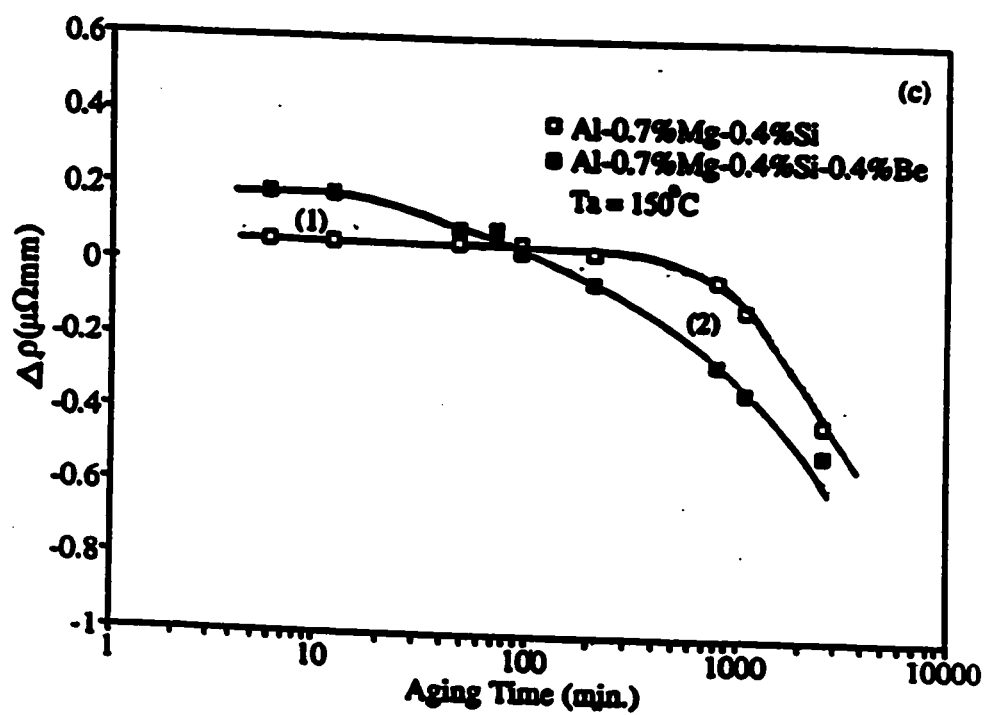


Fig.18 (c) $\Delta\rho$ vs. $\log t$ plot for alloys aged at 150°C .

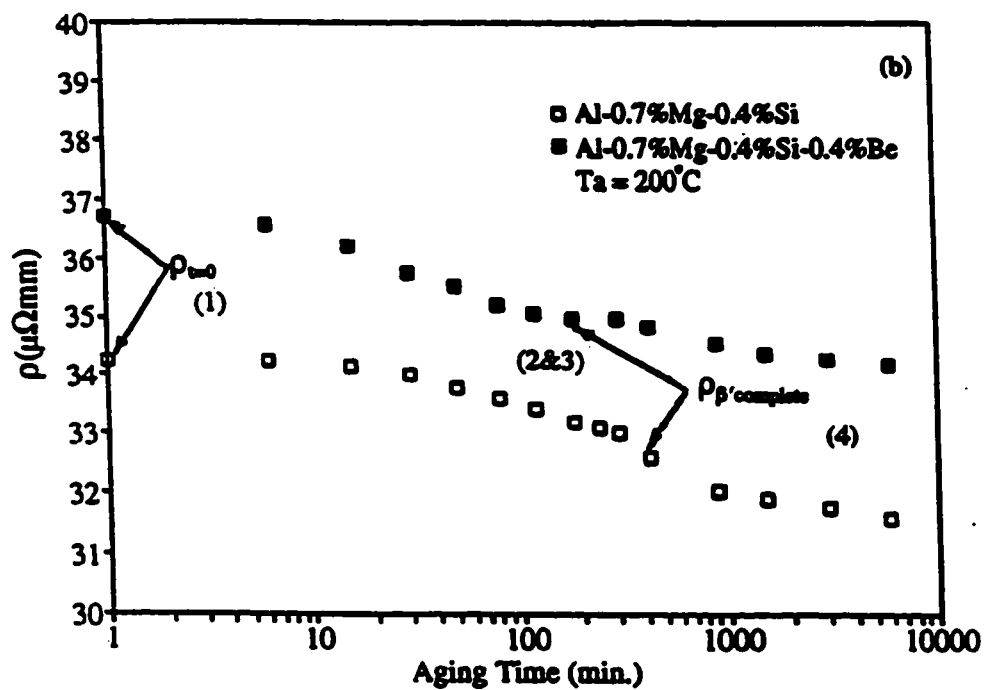
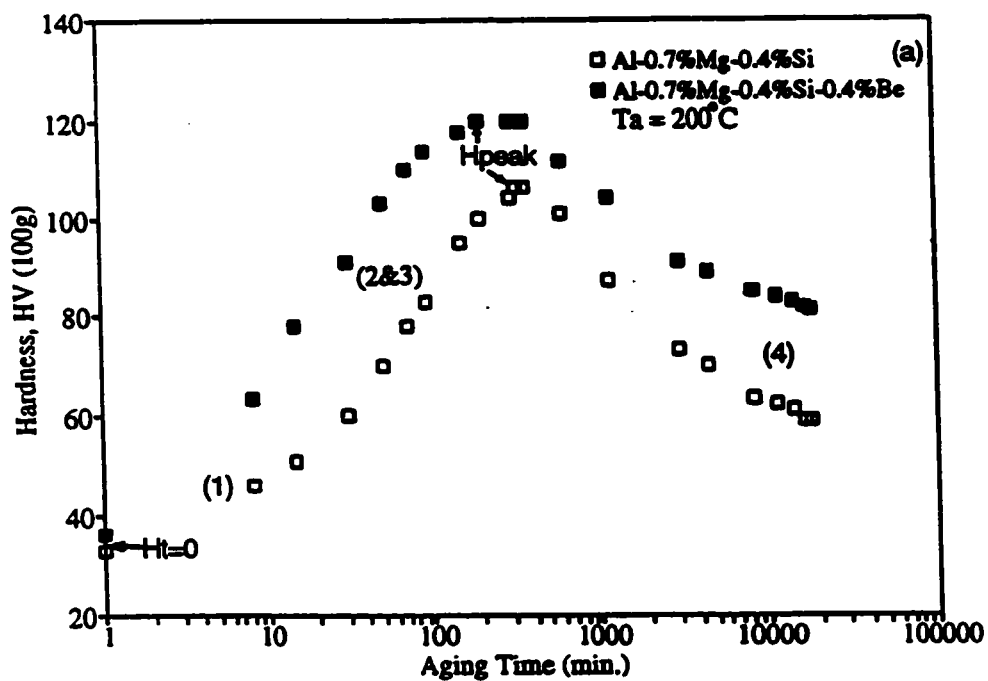


Fig. 19 (a) HV vs. log t and (b) ρ vs. log t plots for the alloys aged at 200°C .

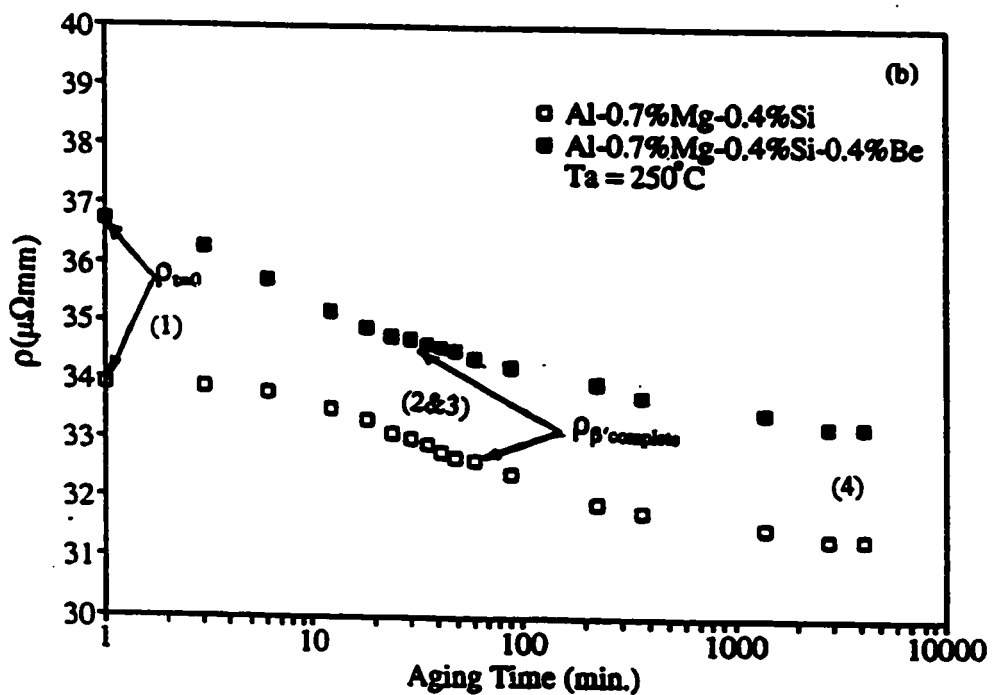
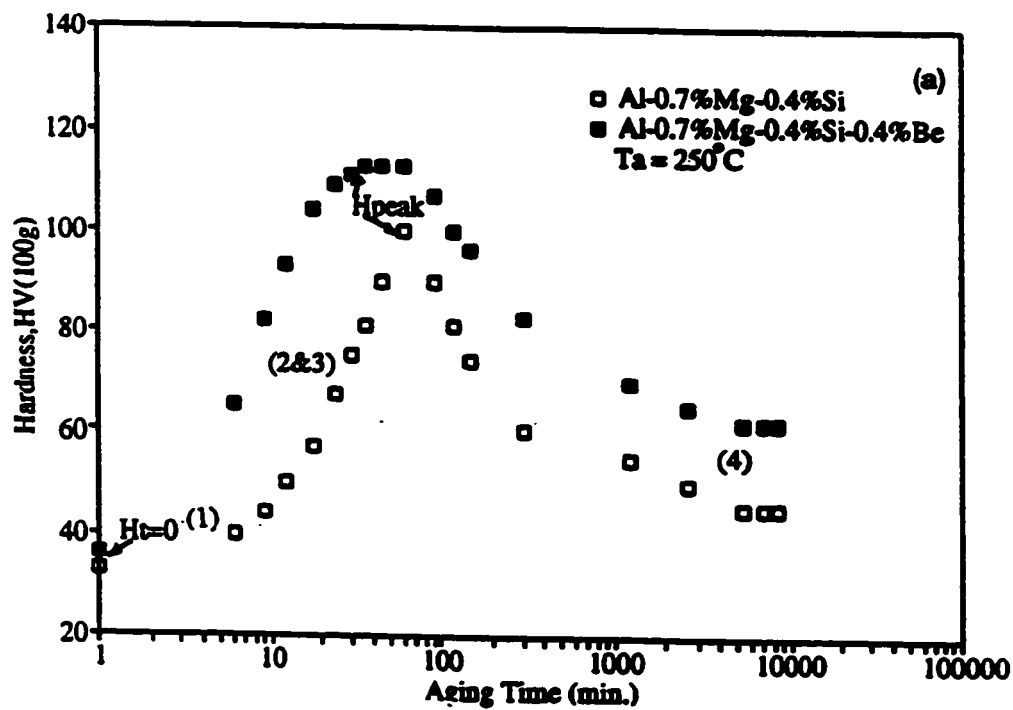


Fig.20 (a) HV vs. log t and (b) ρ vs. log t plots for the alloys aged at 250°C .

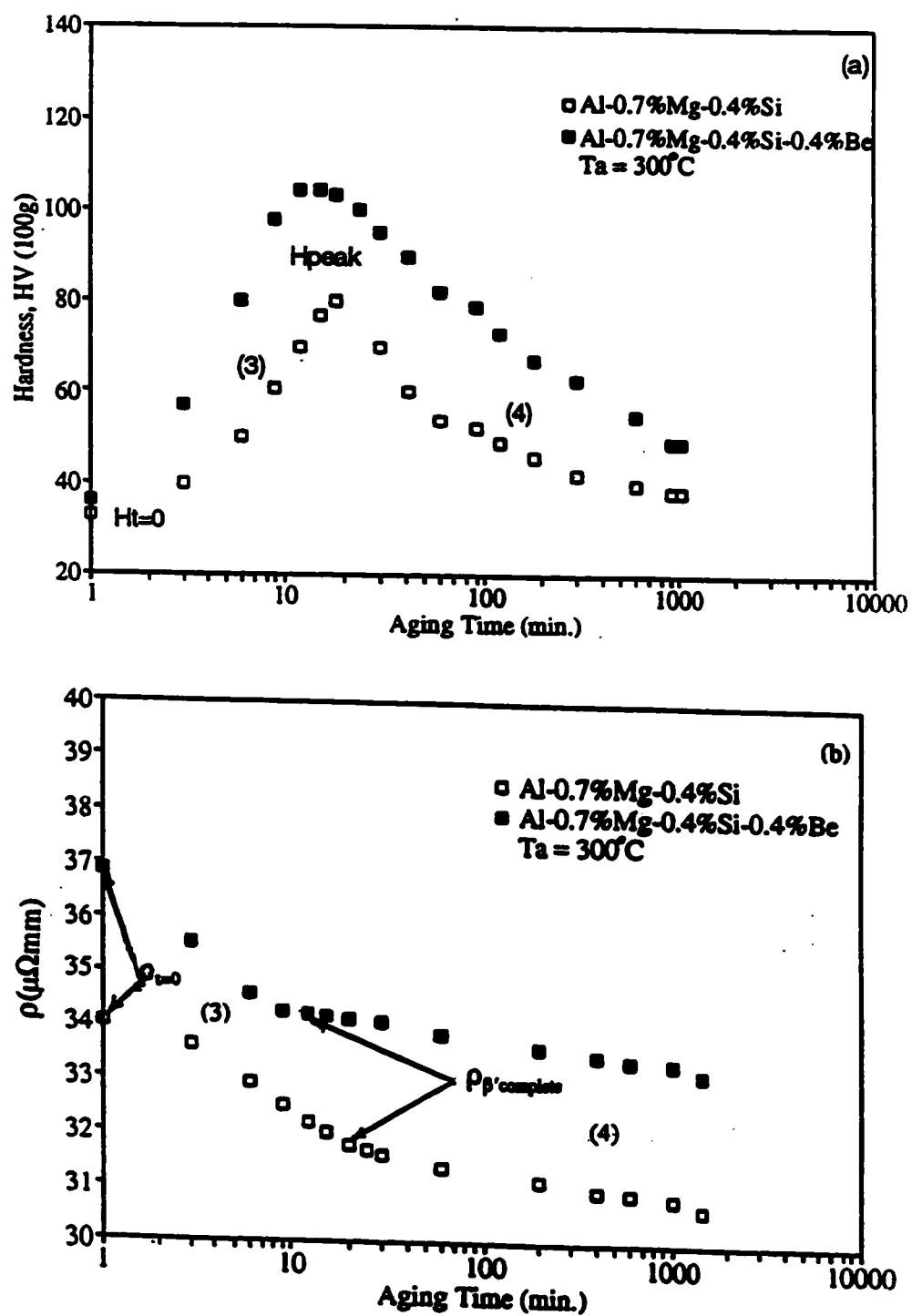


Fig.21 (a) HV vs. log t and (b) ρ vs. log t plots for the alloys aged at 300°C.

where $H_{t=t}$ is the hardness at aging time t , $H_{t=0}$ the initial hardness at zero aging time (start of aging, here taken at 1 minute into the aging time for log plots), and H_{peak} the peak hardness value. The peak hardness value corresponds to completion of β' formation, and the age hardening results for the alloys aged at room temperature, 150, 200, 250, and 300°C are shown in Figs.17a, 18a, 19a, 20a, and 21a.

The resistivity results, Figs.17b, 18b, 19b, 20b, and 21b, do not clearly show the completion of the different stages. This is more accurately determined from the derivative (dp/dt) plots, as shown in Figs. 22, 23 and 24 for the alloys aged at 200, 250 and 300°C respectively, where the more clearly defined slope changes determine the time when β' transformation is complete (corresponding to the peak hardness times in Figs.19a, 20a, 21a). The Y-fraction transformed as interpreted from resistivity measurements is given by

$$Y = ((\rho_{t=0} - \rho_{t=t}) / (\rho_{t=0} - \rho_{\beta'complete})) \quad (41)$$

where $\rho_{t=t}$ is the resistivity at aging time t , $\rho_{t=0}$ the resistivity at zero aging time (start of aging, 1 minute), and $\rho_{\beta'complete}$ the resistivity at the completion of β' transformation (corresponding to peak hardness values). It is estimated that the error in establishing the time for the start and the completion of the transformation is $\sim \pm 15\%$.

Figs 25, 26 and 27 show Y vs. log t plots obtained using eqs.(40,41) for the alloys aged at 200, 250 and 300°C respectively. It is evident that the hardness and resistivity techniques give essentially equivalent results, and that the transformation for the Be-containing alloy is significantly faster compared to the Be-free base alloy.

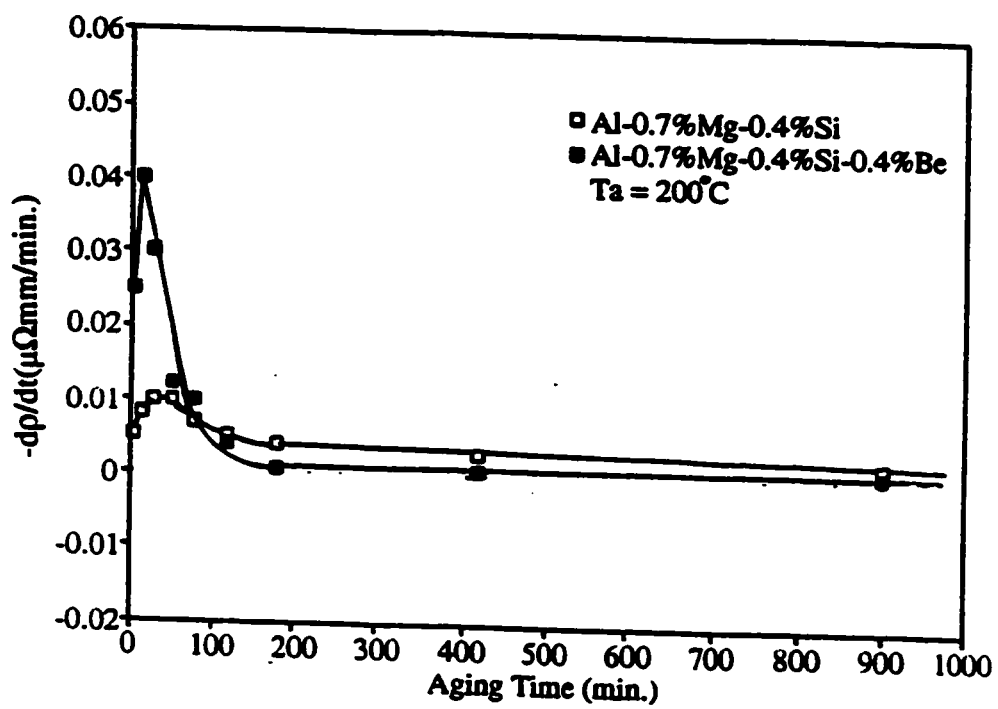


Fig.22 dp/dt vs. t for the alloys aged at 200°C .

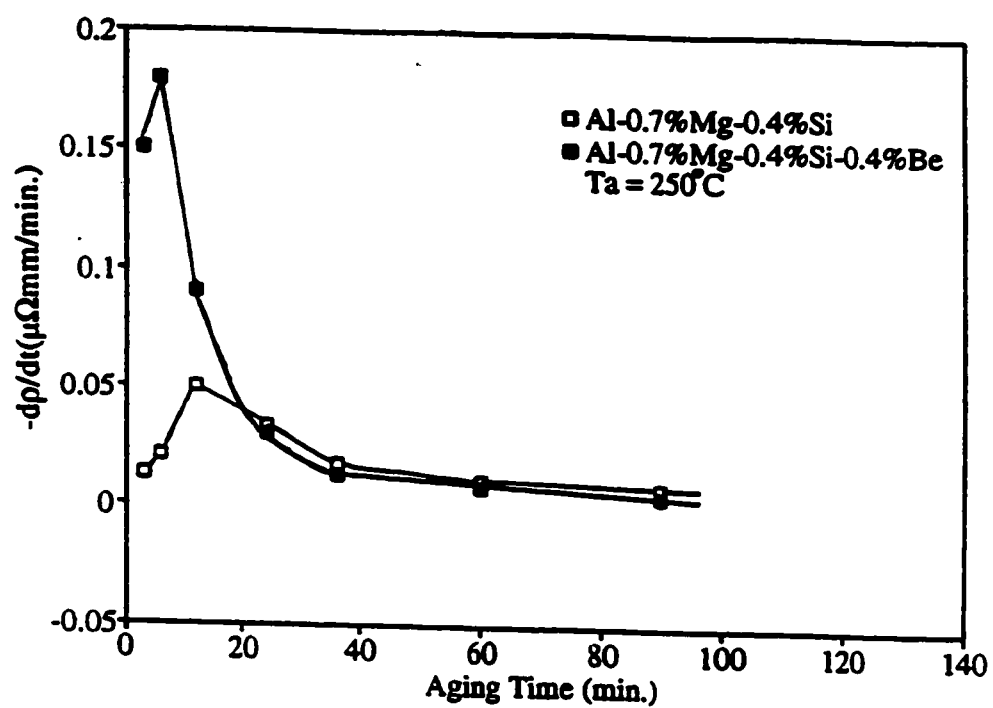


Fig.23 dp/dt vs. t for the alloys aged at 250°C.

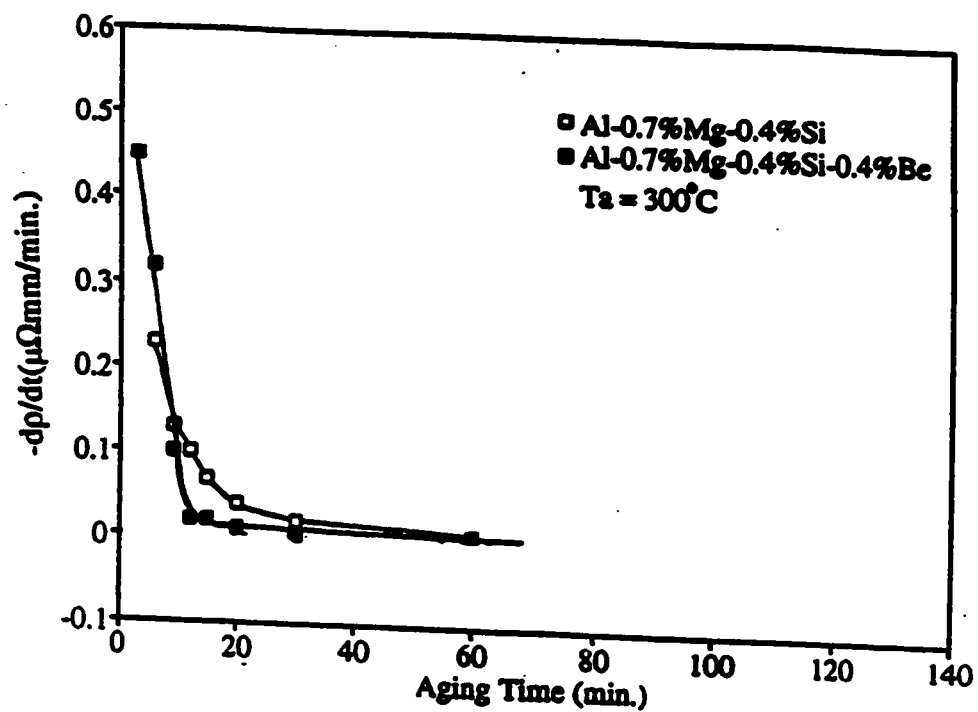


Fig.24 dp/dt vs. t for the alloys aged at 300°C .

The kinetic parameters (n) and (k_1) are obtained from the logarithmic plot of eq.(34), which is a straight line function (eq.(35)) with (n) the slope and k_1 obtained from the intercept ($= n \log k_1$). Plots of eq.(35) for the alloys aged at 200, 250 and 300°C are given in Figs. 28, 29 and 30 respectively. The results show that the growth parameter (n) is essentially the same for both alloys, but that the nuclei density dependent parameter (k_1) is significantly higher for the Be-containing alloy. The Arrhenius plots to obtain the activation energies from k_1 (eq.36 or 37) are given in Fig.31(a) and (b), and Table2 summarizes the kinetic parameters obtained.

Table 2 shows good agreement between the results obtained using hardness and resistivity methods, and which can be considered equivalent within the estimated experimental error. The Be addition does not affect the precipitate growth mechanism (n and Q_1 are independent of composition); however, the nuclei density-dependent parameter k_1 is 2-3 times higher for the Be-containing alloy, which is consistent with the 2-3 fold higher density of the precipitate particles for the Be-containing alloy (see Fig. 34). In order to have optically resolvable precipitate particles, it was necessary to overage the alloys, hence the aging time of 17 hours at 300°C. It may be assumed Ostwald ripening has decreased the actual number of particles initially nucleated; however, this would be the case for both alloys and should not significantly affect the comparison of precipitate particle densities for the alloys.

The interpretation of the precipitate model and growth mechanism from the (n) values obtained presents some difficulty. Wert and Zener[59,55,95], by assuming growth conditions at advancing edges to be constant, obtained for small spheres, rods, and discs the (n) values 3/2, 4/2, 5/2 respectively. However, Ham[96] has shown that the growth conditions at edges for discs and rods will not remain constant as the excess solute is depleted, so that the particle

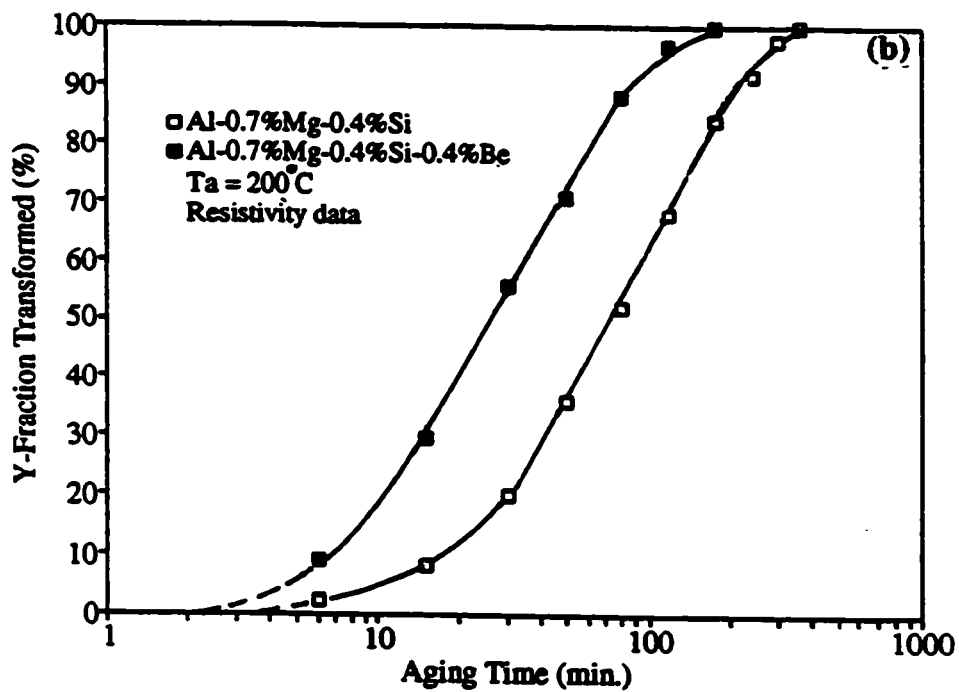
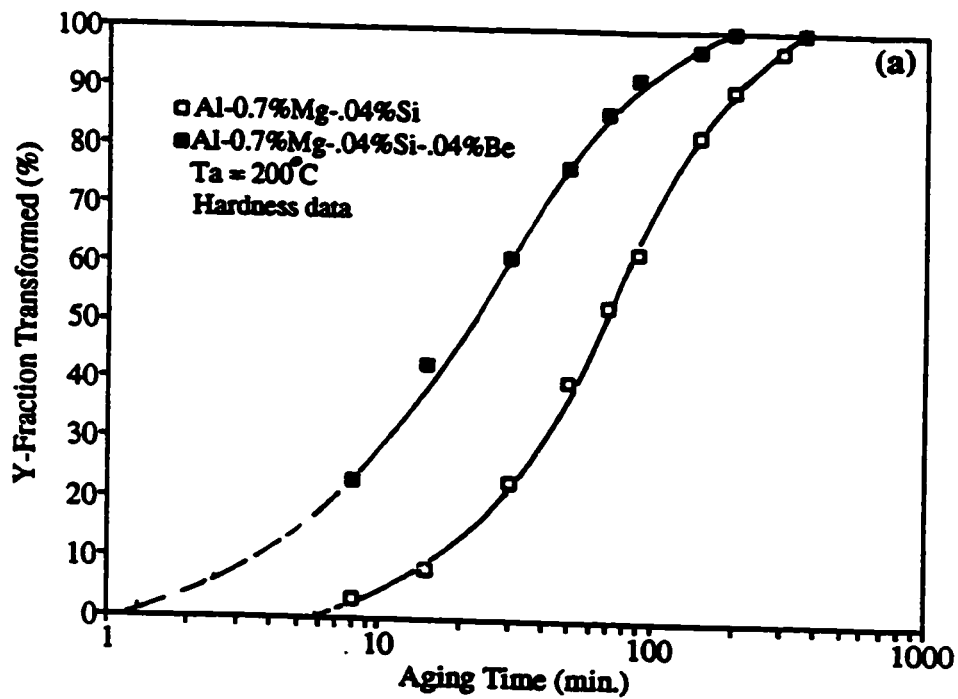


Fig.25 Y vs.log t for the alloys aged at 200°C : (a) hardness data and (b) resistivity data.

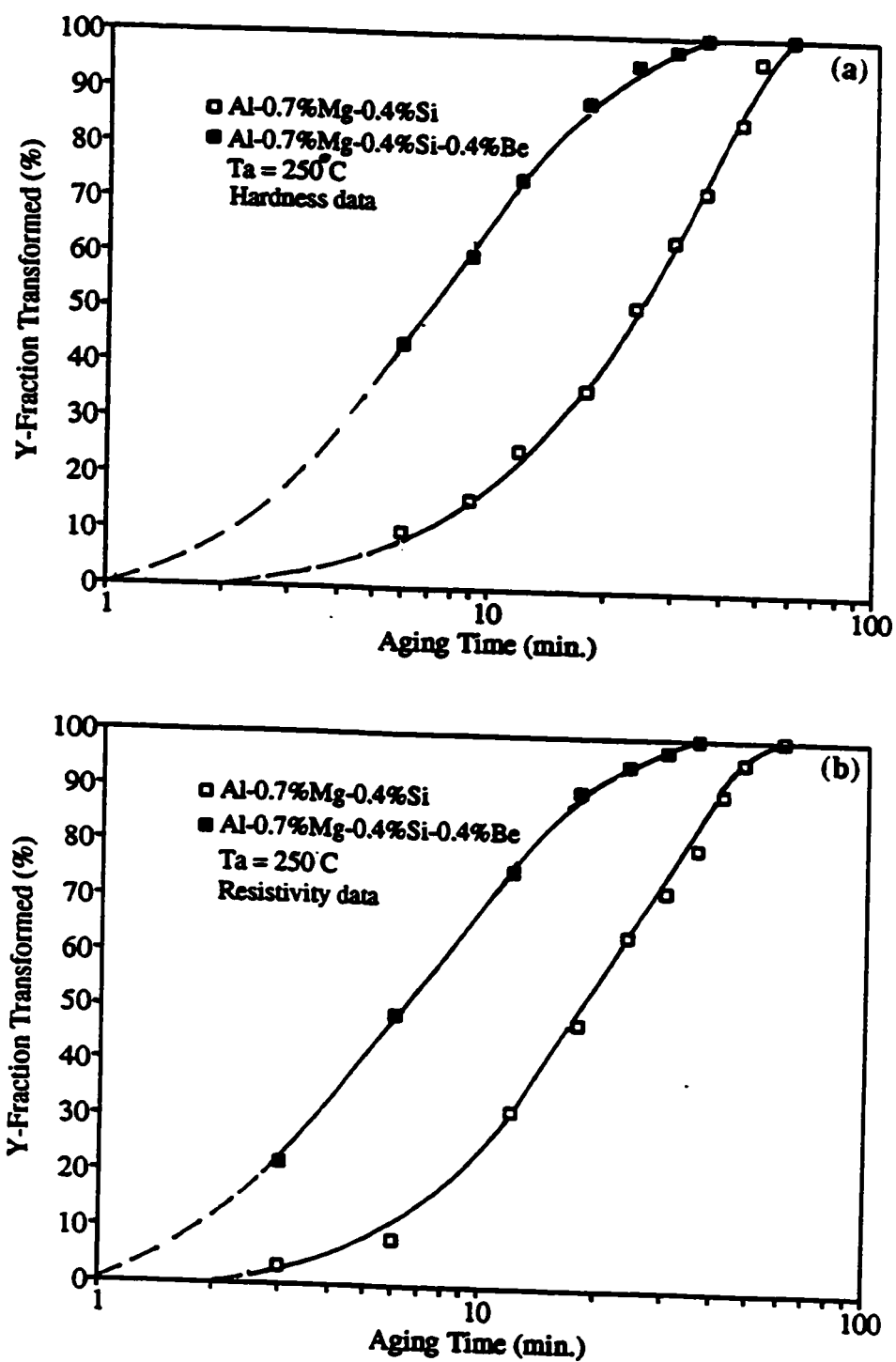


Fig.26 Y vs.log t for the alloys aged at 250°C: (a) hardness data and (b) resistivity data.

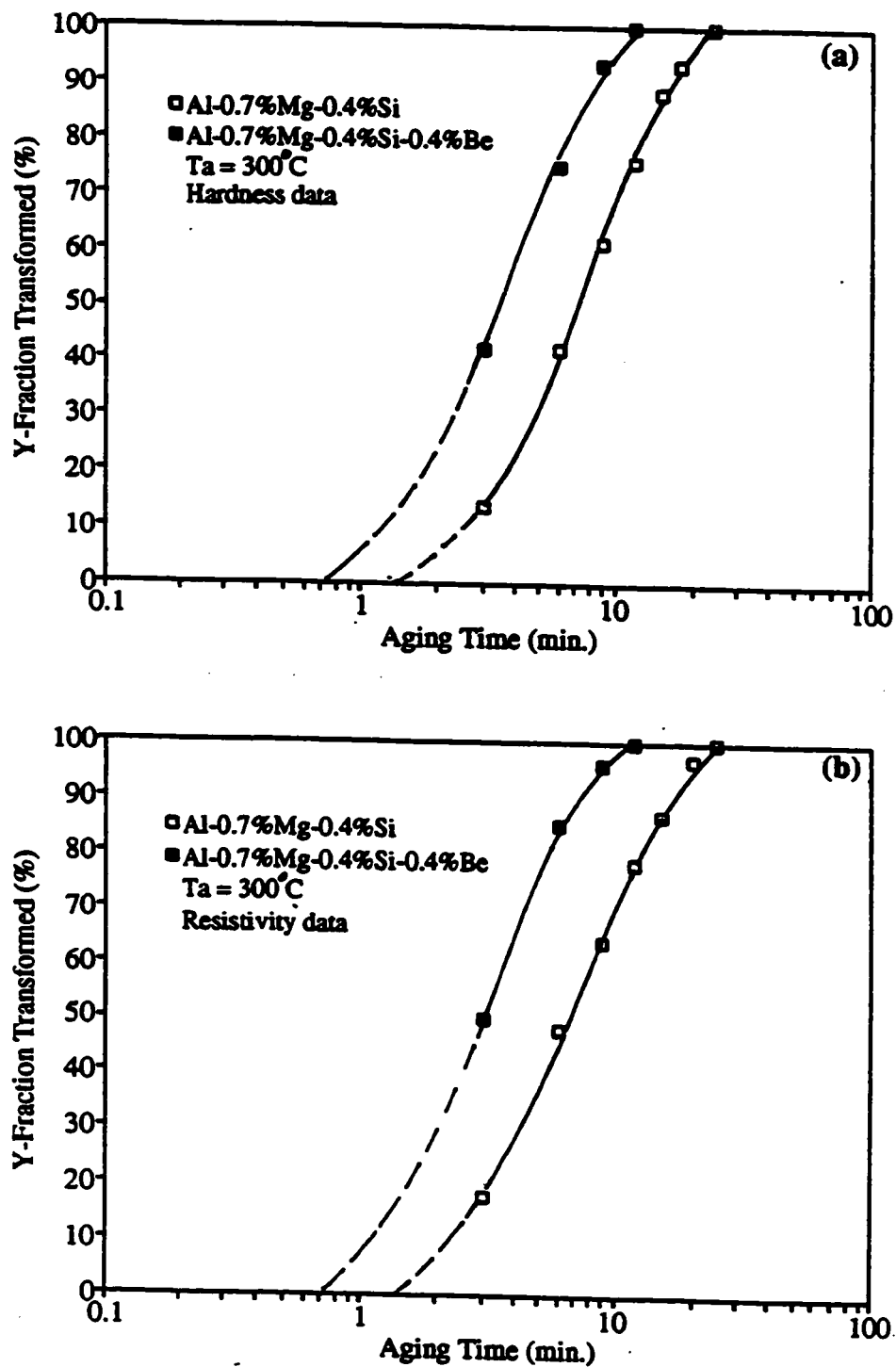


Fig.27 Y vs.log t for the alloys aged at 300°C: (a) hardness data and (b) resistivity data.

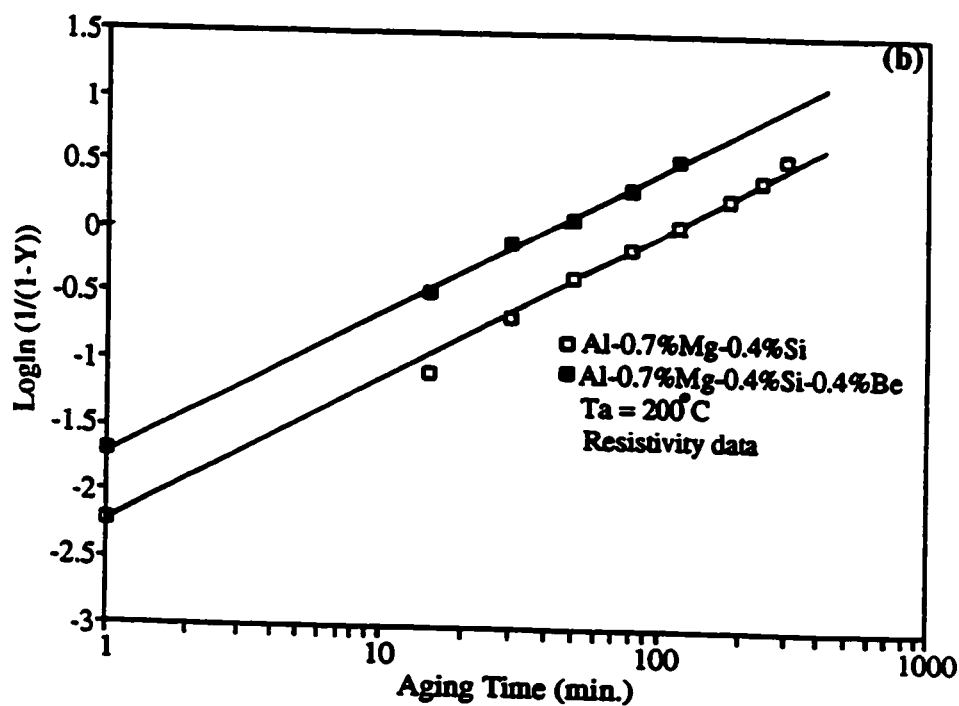
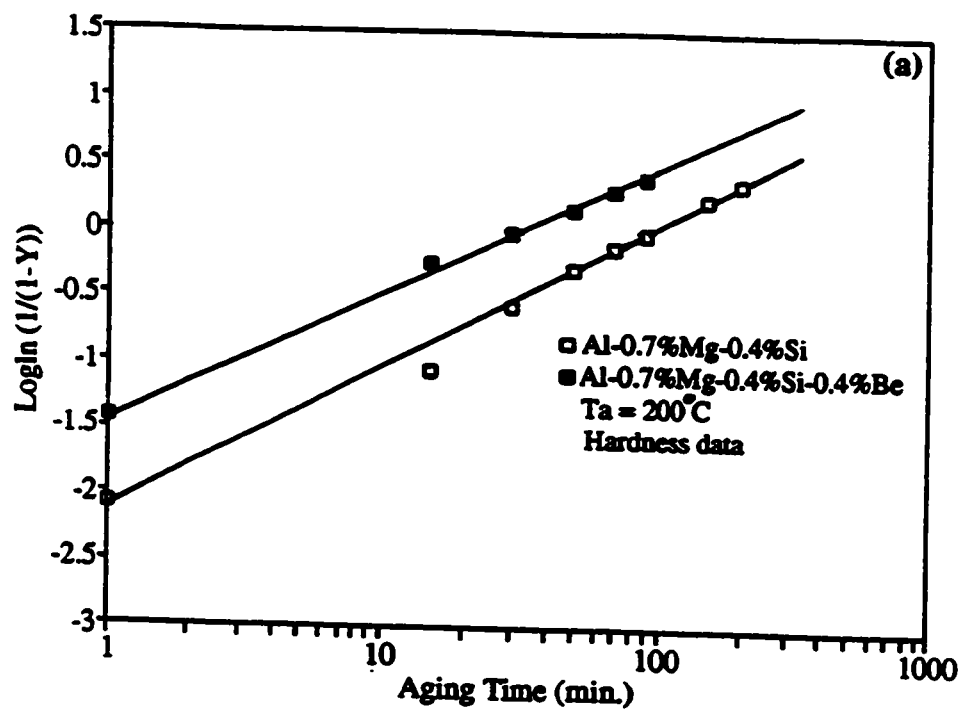


Fig.28 $\text{log ln } (1/(1-Y))$ vs. $\text{log } t$ for the alloys aged at 200°C: (a) hardness data and (b) resistivity data.

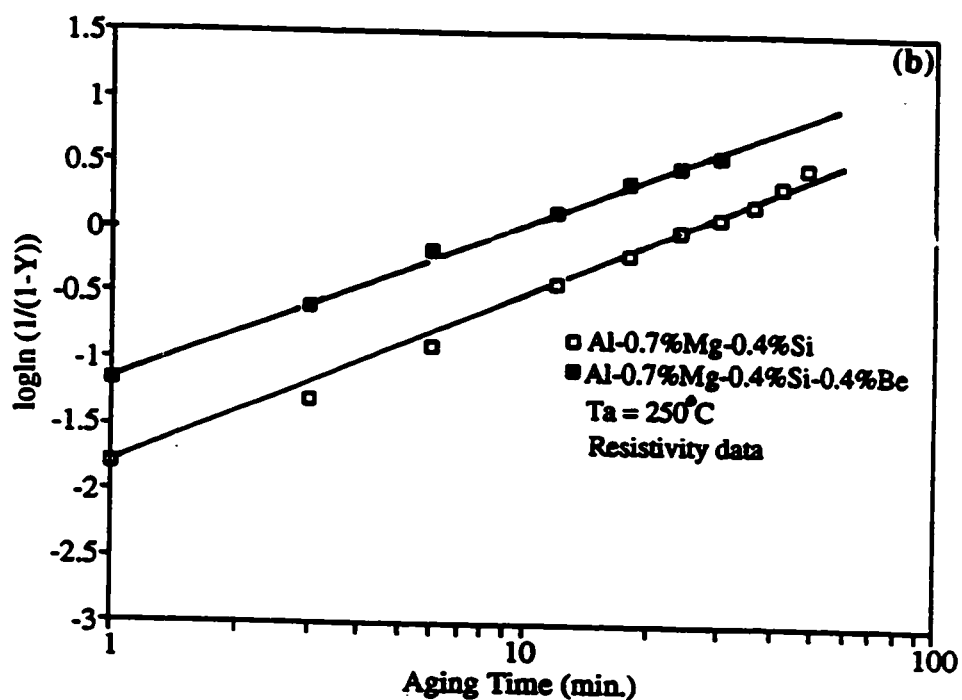
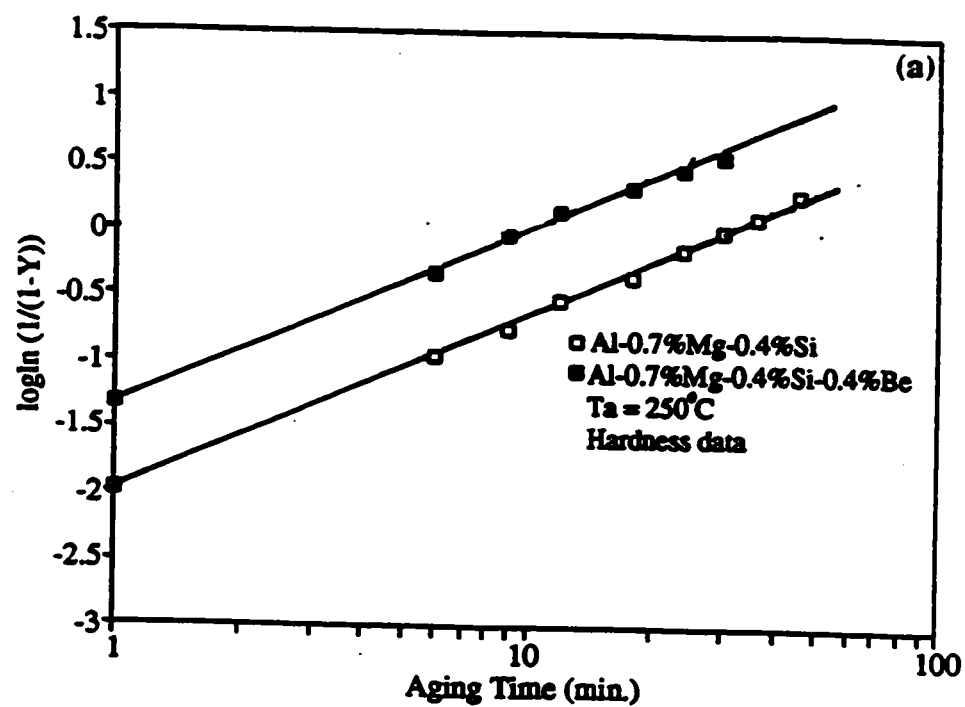


Fig.29 $\log \ln (1/(1-Y))$ vs. $\log t$ for the alloys aged at 250°C: (a) hardness data and (b) resistivity data.

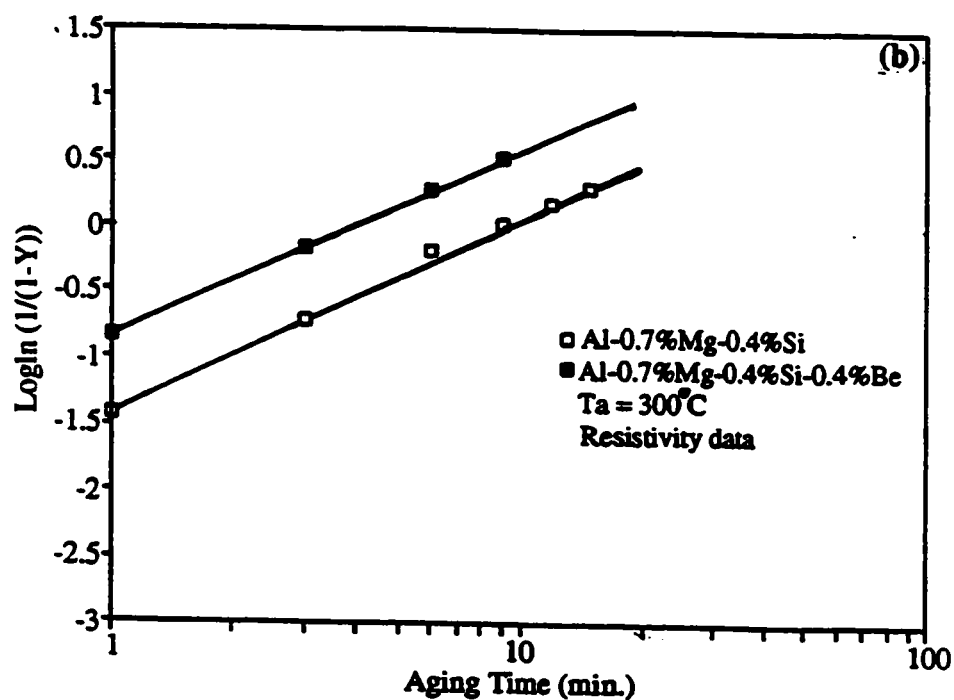
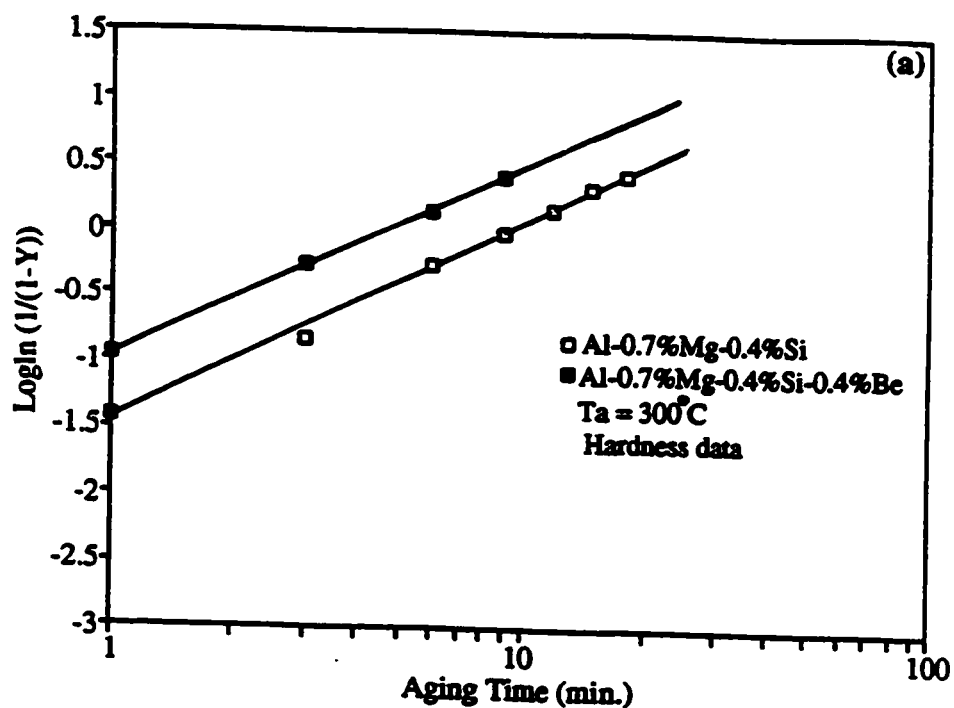


Fig.30 $\log \ln (1/(1-Y))$ vs. $\log t$ for the alloys aged at 300°C: (a) hardness data and (b) resistivity data.

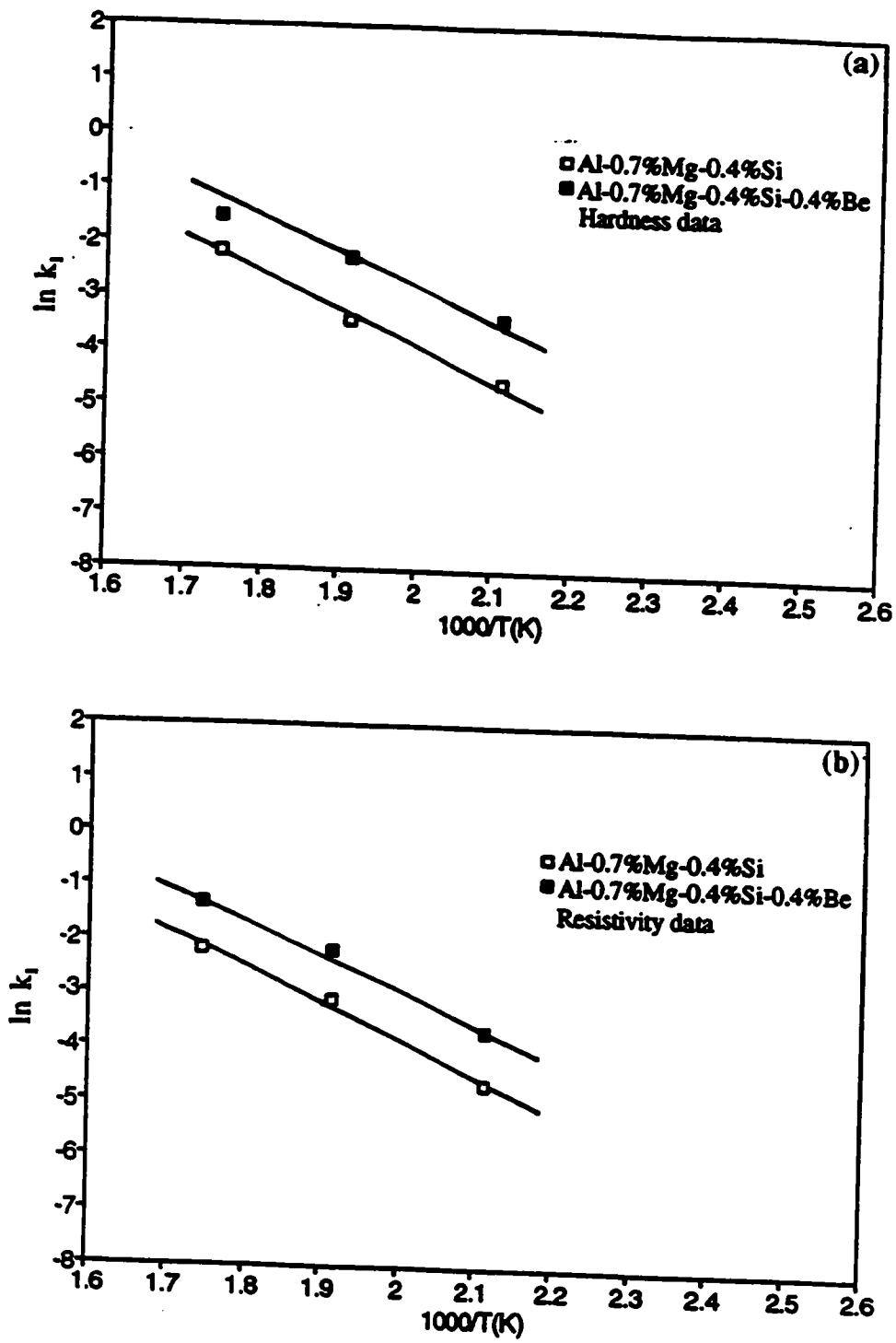


Fig.31 Arrhenius plots using k_1 : (a) hardness data and (b) resistivity data.

Table 2 Kinetic Parameters

Parameter	Temp., °C	Hardness Data		Resistivity Data	
		Base Alloy	Base Alloy with 0.4%Be	Base Alloy	Base Alloy with 0.4%Be
n k ₁	200	1.06±0.10 0.011±0.004	0.95±0.09 0.033±0.010	1.10±0.10 0.0096±0.004	1.07±0.07 0.026±0.006
n k ₁	250	1.33±0.07 0.032±0.006	1.31±0.07 0.099±0.012	1.28±0.05 0.04±0.005	1.23±0.05 0.11±0.010
n k ₁	300	1.47±0.08 0.11±0.013	1.42±0.06 0.21±0.014	1.48±0.06 0.11±0.010	1.43±0.04 0.26±0.010
Q ₁ (kJ) using k ₁		51.53±7.4	41.75±6.65	55.12±8.5	52.06±5.08

shape and growth constant n begin to change in the later stages of transformation. Ham obtains for discs of constant eccentricity (oblate spheroids) $n = 3/2$ (vs. $5/2$, Wert and Zener) during the initial stages of precipitation, which tends to $n = 1$ as the semimajor axis of the spheroid is altered during later stages of solute depletion. Stress-assisted precipitation on edge dislocations further complicates the process. Cottrell and Bilby[97] and Harper[98] have shown that where dislocation assisted precipitation is predominant, and with competition between dislocations occurring in the later stages, $n = 2/3$, and k_1 includes the length of the edge dislocations per unit volume.

GP zone formation, which is generally assumed to be needle-like, is formed during the initial stages of aging at the lower aging temperatures. At higher aging temperatures, β' -rod formation would predominate, dislocation-assisted precipitation would decrease, and 3-dimensional growth would increase, for which (n) approaches $3/2$. Doherty[99] proposed that for early stages of diffusion-controlled processes, the (n) value depends on the particle shape, which for long needles and large thin plates $n = 1$. The increase in a growth parameter from $n = 0.95$ - 1.10 (200°C) to $n = 1.42$ - 1.48 (300°C) for the present investigation is consistent with the above proposed growth mode.

Solution treated and quenched Al-alloys have high concentrations of trapped vacancies, and the vacancy diffusion mechanism becomes the predominant diffusion mode. Turnbull et al[100] showed that activation energies for the formation of solute clusters in Al-Cu, Al-Ag and Al-Zn alloys at lower temperatures are approximately 48, 58 and 38 kJ/mol. respectively. The activation energy for the migration of vacancies in pure Al is given as 48 kJ/mol.[101]. The present investigation gives an activation energy of 41 to 55 kJ/mol., which

is in the accepted range for vacancy diffusion in Al. In the previous study[11] the resistivity technique was used to study β phase formation, for which an activation energy of 61-70 kJ/mol. was obtained. The higher activation energy for β formation is consistent with the decrease in vacancy concentration for the later precipitation stages, requiring their formation (i.e., Frenkel defect), and thus correspondingly increasing the activation energy for solute diffusion.

4.2.3 Aged Microstructures

The addition of Be significantly retards grain growth during aging. Figs. 32 and 33 show the alloy microstructures after aging of the base and 0.4%Be alloys at 250°C for 140 hrs. The Be-containing alloys show grain size approximately 70% smaller (mean dia. 176 μm for Be-containing vs. 487 μm for base alloy), which can be attributed in part to the (excess) Be particles in grain boundaries inhibiting grain boundary migration. Both alloys show β precipitate free zones (PFZ) along the grain boundaries (Fig. 33). Note that the addition of Be has no significant affect on the width of the PFZ. Fig. 34(a) and (b) show the microstructures of the base and Be-containing alloys respectively, aged at 300°C for 17 hrs. The Be-containing alloy shows approximately a 3-fold higher density of the precipitate particles compared with the base alloy, and indicates a Be-enhanced nucleation rate. The increased precipitate particle density for the Be-containing alloys is consistent with the aging results, i.e., the higher peak hardness levels and faster transformation rates compared to the base alloys.

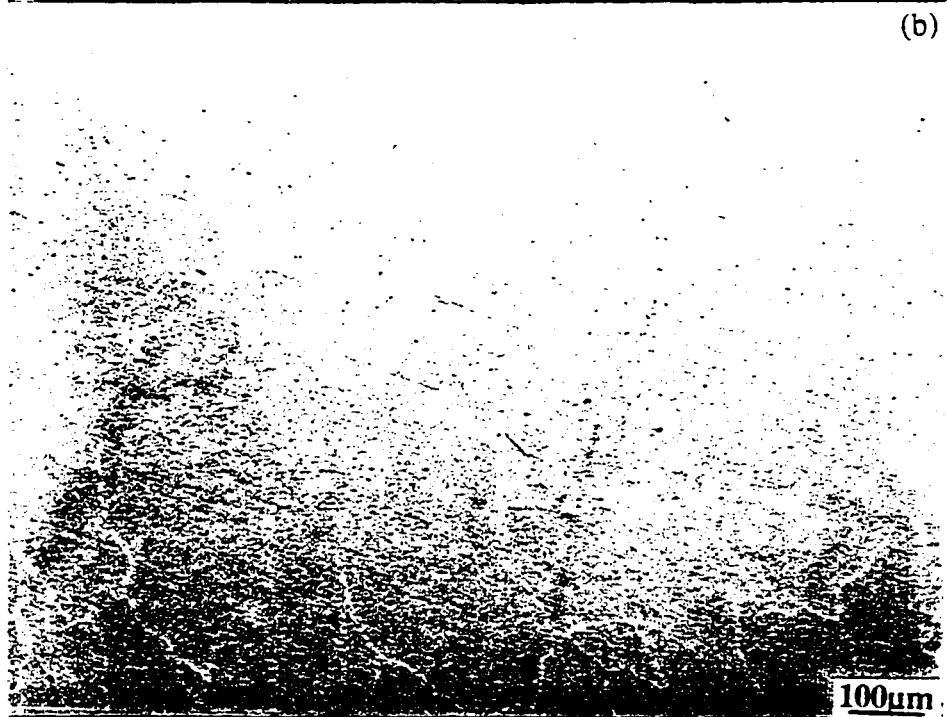
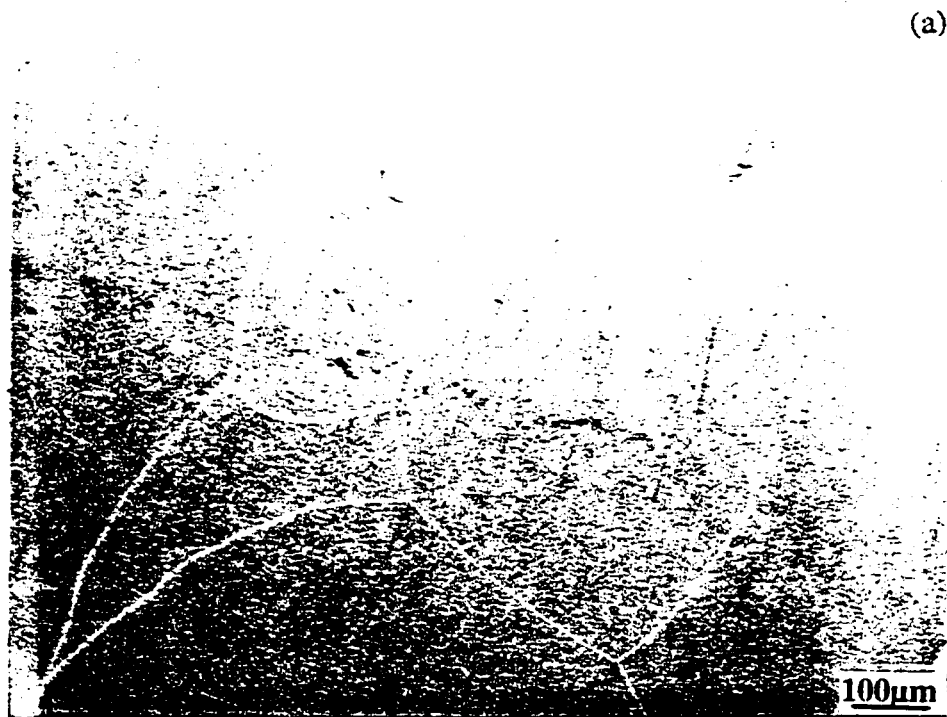


Fig.32 Optical micrographs for the alloys aged at 250°C for 140 hrs: (a) base alloy and (b) 0.4%Be alloy.

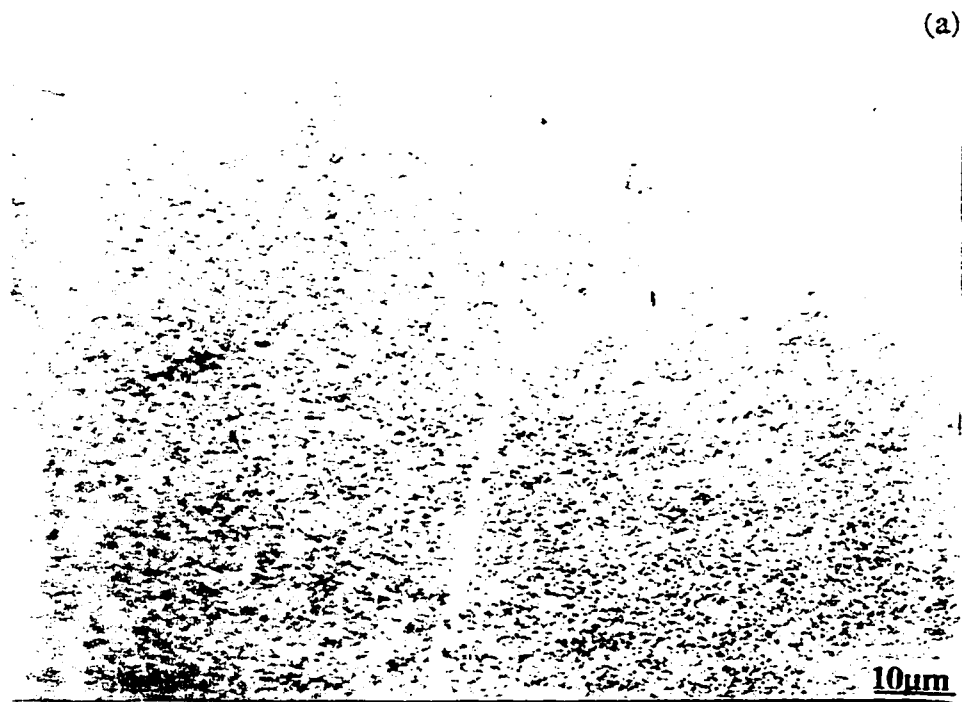


Fig.33 Optical micrographs for the alloys aged at 250°C for 140 hrs: (a) base alloy and (b) 0.4%Be alloy.

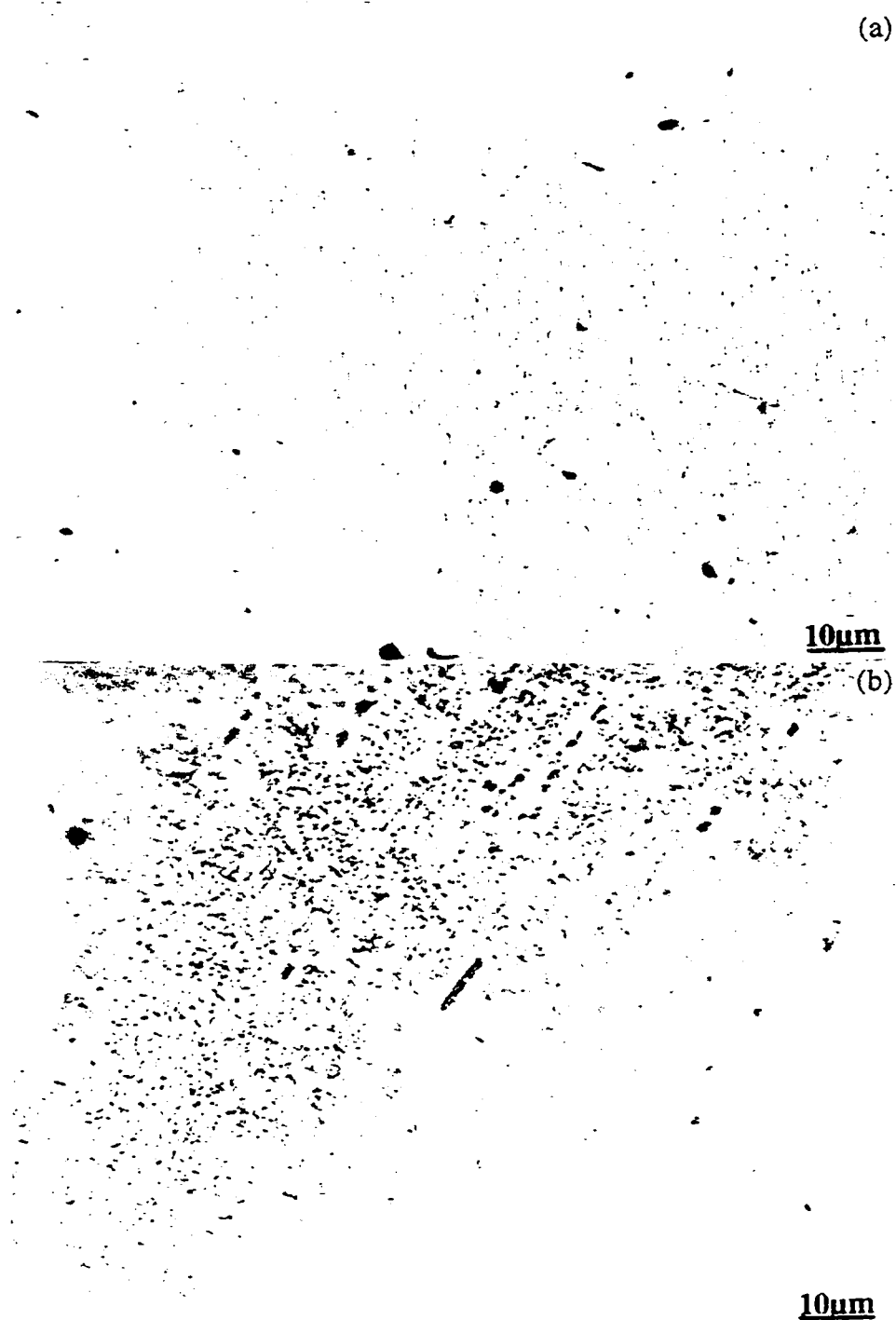


Fig.34 Optical micrographs for the alloys aged at 300°C for 17 hrs: (a) base alloy and (b) 0.4%Be alloy.

4.3 TEM Microscopical Observations

The age hardening results, optical observations, and kinetic analysis show clearly that the addition of 0.4%Be to the base alloy significantly enhances the age hardening response of the alloy, which is associated with a refinement of precipitate structures. A TEM study of the alloy microstructure at various stages of precipitation is essential to determine the specific role of Be in the alloy during the solution and aging treatments, which results in the refinement of the precipitate.

4.3.1 As-Quenched and Room Temperature Aged Alloys

4.3.1.1 Dislocation Loop Formation

Figs. 35 and 36(a-d) give the TEM micrographs and corresponding selected area diffraction patterns (SADP) for the as-quenched (5 days delay at room temperature) alloys. The Be-containing alloy shows a higher density of dislocation lines as indicated by the line segmentation (identified at A in Fig. 35(b)), where the dislocation lines meet the top and bottom surfaces of the thin foil. Figs. 35 and 36(a,c) show dislocation loops formed as a result of the collapse of discs of vacancies[74,102] (large loops at A and small loops at B (Fig.36(a,c))), with no precipitates evident at this point. Large loops are near or intersect dislocation lines, indicating the dislocation lines act as sinks for the vacancies, while small dislocation loops are present farther away from the dislocation lines. The determination of the size and density of the dislocation loops (loops/volume) were made from TEM photomicrographs using a Ladd Microcomputer Image Analyzer, and the accuracy of the calculation is estimated at $\pm 20\%$. Both the base alloy and the Be-containing alloy show no significant difference in the size of dislocation loops (as determined from enlarged

micrographs). The mean diameter of the dislocation loops is $\sim 10\text{nm}$, excluding a very few large loops. The average density of dislocation loops, as determined from 3 micrographs and a foil thickness of $\sim 100\text{nm}$ [87,88], is $\sim 2.3 \times 10^{14}/\text{cm}^3$ for the base alloy and is $\sim 7.3 \times 10^{13}/\text{cm}^3$ (approximately 3-fold less) for the Be-containing alloy. The required vacancy fraction [74] to produce the dislocation loops is approximately 5.2×10^{-6} for the base alloy vs. approximately 1.6×10^{-6} for the Be-containing alloy, and are in relatively good agreement with the vacancy fraction of 3×10^{-6} for Al-1.53% Mg_2Si reported by Thomas [74]. Based on quenching experiments on pure aluminum, Hirsch et al [102] report a vacancy fraction of $\sim 10^{-4}$ (quenching from 550°C), i.e., all the vacancies were used in the formation of loops. The present results suggest that a major fraction of vacancies in the Be-containing alloy are retained in solid solution after quenching (as a result of solute-vacancy interaction), and only vacancies that are free from solute atoms condense, collapse, and ultimately form dislocation loops. The calculated ~ 3 -fold lower vacancy fraction for dislocation loop formation for the Be-containing indicates that Be atoms are trapping vacancies, and this can be attributed to the relatively high Be-vacancy binding energy (0.26 eV [93]). Fig.37 gives the TEM micrographs and corresponding SADP for the alloys aged at room temperature for 4 months, showing that most of the dislocations have migrated (attributed to electron beam heating of the thin foil) to grain boundaries, except where they are pinned by precipitates. The Be-containing alloy has more dislocations pinned by precipitates, and is the result of the higher precipitate density in the Be-containing alloy. A similar solute-vacancy effect on dislocation loop distribution has been reported for Al-Cu-Mg alloys when small additions of Si [103], Li [104], and Be [7] are added.

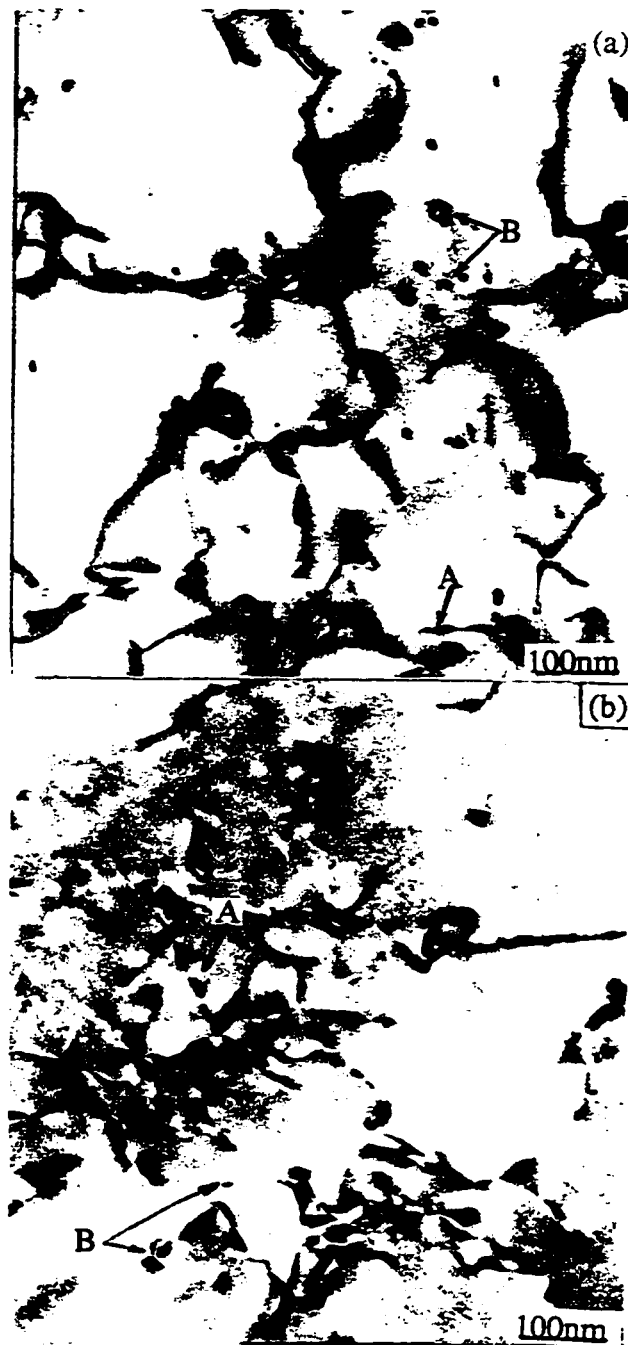


Fig.35 TEM micrographs for as-quenched (5 days delay at room temperature) alloys, showing dislocation lines chopped off at A and dislocation loops at B; (a) base alloy and (b) 0.4%Be alloy. Foil orientation [011].

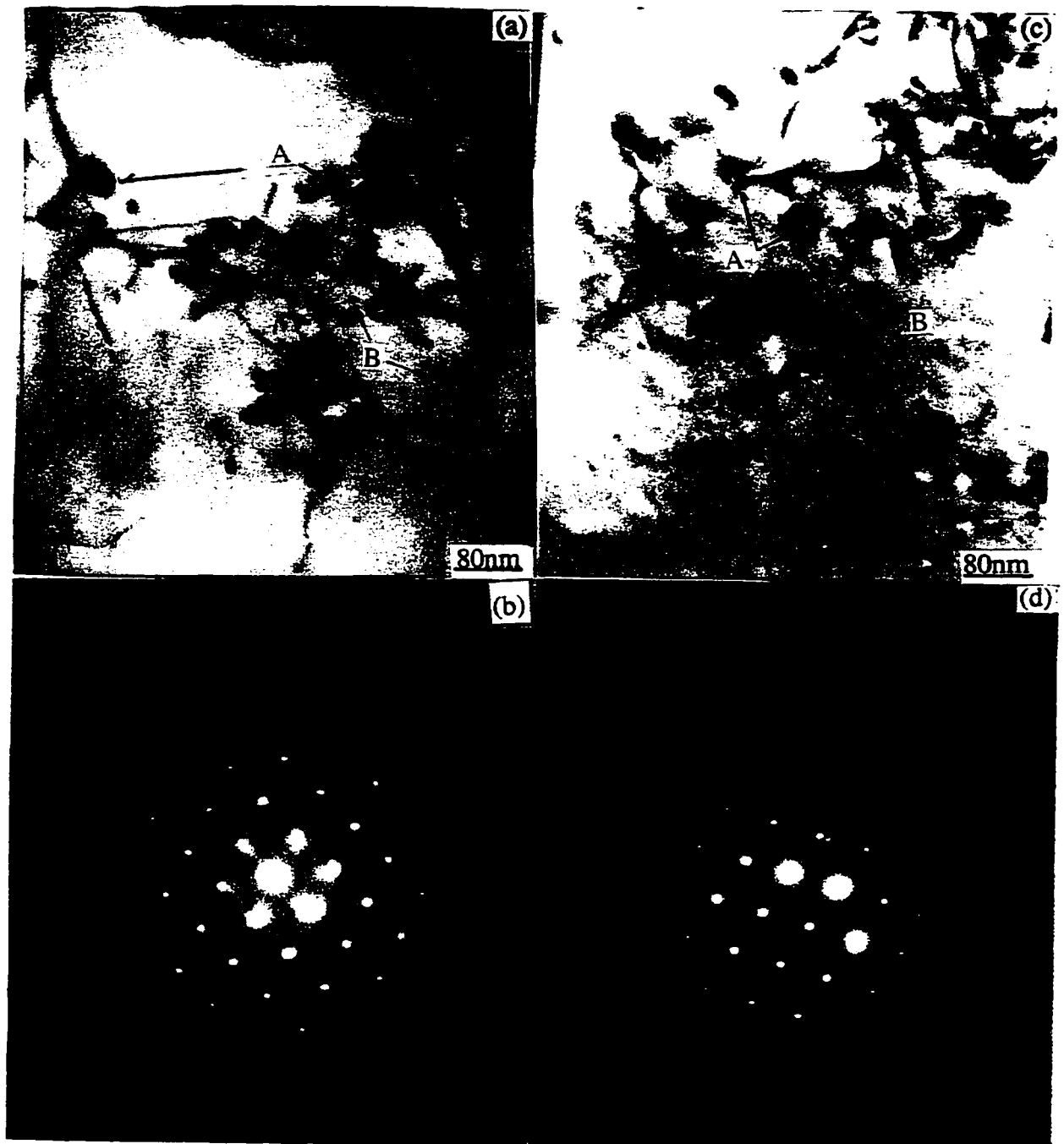


Fig.36 TEM micrograph and corresponding SADP for as-quenched (5 days delay at room temperature) alloys, showing large dislocation loops at A and small loops at B; (a,b) base alloy and (c,d) 0.4%Be alloy. Foil orientation [011].

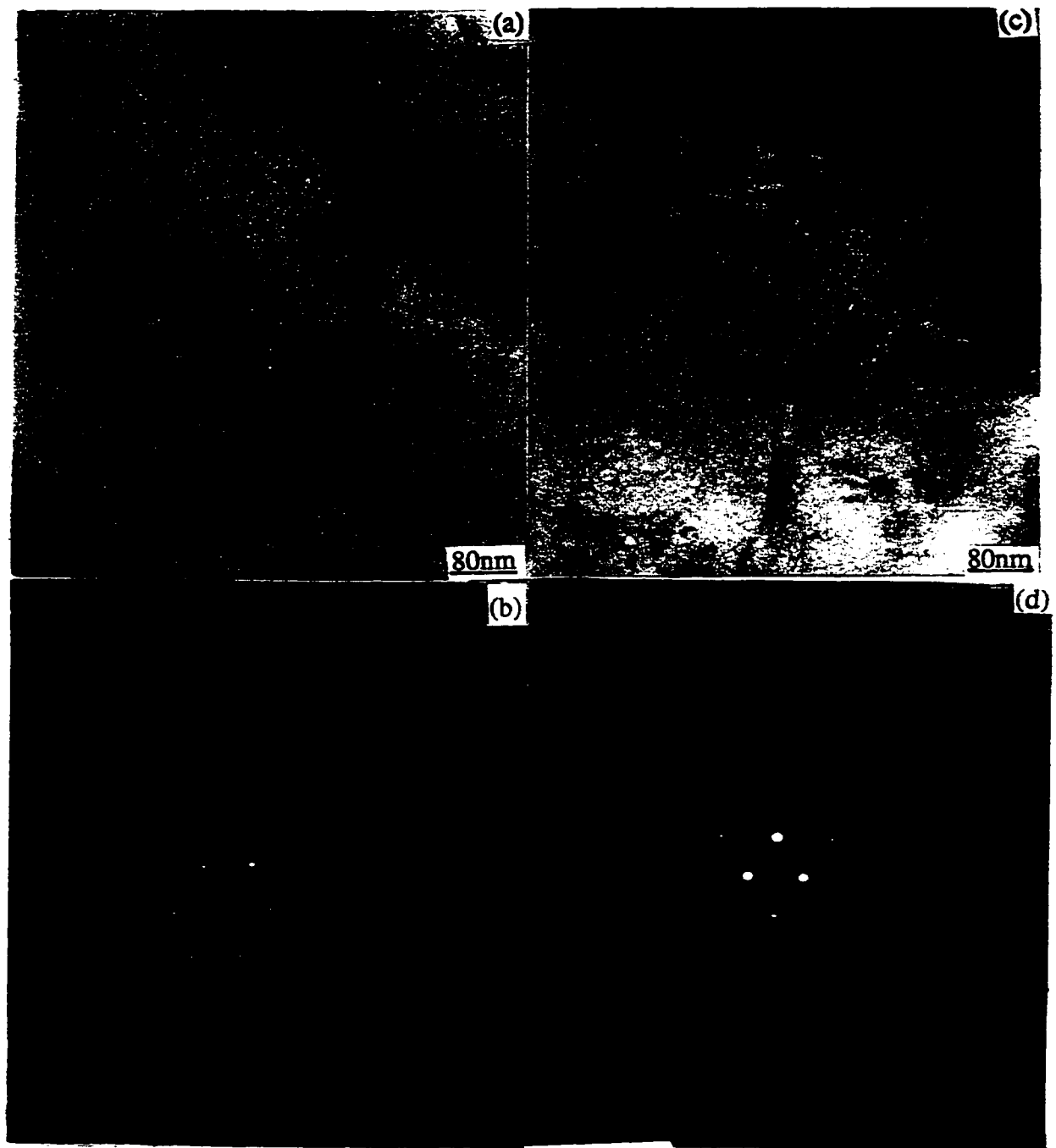


Fig.37 TEM micrograph and corresponding SADP for the alloys aged at room temperature for 4 months, showing dislocations pinned by precipitates; (a,b) base alloy and (c,d) 0.4%Be alloy. Foil orientation [011].

4.3.2 Peak Hardness Structure: β'' to β' Transition

The TEM micrographs and corresponding SADP are shown in Fig. 38 for the alloys aged to peak hardness (250°C, 65min.). The presence of β'' needles and β' rods, is evident, with approximately a 3-fold higher density of the precipitates in the Be-containing alloy. The increase in the precipitate particle density in the aged Be-containing alloy, compared with the lower dislocation loop density and higher density of dislocation lines (corresponding to a higher concentration of solute trapped vacancies) for the quenched alloy, indicates that as aging progresses at higher temperatures, the trapped vacancies are released and condense to form dislocation loops that act as sites for precipitation of more Mg_2Si particles.

The vacancy release mechanism as described here is similar to that proposed for Li-containing Al-Cu-Mg alloys. Gregson et al[105] reported that the high density of as-quenched dislocation loops in Al-Cu-Mg alloys is completely altered by the presence of Li atoms due to high Li-vacancy binding energy. More recently, Fang and Youdelis[7] have shown a similar effect for Be-containing Al-Cu-Mg alloys, and propose that the Be atoms released from the vacancies are incorporated into the Al_2CuMg precipitate (S' phase).

The β'' needles and β' rods (assumed grown from β'' needles) shown in Fig.38 have a $\langle 100 \rangle_{\text{matrix}}$ alignment. The size of β'' needles is $\sim 3\text{nm}$ in diameter and $\sim 40\text{nm}$ in length for base alloy vs. $< 2\text{nm}$ in diameter and $< 12\text{nm}$ in length for the Be-containing alloy. The size and average density of β' rods measure at $\sim 7\text{nm}$ in diameter, $> 200\text{nm}$ in length, and $\sim 6.3 \times 10^{15}/\text{cm}^3$ for the base alloy vs. $\sim 3\text{nm}$ in diameter, $20\text{--}40\text{nm}$ in length, and $\sim 2.1 \times 10^{16}/\text{cm}^3$ for the Be-containing alloy. This corresponds to a 2-3 fold reduction in diameter, a 5-10 fold reduction in length, and ~ 3 -fold increase in the β' particle density for the Be-containing alloy,

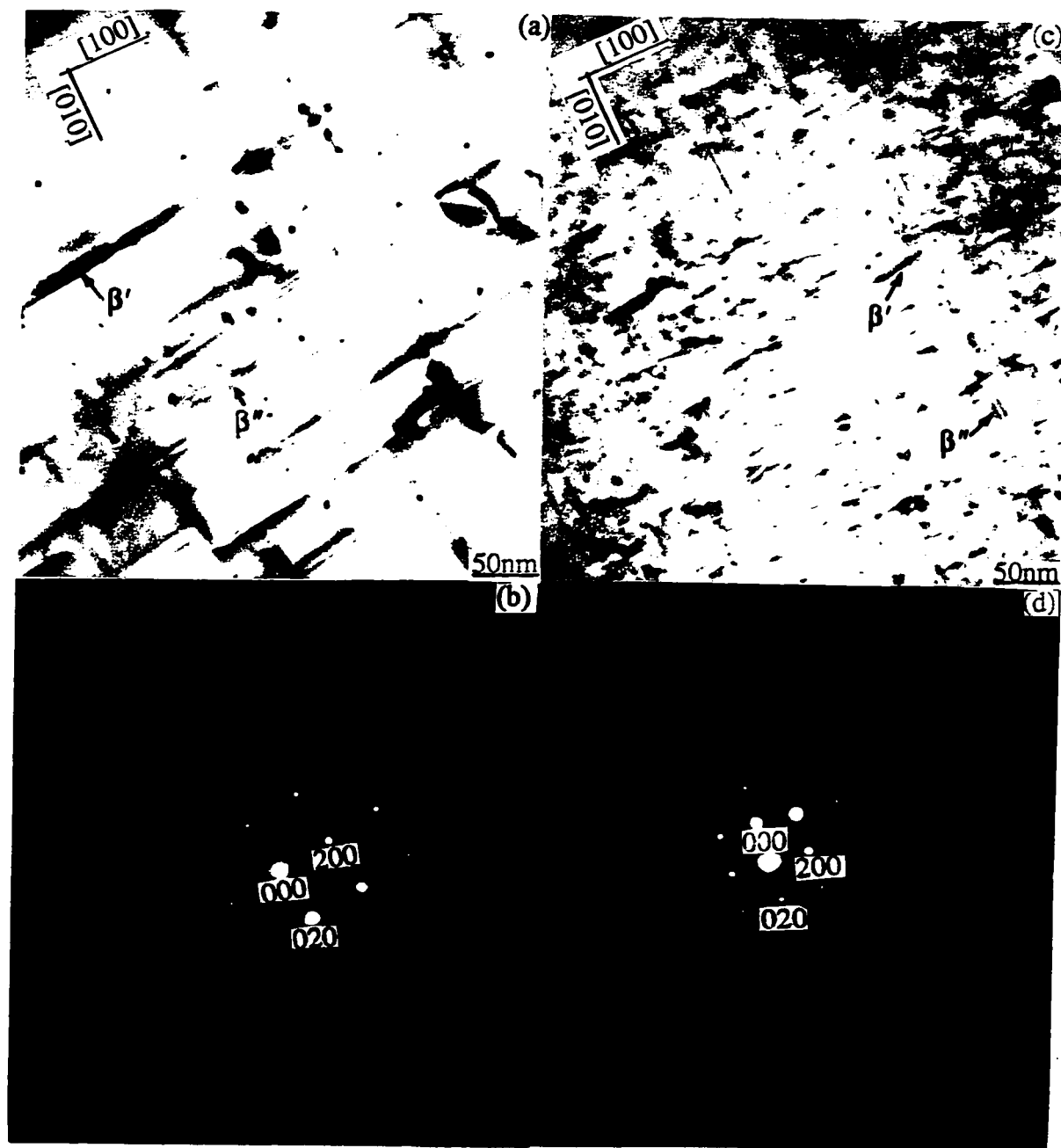


Fig.38 TEM micrograph and corresponding SADP for the alloys aged at 250 °C for 65 min., showing β'' needles and β' rods, spots are from the matrix. (a,b) base alloy and (c,d) 0.4%Be alloy. Foil orientation [001].

which is consistent with a similar increase in the nuclei density-dependent parameter (k_1) for the Be-containing alloy noted earlier.

Lynch et al[80] showed that for Al-1.16%Mg₂Si alloy aged for 3 hrs., the β' -rods grow in size up to 300nm in length and 4nm in diameter. Dutta and Allen[74] propose that β'' needles grow to β' -rods about 5.0-7.5nm in diameter and 50.0nm in length. Andersen[88] reports an average length of ~50nm for β'' needles and ~500nm for β' rods.

4.3.3 Overaged Structure: β' to β Transition

Fig. 39 gives the TEM micrographs and corresponding SADP for the overaged alloys (250°C, 600min.). For the base alloy the β' rods have grown in size to ~17nm diameter, with the density decreasing to $\sim 7.3 \times 10^{14}/\text{cm}^3$ compared with ~6.0nm and $\sim 1.6 \times 10^{15}/\text{cm}^3$ for the Be-containing alloy. Thus even in the overaged condition, with considerable coarsening of the particles, the density of β' rods for the Be-containing alloy is ~2-fold higher than for the base alloy. Fig.40 shows dislocations cut the β' rods, which ultimately break down the precipitates as they move, indicating a loss of coherency[106] and formation of incoherent β plates.

Matsuda[81], using high resolution TEM and micro-beam diffraction studies, have shown three orientation relationships between β' rods precipitate and the matrix; 0°-type: the elongated direction of the β' rods are parallel to $[100]_{\text{matrix}}$ ($(100)_{\text{matrix}}$ habit plane); 15°-type: β' -rods are parallel to the $[110]_{\text{matrix}}$ ($(110)_{\text{matrix}}$ habit plane), and middle range-type: β' -rods are parallel to the $[310]_{\text{matrix}}$ ($(130)_{\text{matrix}}$ habit plane). The present results are in good agreement with the above. The diffraction patterns for both alloys are essentially identical, suggesting that the Be addition does not alter the morphology and the growth direction of the β' -rods,



Fig.39 TEM micrograph and corresponding SADP for the alloys aged at 250 °C for 600 min., showing β' rods, spots are from the matrix. (a,b) base alloy and (c,d) 0.4%Be alloy. Foil orientation $[001]$.

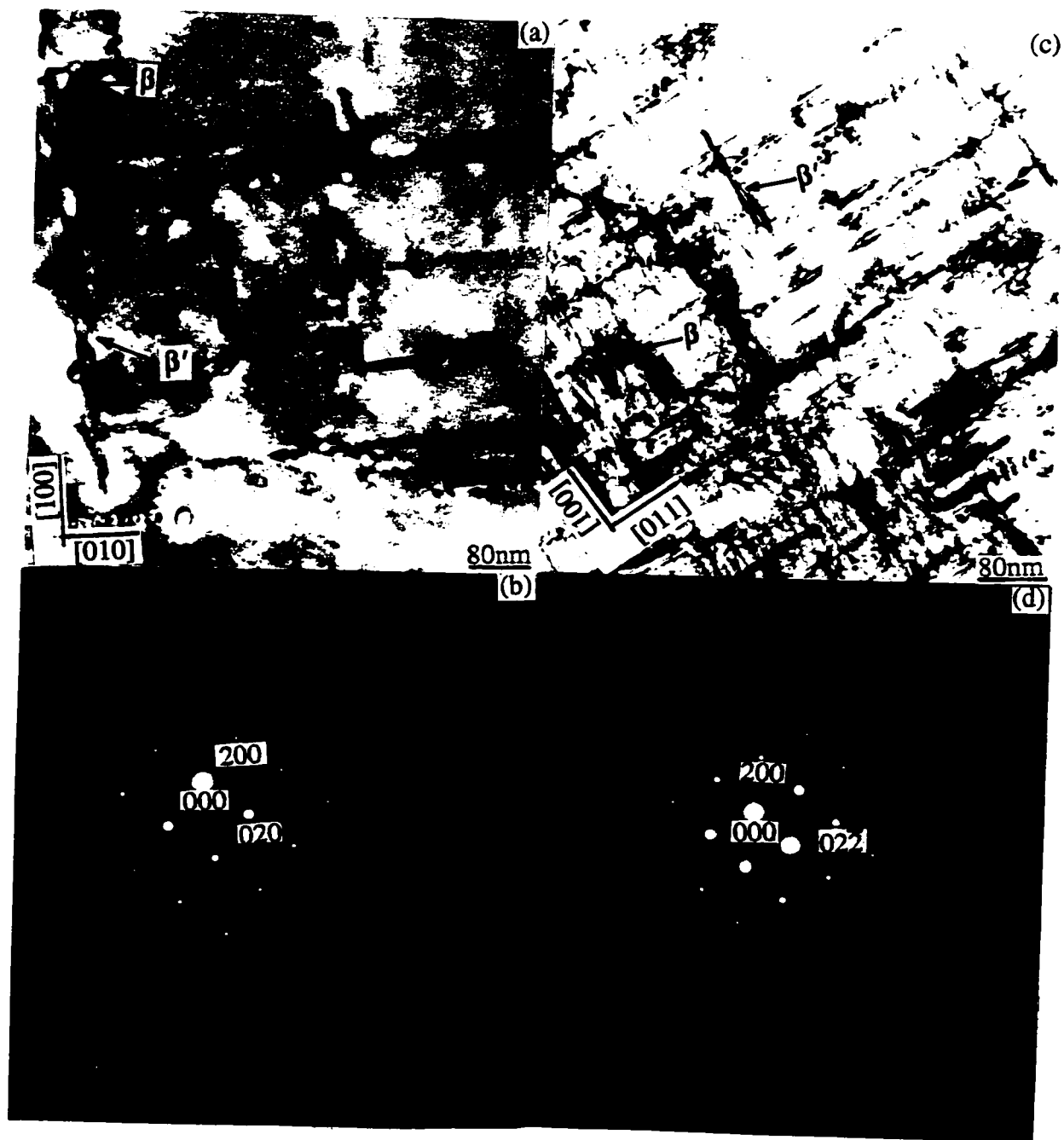


Fig.40 TEM micrograph and corresponding SADP for the alloys aged at 250 °C for 600 min., showing β' rods and β plates, spots are from the matrix. (a,b) base alloy and (c,d) 0.4%Be alloy. Foil orientation $[001]$ for base alloy and $[011]$ for 0.4%Be alloy.

but refines the precipitate and increases the density, which is consistent with the optical, age hardening, and kinetic analysis results.

CHAPTER 5

Be EFFECT ON NUCLEATION RATE OF β' PHASE

5.1 Nucleation Thermodynamics and Kinetics

The microscopical analyses (optical and TEM) show that the addition of 0.4%Be to the base alloy increases the β' particle density ~ 3 -fold, and this is consistent with the kinetic analysis, which shows a 200-300% increase in the nuclei density dependent parameter (k_1) in the modified AJM equation, without any significant changes to the growth parameter (n) or activation energy (Q_1). Thus the effect of Be is to increase the nucleation rate in the overall transformation process, and it remains to consider the factors affecting the activation energy (ΔG^*) in the nucleation rate expression (Eq.(13)), specifically, the effect of Be on the nucleation entropy (ΔS_v), the interfacial energy (γ), and the strain energy (W).

5.2 Nucleation Entropy of Mg_2Si

The mixing entropy contributions to the nucleation entropy given by Eq.(30) apply to regular solutions, but intermediate compounds or phases with limited solid solubility will be far removed from regular solution behavior, and additional thermodynamic data is required to calculate the nucleation entropy. The regular solution constraint can be removed by an appropriate combination of reactions for which entropy changes can be calculated or are given. The procedure used to calculate nucleation entropy for precipitation in solid alloys is

similar to that for primary phase nucleation in liquid alloys, except that the solidification reaction must be replaced by the appropriate solid phase transformation, and the corresponding entropy change calculated or estimated.

Table 3 gives the reaction sequence used for calculating the molar nucleation entropy of Mg_2Si in an Al-0.78 at.%Mg-0.38 at.%Si (which in wt% corresponds to Al-0.7%Mg-0.4%Si) alloy at the aging temperature of 250°C. The (reverse) formation of 1 mole (3g-atom) of a regular (behaving) solid solution of Mg-33.33 at.%Si alloy is given by reaction 1a, for which the mixing entropy per g-atom is given by

$$\Delta S^{\text{reg}} = -R(N_{\text{Mg}} \ln N_{\text{Mg}} + N_{\text{Si}} \ln N_{\text{Si}}) \quad (42)$$

The formation of 1 mole of Mg_2Si is given in reaction 2a, for which the formation entropy (at the aging temperature of 250°C) is calculated using the thermodynamic data for Mg_2Si , Mg and Si[107-109]. Adding reaction 1a to 2a gives 3a, the reaction and corresponding entropy change for the formation of 1 mole of Mg_2Si from 1 mole of regular solid solution of Mg-33.33 at.%Si alloy. Reaction 4a denotes the nucleation reaction by which 1 mole of regular solid solution of Mg-33.33 at.%Si alloy is formed or precipitated in an infinite amount of regular solid solution of Al-0.78 at.%Mg-0.38 at.%Si. The entropy change for this reaction is calculated using eqs. (27) and (28), in which the liquid phase is replaced by the supersaturated solid solution (see p.17). Thus the transformation and mixing entropy changes are

$$\Delta S_T = N_{\text{Mg}}^{\beta} (S_{\text{Mg}}^{\beta} - S_{\text{Mg}}^{\alpha}) + N_{\text{Si}}^{\beta} (S_{\text{Si}}^{\beta} - S_{\text{Si}}^{\alpha}) \quad (43)$$

$$\Delta S_M = R(N_{Mg}^{\beta} \ln(N_{Mg}^{\alpha} / N_{Mg}^{\beta}) + N_{Si}^{\beta} \ln(N_{Si}^{\alpha} / N_{Si}^{\beta})) \quad (44)$$

The transformation entropy (eq. (43)) requires the entropies for the elements in the hypothetical β structure of Mg_2Si (fcc, CaF_2 prototype). There are several theoretical approaches to estimating the lattice stability of the pseudo-structures. The method of pseudo-potentials has been applied with variable success to the problem of computing the stability of various structures of pure metals, from which the corresponding entropy changes are directly obtained (see Kaufman and Bernstein[110]). For example, for Mg (hcp- ϵ) transforming to Mg (fcc- α), Kaufman gives $\Delta G^{\epsilon-\alpha} = 1946 + 1.80 T$, or $\Delta S = -1.80$ J/mol. K. In the present case, the Al-rich solid solution phase (α) and Mg_2Si (β) are both fcc structures, so that the entropy difference would be small, assuming that the vibrational component of the total entropy change (which is comprised of vibrational and configurational components) is small. This argument also applies to Si. Thus to a first approximation, ΔS_T can be considered small and negligible compared to ΔS_M . Adding reaction 3a to 4a gives 5a. Reaction 5a gives the nucleation reaction and corresponding nucleation entropy for the formation of 1 mole of Mg_2Si from a regular solid solution of Al-0.78 at. %Mg-0.38 at. %Si at the aging temperature of 250°C. The determination of the nucleation entropy of Mg_2Si from the real supersaturated solid solution alloy requires appropriate thermodynamic information for the latter, which is not available. However, since the difference in molar entropies of mixing for regular and real solutions is small for dilute alloys (both converge and become zero at infinite dilution), the difference in the molar entropy for nucleation of Mg_2Si , in the real vs. regular solid solution will likewise be small, and for the dilute solute concentrations of the present alloy ($N_{Mg} =$

Table 3 Reaction sequence for calculating ΔS for precipitation of Mg_2Si from supersaturated Al-0.78%Mg-0.38%Si alloy at 250°C.

reaction	entropy change ΔS (J/mol.K)
1a $3(Mg-33.33\%Si)_{sol}^{reg} \rightleftharpoons 2Mg(s) + Si(s)$	-15.82
2a $2Mg(s) + Si(s) \rightleftharpoons Mg_2Si(s)$	-21.22
3a $3(Mg-33.33\%Si)_{sol}^{reg} \rightleftharpoons Mg_2Si(s)$	-37.04
4a $\infty(Al-0.78\%Mg-0.38\%Si)_{sol}^{reg} \rightleftharpoons 3(Mg-33.33\%Si)_{sol}^{reg} + \infty(Al-0.78\%Mg-0.38\%Si)_{sol}^{reg}$	-110.78
5a $\infty(Al-0.78\%Mg-0.38\%Si)_{sol}^{reg} \rightleftharpoons Mg_2Si(s) + \infty(Al-0.78\%Mg-0.38\%Si)_{sol}^{reg}$	-147.82

All concentrations are in at. %.

(s) solid

0.0078, $N_{Si} = 0.0038$) negligible (see Appendix A for detailed calculations).

5.3 Nucleation Entropy of $Mg_2SiBe_{0.15}$

The solubility of Be in Mg_2Si is based on an earlier investigation by Hatab[13], and is estimated to be ~4.8at.%, to give the ternary compound of the approximate composition $Mg_2SiBe_{0.15}$. Table 4 gives the appropriate reactions by which the nucleation entropy for $Mg_2SiBe_{0.15}$ in a supersaturated Al-0.78 at.%Mg-0.38 at.%Si-0.06 at.%Be, is obtained. Note that the Be concentration in Al(α) alloy is determined from the solvus line in Al-Be phase diagram (cf. Fig. 5). The procedure is similar to that performed for Mg_2Si except for the assumption that the entropy change for reaction 2b does not differ appreciably from the entropy of formation of Mg_2Si as given in reaction 2a. The basis for this assumption is the common crystal structure (fcc,C1 type) and lattice parameters[13] for both Mg_2Si and $Mg_2SiBe_{0.15}$ phases. The principal factors determining the entropy of a phase are structure and bond energy. Because the structures of the two compounds are essentially identical, and because the reported X-ray diffraction and microhardness results[13] indicate that the Be atoms in the ternary compound occupy the existing vacant site in the centre of a unit cell, the bond energies, and hence the entropies of the two compounds should not differ appreciably (except for the additional mixing entropy for the ternary compound). The ΔS_T term for ternary compound ($Mg_2SiBe_{0.15}$) will include an additional entropy change for Be. Since Be occupies the interstitial sites in the β phase, it cannot be assumed to take on the fcc structures of β . Hence, ΔS_T (Be), i.e., the magnitude of ($S_{Be}^{\beta} - S_{Be}^{\alpha}$) is unknown. However, in a comparison of ΔS for the binary and ternary compounds, this difference will be small and

Table 4 Reaction sequence for calculating ΔS for precipitation of $\text{Mg}_2\text{SiBe}_{0.15}$ from supersaturated Al-0.78%-0.38%Si-0.06%Be at 250°C.

reaction	entropy change ΔS (J/mol.K)
1b $3.15(\text{Mg-31.75\%Si-4.76\%Be})_{\text{sol}}^{\text{reg}} \rightleftharpoons 2\text{Mg (s)} + \text{Si (s)} + 0.15\text{Be (s)}$	-20.88
+ 2b $2\text{Mg (s)} + \text{Si (s)} + 0.15\text{Be (s)} \rightleftharpoons \text{Mg}_2\text{SiBe}_{0.15} \text{ (s)}$	~-21.22
3b $3.15(\text{Mg-31.75\%Si-4.76\%Be})_{\text{sol}}^{\text{reg}} \rightleftharpoons \text{Mg}_2\text{SiBe}_{0.15} \text{ (s)}$	~-42.10
+ 4b $\infty(\text{Al-0.78\%Mg-0.38\%Si-0.06\%Be})_{\text{sol}}^{\text{reg}} \rightleftharpoons 3.15(\text{Mg-31.75\%Si-4.76\%Be})_{\text{sol}}^{\text{reg}} + \infty(\text{Al-0.78\%Mg-0.38\%Si-0.06\%Be})_{\text{sol}}$	-115.34
5b $\infty(\text{Al-0.78\%Mg-0.38\%Si-0.06\%Be})_{\text{sol}}^{\text{reg}} \rightleftharpoons \text{Mg}_2\text{SiBe}_{0.15} \text{ (s)} + \infty(\text{Al-0.78\%Mg-0.38\%Si-0.06\%Be})_{\text{sol}}$	~-157.44

negligible, since $N_{\text{Be}}^{\beta} \sim 0.005$.

Thus only the entropy change for reaction 2b in Table 4 introduces some degree of uncertainty; however, the assumption of approximately equal entropy changes for reactions 2a and 2b is reasonable, based on the structural similarity of the phases. The higher nucleation entropy for $\text{Mg}_2\text{SiBe}_{0.15}$ (157.44 vs. 147.82 J/mol.K) is due almost entirely to the increase in mixing entropy when Be is incorporated into Mg_2Si .

5.4 Determination of Strain Energy

β' is reported to be semicoherent with $\text{Al}(\alpha)$ matrix[79-81], and as such contains interfacial dislocations for lattice matching. Thus some of the elastic strain energy associated with the nucleus is replaced by interfacial dislocations, which contribute to the interfacial energy. The problem of strain energy arising from the difference in lattice parameters between the precipitate and the matrix (lattice misfit, δ) has been treated by Nabarro[26]. Assuming that all strains are stored in the matrix, an elastically isotropic matrix, equivalent moduli for the matrix and precipitate, and a coherent interface, the strain energy (W) for the misfit is given by[26]

$$W = (2/9) ((1+\nu)/(1-\nu)) \mu_{\alpha} \epsilon^2 \quad (45)$$

where ν is Poisson's ratio (0.33), $\mu_{\alpha} = (E/2(1+\nu))$ the matrix shear modulus ($E = 72$ Gpa for Al alloys[111]), and ϵ the stress-free transformation strain given by (see Jena and Chaturvedi[112])

$$\varepsilon \approx (1/3)(\Delta V/V) \approx ((V_\beta - V_\alpha)/3V_\beta) \quad (46)$$

where the molar volumes are $V_\beta = 12.887$, $V_\alpha = 10.013$ for base alloy, and $V_\beta = 12.946$, $V_\alpha = 10.057 \text{ cm}^3/\text{g. atom}$ for the Be-containing alloy[13]. The above give for W and ε $\sim 6.60 \times 10^7 \text{ J/m}^3$ and $\sim 7.43\%$ for the base alloy vs. $\sim 6.62 \times 10^7 \text{ J/m}^3$ and $\sim 7.44\%$ for the Be-containing alloy.

5.5 Nucleation Rate Comparison

In many reports of TEM observations for nucleation in solids, it is shown that the nucleation sites are not distributed randomly, but are concentrated at particular sites in the matrix (defects). The defects that act as the heterogeneous sites for nucleation are grain boundaries, dislocations, stacking faults, vacancy clusters (dislocation loops) etc., and are high energy sites which can induce preferential nucleation.

For homogeneous nucleation involving strain energy, the Gibbs free energy change of formation of a spherical critical-sized nucleus is given by (cf eq.(6))

$$\Delta G = (4/3)(\pi r^3)(\Delta G_v + W) + (4\pi r^2)(\gamma) \quad (47)$$

Minimizing ΔG with respect to r , gives the value of a critical-sized nucleus

$$r^* = -2\gamma/(\Delta G_v + W) \quad (48)$$

which combined with eq.(47) gives the nucleation activation energy

$$\Delta G^*_{\text{hom}} = (16\pi\gamma^3)/3(\Delta G_v + W)^2 \quad (49)$$

The homogeneous nucleation rate is given by (cf eq.(3))

$$\dot{N}_{\text{hom}} \propto \exp(-(16\pi\gamma^3)/3(\Delta G_v + W)^2) / kT \quad (50)$$

The interfacial energy is not available, and for the purpose of calculation the interfacial energy for the semicoherent θ' phase in Al-Cu alloy is used, i.e., $\gamma_{\alpha\beta'} = 0.110 \text{ J/m}^2$ for both compounds. The reported interfacial energies for Al for grain boundary, stacking fault, and coherent twin boundary are respectively 0.324, 0.166, and 0.075 J/m²[113]. For Al-Cu alloy the $\theta(\text{CuAl}_2)/\text{Al}$ interfacial energy increases according to the precipitation sequence; i.e., for coherent GP zones $\gamma \sim 0.010\text{-}0.030 \text{ J/m}^2$ [112], for semicoherent $\gamma \sim 0.090\text{-}0.110 \text{ J/m}^2$ [114], and for incoherent $\gamma \sim 0.295 \text{ J/m}^2$ [113]. It is evident that interfacial energy depends on the type of interface (coherent, semicoherent, or incoherent) between the precipitate and the matrix.

A comparison of nucleation rates for a spherical nucleus of the β' phase with and without Be, determined using eqs.(49) and (50), is summarized in Table 5 for two values of interfacial energy.

The results in Table 5 show a decrease in $\Delta G^* \sim 13\%$ and increase in nucleation rate ~ 1.7 times for the Be-containing alloy, which is attributed to an increase in $|\Delta G_v| \sim 7\%$.

Table 5 Comparison of nucleation rates for β' -Mg₂Si and β' -Mg₂SiBe_{0.15} at 250°C.

Parameters	β' -Mg ₂ Si	β' -Mg ₂ SiBe _{0.15}
$\Delta G_v = -\Delta S_v \Delta T$ (J/m ³)	-9.55×10^8	-1.02×10^9
$\gamma_{\alpha\beta'}$ (J/m ²) $\gamma_{\alpha\beta'}$ (J/m ²)	0.110 0.200	0.110 0.200
W (J/m ³)	6.60×10^7	6.62×10^7
$\gamma_{\alpha\beta'} = 0.110$ ΔG_{hom}^* (J/critical nucleus) (J/mol.)	2.82×10^{-20} 16976	2.45×10^{-20} 14749
$\gamma_{\alpha\beta'} = 0.200$ ΔG_{hom}^* (J/critical nucleus) (J/mol.)	1.70×10^{-19} 102340	1.47×10^{-19} 88494
$\gamma_{\alpha\beta'} = 0.110$ $N_{Mg_2SiBe_{0.15}} / N_{Mg_2Si}$	1	1.7
$\gamma_{\alpha\beta'} = 0.200$ $N_{Mg_2SiBe_{0.15}} / N_{Mg_2Si}$	1	24

An increase in interfacial energy further increases the nucleation rate difference for the Be-containing alloy over the base alloy (1:24), due to the larger ΔG^* .

The TEM observations of this investigation (Figs. 35,36) show the presence of dislocation loops and lines, which act as sites for heterogeneous nucleation of β' rods. However, due to the lack of appropriate data for the contact angle θ at the α/β' interface, and interfacial energy, a similar comparison for the heterogeneous nucleation case is omitted. The above calculations are useful only for a comparative purposes; however, it gives some insight into the specific role of Be in stimulating the precipitation of β' phase in the Al-Mg-Si alloy, in particular the enhanced age-hardening response and refinement of the precipitate.

CHAPTER 6

CONCLUSIONS

AND

RECOMMENDATIONS

6.1 Conclusions

1. The addition of 0.4%Be to Al-0.7%Mg-0.4%Si alloy significantly increases the peak hardness levels obtained on age hardening, and is associated with a refinement and increase in the particle density of β' precipitate.
2. The Be addition decreases the grain size for both the columnar and equiaxed zones of the casting alloys and significantly inhibits grain growth during solution treatment and aging.
3. The modified AJM kinetic parameters for β' precipitation (n , k_1 , Q_1), obtained from hardness and resistivity data are in good agreement, and is evidence of the equivalence of the two methods for monitoring transformation rates.
4. An analysis of kinetic data using the modified AJM equation shows Be does not alter the growth parameter (n), but increases 2-3 fold the nuclei density dependent parameter (k_1), which is in agreement with the 2-3 fold increase in the β' -rod precipitate density for the Be-containing alloys.
5. The activation energies obtained fall in the accepted range for vacancy diffusion in Al as the transport mechanism controlling the rate of β' formation for both alloys.
6. The increase in the precipitate particle density in the aged Be-containing alloy, compared with the lower dislocation loop density and higher density of dislocation lines

(corresponding to a higher concentration of Be-trapped vacancies) for the quenched alloy, indicates that as aging proceeds at higher temperatures, the trapped vacancies are released and condense to form dislocation loops that act as sites for β' nucleation.

7. Relative nucleation rate calculation shows that the ~ 1.7 -fold increase in nucleation rate for the Be-containing alloy is due to an increase in $|\Delta G_v| \sim 7\%$.

6.2 Recommendations

Light-weight materials have been targeted as the promising materials for transportation vehicles to decrease fuel consumption and environmental pollution, and the age-hardenable aluminum alloys are the obvious choice for both castings (engine blocks, heads, etc.) and structural applications (chassis). The Al-0.7%Mg-0.4%Si (6063-type) alloy provides an attractive material selection for this purpose, particularly as castability is relatively good and it has good mechanical properties. However, the alloy can be further enhanced, i.e. the age-hardening response in a higher peak hardness and accelerated aging rate. The results of the present investigation show that the precipitation hardening of this alloy is significantly improved by Be microalloying; however, for Be-microalloying to be accepted as standard industrial practice, the following structure-property information needs to be generated as an applied research project:

1. Comprehensive mechanical testing of the Al-Mg-Si alloy (UTS, YS, fracture toughness, and fatigue) to determine the optimum microstructures to maximize the mechanical properties.
2. Determine the optimum levels of Be for the Al-0.7%Mg-0.4%Si alloy to obtain the

desired age-hardening response and refinement in precipitate structure. Earlier work has shown that a Be content of only 0.1% gives significant improvement in the age-hardening properties.

Applied research and development in any area will progress only to the extent that essential basic scientific information available. In this regard the following basic research should be undertaken.

1. A more detailed determination of the effect of Be on the crystal structure of β' , and its crystallographic orientation relationship to the $\text{Al}(\alpha)$ is required. This may be possible using High Resolution Transmission Electron Microscopy (HRTEM).

2. A more accurate determination of the Be solubility in β' phase, and the solubilities of Mg and Si in $\text{Al}(\alpha)$ saturated with Be is essential for more accurate nucleation entropy calculations. The application of Auger techniques is suggested.

REFERENCES

- [1] S.P.Iyer and W.V.Youdelis: *Aluminum*, 1977, vol.53, p.252.
- [2] W.V.Youdelis: *Met. Sci.*, 1979, vol.13, p.540.
- [3] W.V.Youdelis and C.S.Yang: *Mat. Sci.*, 1982, vol.16, p.275.
- [4] W.V.Youdelis and W.Fang: *Mat. Sci. And Tech.*, 1991, vol.7, p.201.
- [5] J.Karov and W.V.Youdelis: *Mat. Sci. And Tech.* , 1987. Vol.3, p.1.
- [6] W.V.Youdelis and J.Karov: *Mat. Sci. Forum*, 1987, vol.13-14, p.483.
- [7] W.Fang and W.V.Youdelis: "*Effect of Be on the defect Structure and Morphology of S'Precipitation in Pseudo-Binary Al(a)-S(Al₂CuMg) Alloy*," Proc. Inter. Symposium on Advances in Production and Fabrication of Light Metals,Edmonton, Canada, Aug.1992, The Metallurgical Society of CIM, p.339-349.
- [8] W.V.Youdelis and W.Fang: "*The effect of Be on the Age Hardening of Al-2.5Cu-1.2Mg Alloy*," Proc. Of Inter. Conf. On Recent Advances in Science and Engineering of Light Metals, Japan Inst. Of Light Metals, Tokyo, Japan, Oct.1991,Ed.K.Hirano, H.Oikawa and K.Ikeda, p.917.
- [9] A.Luo and W.V.Youdelis: "*The Effects of V and Be Microadditions on Age Hardening Behaviour of Al-Li Alloy 8090*", Proc. Of Inter. Symposium on Extraction, Refining and Fabrication of Light Metals, Ottawa, Canada, 1991, Pergamon Press, p.423-433.
- [10] A.Luo and W.V.Youdelis: "*Effects of V and Be on S'(Al₂CuMg) Precipitation in Al-Li-Cu-Mg Alloy 8090*", *Mat. Sci. and Tech.*, 1993, vol.9, p.781-784.
- [11] T.Xiao and W.V.Youdelis: *Proc. Int. Symp. On "Reduction and Casting of Aluminum*," 1988, vol.8, ed. C. Bickert, Oxford, Pergamon Press, p.37.
- [12] T.Xiao and W.V.Youdelis: *Mat. Sci. and Tech.*, 1989, vol.5(10), p.991.
- [13] Ali Hatab: *M.A.S. Thesis*, 1992, University of Windsor, Windsor, Ontario, Canada.
- [14] M.Volmer and A.Weber: *Z. Phys. Chem.*, 1925, vol.119, p.277.
- [15] R.Becker and W.Doring: *Ann. Phys.*, 1935, vol.24, p.719.

- [16] D.Turnbull and J.C.Fisher: *J. Chem. Phys.*, 1949, vol.17, p.71.
- [17] I.S.Servi and D.Turnbull: *Acta Metall.*, 1966, vol.14, p.161.
- [18] A.Kelly and R.B.Nicholson: *Prog. Mat. Sci.*, 1963, vol.10, p.151.
- [19] J.W.Christian: *The Theory of Transformations in Metals and Alloys*, 1975, 2nd Ed., Pergamon Press, Oxford.
- [20] K.C.Russell: *Phase Transformations*, 1970, ASM, Metals Park, OH. , USA, p.219.
- [21] R.B.Nicholson: *Phase Transformations*, 1970, ASM, Metals Park, OH. , USA, p.269.
- [22] H.I.Aaronson, J.K.Lee and K.C.Russell: *Precipitation Process in Solids*, 1978, Eds. K.C.Russell and H.I.Aaronson, Met. Soc. AIME, Warrendale, PA., USA, p.31.
- [23] K.C.Russell: *Adv. Colloidd and Interface Sci.*, 1980, vol.13, p.205.
- [24] W.V.Youdelis: *Met. Sci.*, 1975, vol.9, p.464.
- [25] R.D.Doherty: *Physical Metallurgy, Part II*, 1983, Eds. R.W.Cahn and P.Hassen, North-Holland Physics Publishing, Amsterdam, p.933.
- [26] F.R.N.Nabarro: *Proc. Roy. Soc.*, 1940, vol.A175, p.519.
- [27] J.K.Lee and W.C.Johnson: *Solid-State Phase Transformations*, The Pittsburg Conference, 1983, Ed. H.I.Aaronson, Met. Soc. AIME, Warrendale, PA., USA, p.127.
- [28] J.K.Lee, Y.Y.Earmme, H.I.Aaronson, and K.C.Russell: *Met. Trans.*, 1980, vol.11A, p.1837.
- [29] J.D.Eshelby: *Proc. Roy. Soc.*, 1957, vol.a241, p.376.
- [30] J.D.Eshelby: *Prog. In Solid Mechanics*, 1961, vol.2, p.89.
- [31] J.K.Lee, D.M.Barnett and H.I.Aaronson: *Met. Trans.*, 1977, vol.8A, p.963.
- [32] J.K.Lee and W.C.Johnson: *Scripta Met.*, 1977, vol.11, p.477.

- [33] J.Burke: *The Kinetics of Phase Transformation in Metals*, 1965, Pergamon Press, Oxford, p.132.
- [34] N.Raghaven and M.Cohen: *Treatise on Solid State Chemistry*, 1975, vol.5, Ed. N.B.Hannay, Plenum Press, p.67.
- [35] R.B.Nicholson: *Phase Transformations*, 1970, ASM, Metals Park, OH, p.269.
- [36] H.B.Aaron and H.I.Aaronson: *Met. Trans.*, 1971, vol.2, p.23.
- [37] J.W.Cahn: *Acta Metall.*, 1956, vol.4, p.441.
- [38] J.W.Cahn: *Acta Metall.*, 1957, vol.5, p.168.
- [39] E.Hornbogen and M.Roth: *Zeit. Metallkunde*, 1967, vol.58, p.842.
- [40] W.C.Leslie: *Acta Metall.*, 1961, vol.9, p.1004.
- [41] R.Gomez-Ramirez and G.M.Pound: *Met. Trans.*, 1973, vol.4, p.1563.
- [42] C.C.Dollins: *Acta Metall.*, 1970, vol.18, p.1902.
- [43] B.Ya.Lyubov and V.A.Solv-Yev: *Fiz. Metal. Metallography*, 1965, vol.19, p.333.
- [44] F.C.Larche: *Dislocations in solids*, 1979, vol.4, ed. F.R.N.Nabarro, North-Holland Publishing company, Amsterdam, p.135.
- [45] G.W.Lorimer and R.B.Nicholson: *The Mechanisms of Phase Transformations in Crystalline Solids*, 1969, The Metals Society, London, p.36.
- [46] M.H.Jacobs and D.W.Pashley: *The Mechanisms of Phase Transformations in Crystalline Solids*, 1969, The Metals Society, London, p.43.
- [47] A.H.Cottrell: *Report on Strength of Solids*, 1948, The Physical Society, London.
- [48] J.S.Koehler and F.Seitz: *J. Appl. Mech.*, 1947, vol.14, p.217.
- [49] A.K.Jena and M.C.Chaturvedi: *Phase Transformation in Materials*, 1992, Prentice Hall, Inc., USA.
- [50] W.V.Youdelis and O.Kwon: *Met. Sci.*, 1983, vol.17, p.379.
- [51] W.V.Youdelis and O.Kwon: *Met. Sci.*, 1983, vol.17, p.385.

- [52] G.W.Delamore and R.W.Smith: *Met.Trans.*, 1971, vol.2, p.1733.
- [53] M.Avrami: *J. Chem. Phys.*, 1939, vol.7, p.1103.
- [54] W.A.Johnson and R.F.Mehl: *Trans. A.I.M.E.*, 1939, vol.135, p.416.
- [55] C.Wert and C.Zener: *J. Appl. Phys.*, 1950, vol.21, p.5.
- [56] M.B.Berkenpas, J.A.Barnard, R.V.Ramaniyan, and H.I.Aaronson: *Scripta Met.*, 1986, vol.20, p.323.
- [57] A.Luo, D.J.Lloyd, A.Gupta and W.V.Youdelis: *Acta Metall. Mat.*, 1993, vol.41, No.3, p.769.
- [58] A.Luo and W.V.Youdelis: " *New Analytical Method for Calorimetric Studies of Precipitation Kinetics in Aluminum Alloys*", C.Bickert, M.Bouchard, G.Davies, E.Ghali and E.Jiran, Eds., Int. Symp. on Light Metals Processing and Applications, Met. Soc.CIM, 1993, p.437.
- [59] C.Zener: *J. Appl. Phys.*, 1949, vol.20, p.950.
- [60] J.L.Murray: *Bull. Alloy phase Diagrams*, 1982, vol.3, p.129.
- [61] W.B.Pearson: *Handbook of Lattice Spacings and Structures of Metals*, 1967, vol.1, Pergamon Press Ltd, p.367.
- [62] J.L.Murray and A.J.McAlister: *Bull. Alloy Phase Diagrams*, 1984, vol.5, p.164.
- [63] W.B.Pearson: *Handbook of Lattice Spacings and Structures of Metals*, 1967, vol.1, Pergamon Press Ltd, p.382.
- [64] W.A.Anderson: *Precipitation from Solid Solution*, 1959, ASM, Cleveland, OH, p.155.
- [65] L.F.Mondolfo: *Aluminum Alloys, Structure and Properties*, 1976, Butterworths, London.
- [66] W.B.Pearson: *Handbook of Lattice Spacings and Structures of Metals*, 1967, vol.1, Pergamon Press Ltd, p.317.
- [67] J.L.Murray and D.J.Kahan: *Bull. Alloy phase Diagrams*, 1983, vol.4, p.50.
- [68] W.B.Pearson: *Handbook of Lattice Spacings and Structures of Metals*, 1967,

vol.1, Pergamon Press Ltd, p.316.

- [69] H.Nowotny: *Z. Metallunde*, 1946, vol.37, p.146.
- [70] N.D.Nagorskaya, I.N.Fridlyander, and K.P.Yatsenko: *Russian Metall.*, 1966, vol.5, p.71.
- [71] I.N.Fridlyander, K.P.Yatsenko, and G.A.Nekrasova: *Met.Sci. And Heat Treat.*, 1970, vol.5, p.599.
- [72] W.B.Pearson: *Handbook of Lattice Spacings and Structures of Metals*, 1967, vol.1, Pergamon Press Ltd, p.317.
- [73] I.Dutta and S.M.Allen: *J. Mat. Sci. Letters*, 1991, vol.10, p.323.
- [74] G.Thomas: *J. Inst. Metals*, 1961-62, vol.90, p.57.
- [75] A.H.Geisler and J.K.Hill: *Acta Cryst.*, 1948, vol.1, p.238.
- [76] A.Guinier and H.Lambot: *Compt.Rend.*, 1948, vol.227, p.74.
- [77] A.Lutts: *Acta Met.*, 1961, vol.9, p.577.
- [78] W.F.Smith: *Metall. Trans.*, 1973, vol.4, p.2435.
- [79] J.P.Lynch, L.M.Brown and M.H.Jacobs: *Acta Met.*, 1982, vol.30, p.1389.
- [80] M.H.Jacobs: *Phil. Mag.*, 1972, vol.26, p.1.
- [81] K.Matsuda, S.Tada and S.Ikeno: *J. Electron Microsc.*, 1993, vol.42, p.1.
- [82] I.J.Polmear: *J. Australian Inst. Metals*, 1966, vol.11, p.246.
- [83] J.T.Vietz and I.J.Polmear: *J. Inst. Metals*, 1966, vol.94, p.410.
- [84] D.A.Granger and R.R.Sawtell: *J.A.F>S. Trans.*, 1984, vol.92, p.579.
- [85] M.B.Al'tman, N.S.Postnikov and L.I.Loktionova: *Met. Sci. And Heat Treat.*, 1964, p.348.
- [86] S.Nishi and T.Shinoda: *J. Japane Inst. Light Metals*, 1972, vol.22, p.325.
- [87] S.J.Andersen: *Met. And Mat. Trans.*, 1995, vol.26A, p.1931.

- [88] J.Washburn, A.Kelly and G.K.Williamson: *Phil. Mag.*, 1960, vol.5, p.192.
- [89] J.D.Livigston: *J. Appl. Phys.*, 1960, vol.31, p.1071.
- [90] W.V.Youdelis and W.Fang: *Mat. Sci. And Tech.*, 1994, vol.10, p.1031-1041.
- [91] C. Panseri and T.Federighi: *J. Inst. Metals*, 1966, vol.94, p.99.
- [92] I.Kovacs, J.Lenvai and E.Nagy: *Acta Metall.*, 1972, vol.20, p.975.
- [93] E.S.Dwarakadasa: *Scripta Metall.*, 1972, vol.6, p.187.
- [94] J.Karov, W.V.Youdelis and R.Hering : *Mat. Sci. And Tech.* , 1986, vol.2, p.547.
- [95] C.Wert: *J. Appl. Phys.*, 1949, vol.20, p.943.
- [96] F.S.Ham: *J.Appl. Phys.*, 1959, vol.30, p.1518.
- [97] A.H.Cottrell and B.A.Bilby: *Proc. Phys. Soc. (London) series A*, 1949, vol.62, p.49.
- [98] S.Harper: *Phys. Rev. Soc. (London) series A*, 1949, vol.62, p. 49.
- [99] R.D.Doherty: *Phsical Metallurg Part II*, Ed. R.W.Cahn and P.Haasen, 1983, p.988.
- [100] D.Turnbull, H.S.Rosenbaum and H.N.Treafis: *Acta Metall.*, 1960, vol.8, p. 277.
- [101] P.G.Shewmon: *Transformation in Metals*, McGraw-Hill, N.Y., USA, 1967, p.72.
- [102] P.B.Hirsch, J.Silcox and R.E.Smallman: *Phil. Mag.*, 1958, vol.3, p.897.
- [103] R.N.Wilson, D.M.Moore and P.J.E.Forsyth: *J. Inst. Of Metals*, 1967, vol.95, p.177.
- [104] S.Cersara, A.Giarda and A.Sanchez: *Phil. Mag.*, 1977, vol.35, p.97.
- [105] P.J.Gregson, H.M.Flower and A.K.Makhopa: *Mat. Sci. And Tech.*, 1986, vol.2, p.349.
- [106] G.C.Weatherly and R.B.Nicholson: *Phil. Mag.*, 1968, vol.17, p.801.
- [107] O.Kabaschewski and C.B.Alcock: *Metallurgical Thermochemistry*, Pergamon

Press, USA, 1979.

- [108] Handbook of Chemistry and Physics, 69th edition, 1988-89, p.5-16 .
- [109] I.Barin and O.Knacke: *Thermo Chemical Properties of Inorganic Substance*, Springer-Verlay, USA, 1977.
- [110] L.Kaufman and H.Bernstein: *Computer Calculation of Phase Diagrams*, Refractory Materials Academic Press, vol.4, 1970, p.31, 185.
- [111] Metals Handbook, Mechanical Testing, 9th edition, vol.8,1985.
- [112] A.K.Jena and M.C.Chaturvedi: *Phase Transformation in Materials*, Prentice Hall, New Jersey, USA, 1992, p.146,306.
- [113] L.E.Murr: *Interfacial Phenomena in Metals and Alloys*, Addison-Wesley, USA, 1975, p.82.
- [114] J.W.Martin and R.D.Doherty: *Stability of Microstructure in Metallic Systems*, Cambridge University Press, UK, 1976, p.203.

APPENDIX A

Nucleation Entropy Calculation

Reaction 1a

$$\begin{aligned}\Delta S^{\text{res}} &= R(N_{\text{Mg}} \ln N_{\text{Mg}} + N_{\text{Si}} \ln N_{\text{Si}}) \\ &= (3)(1.98)(0.6667 \ln 0.6667 + 0.3333 \ln 0.3333) \\ &= -3.78 \text{ cal/mol.K} = -15.82 \text{ J/mol.K}\end{aligned}$$

Reaction 2a

$$\begin{aligned}\Delta S &= \Delta S_{298} + \int_{298}^T \Delta C_P d\ln T \\ \Delta S_{298} &= S_{\text{Mg}_2\text{Si}} - 2S_{\text{Mg}} - S_{\text{Si}} \\ \Delta S_{298} &= 15.25 - 2(7.81) - 4.5 \\ \Delta S_{298} &= -4.87 \text{ cal/mol.K} = -20.38 \text{ J/mol.K} \\ \Delta C_P &= C_{P,\text{Mg}_2\text{Si}} - 2 C_{P,\text{Mg}} - C_{P,\text{Si}} \\ C_{P,\text{Mg}_2\text{Si}} &= 17.52 + 3.58 \times 10^{-3} T - 2.11 \times 10^5 T^{-2} \text{ (cal/mol.K)} \\ C_{P,\text{Mg}} &= 5.33 + 2.45 \times 10^{-3} T - 0.103 \times 10^5 T^{-2} \text{ (cal/mol.K)} \\ C_{P,\text{Si}} &= 5.70 + 1.02 \times 10^{-3} T - 1.06 \times 10^5 T^{-2} \text{ (cal/mol.K)} \\ \Delta C_P &= 1.16 - 2.34 \times 10^{-3} T - 0.844 \times 10^5 T^{-2} \\ \Delta S &= -4.87 + \int_{298}^{523} [(1.16/T) - (2.34 \times 10^{-3}) - (0.844 \times 10^5/T^3)] dT \\ \Delta S &= -5.07 \text{ cal/mol.K} = -21.22 \text{ J/mol.K}\end{aligned}$$

Reaction 3a

$$\begin{aligned}\Delta S &= \Delta S(1a) + \Delta S(2a) \\ \Delta S &= -3.78 - 5.07 = -8.85 \text{ cal/mol.K} = -37.04 \text{ J/mol.K}\end{aligned}$$

Reaction 4a

$$\Delta S_M = R(N_{Mg}^{\beta} \ln(N_{Mg}^{\alpha} / N_{Mg}^{\beta}) + N_{Si}^{\beta} \ln(N_{Si}^{\alpha} / N_{Si}^{\beta}))$$

$$\Delta S_M = (3)(1.98)(0.6667 \ln[0.0078/0.6667] + 0.3333 \ln[0.0038/0.3333])$$

$$\Delta S_M = -26.47 \text{ cal/mol.K} = -110.78 \text{ J/mol.K}$$

Reaction 5a

$$\Delta S = \Delta S(3a) + \Delta S(4a)$$

$$\Delta S = -8.85 - 26.47 = -35.32 \text{ cal/mol.K.} = -147.82 \text{ J/mol.K}$$

Molar Volume

$$V_m = [V][N_A]/Z$$

where V_m is the molar volume , V volume of unit cell , N_A avogadro number , and Z number of atoms per unit cell , the values were obtained from ref.[13].

$$V_m = (6.357 \times 10^{-8} \text{ cm})^3 (6.02 \times 10^{23} \text{ atoms/mole}) / 4 \text{ atoms}$$

$$V_m = 38.66 \text{ cm}^3/\text{mol.}$$

Volume Nucleation Entropy Change

$$\Delta S_v = \Delta S(5a) / V_m = -147.82/38.66 = -3.82 \text{ J/cm}^3 \text{ K}$$

$$\Delta S_v = -3.82 \times 10^6 \text{ J/ m}^3 \text{ K}$$

Volume Free Energy Change

$$\Delta G_v \approx -\Delta S_v \Delta T$$

$$\Delta T = 250 - 500 = -250^\circ\text{K}$$

$$\Delta G_v \approx -(-3.82 \times 10^6 \text{ J/ m}^3 \text{ K})(-250 \text{ K})$$

$$\Delta G_v \approx -9.55 \times 10^8 \text{ J/ m}^3$$

PULICATIONS

1. A.Hatab, W.Yang and W.V.Youdelis:"Effect of Be on the Defect Structure and Formation of β' and β Precipitate in Al-0.7%Mg-0.4%Si Alloy", CIM Conference of Metallurgists, Montreal, Canada, Aug., 1996, p.247-255.
2. A.Hatab and W.V.Youdelis:"Precipitation Rates Studies in Al-0.7%Mg-0.4%Si Alloy, Equivalence of Hardness and Resistivity Techniques", S.MacEwen and T.P. Gilardeau, Eds., Proc. of the Inter. Symp. On Recent Metallurgical Advances in Light Metals Industies, Met. Soc. CIM, Vancouver, B.C., Canada, 1995, p.453-464.
3. A.Hatab and W.V.Youdelis:"Effect of Be on the Aging Behaviour and Precipitation Kinetics of Al-0.7%Mg-0.4%Si Alloy", M.Gilbert, P.Tremblay and E.Ozberk, Eds., Proc. of the Inter. Symp. On Recent Developments in in Light Metals, Met. Soc. CIM, Toronto, Ontario, Canada, 1994, p.269-280.

VITA AUCTORIS

Name: Ali Mehdi Hatab

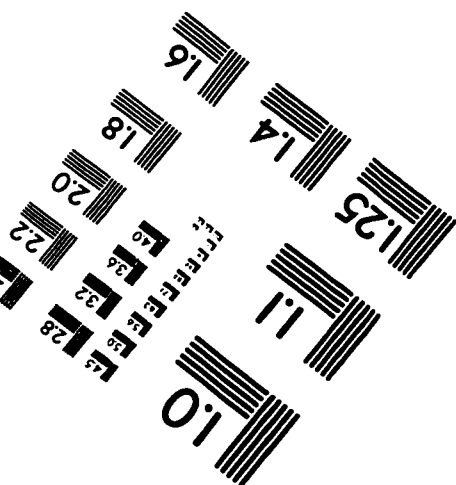
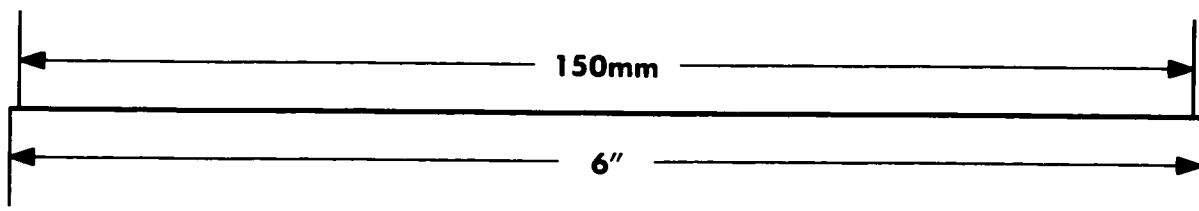
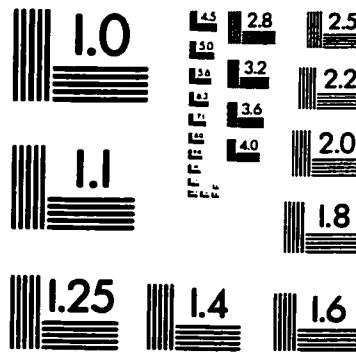
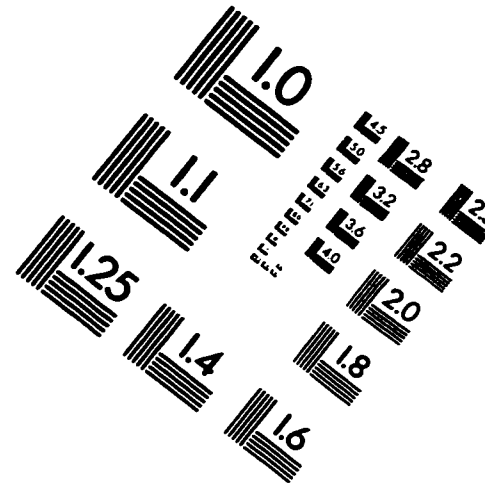
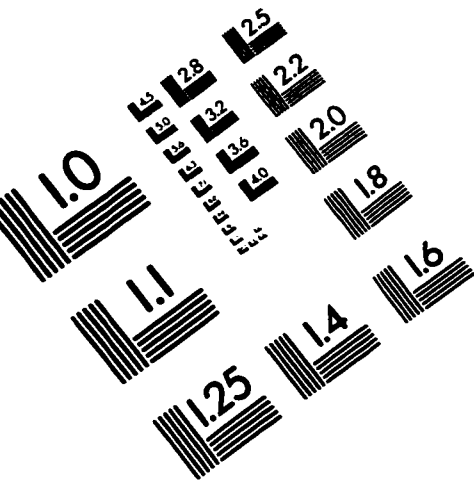
Place of Birth: Tripoli, Libya

Date of Birth: June 21, 1957

Education: University of Wisconsin, Milwaukee, Wisconsin, USA.
B.Sc. with double major in Civil and Material Science
Engineering, 1978-1982.

University of Windsor, Windsor, Ontario, Canada.
M.A.Sc., Engineering Materials 1990-1992.

IMAGE EVALUATION TEST TARGET (QA-3)



APPLIED IMAGE, Inc
1653 East Main Street
Rochester, NY 14609 USA
Phone: 716/482-0300
Fax: 716/288-5989

© 1993, Applied Image, Inc., All Rights Reserved

